

***Laser Welding of Aluminium Alloy 2024:
Experimental Investigation, Numerical
Simulation and Optimization***

A SUDHA KIRAN DUGGIRALA

D-7/ISLM/22/18

Doctor of Philosophy (Engineering)

***School of Laser Science and Engineering
Faculty council of Interdisciplinary Studies, Law and
Management
Jadavpur University
Kolkata, India***

2022

LIST OF PUBLICATIONS

1. Duggirala, A., Paramasivan, K., Acherjee, B. and Mitra, S. (2021), 'Numerical simulation of the temperature field, weld profile, and weld pool dynamics in laser welding of aluminium alloy.', *Optik*, **247**, 167990, <https://doi.org/10.1016/j.ijleo.2021.167990>.
2. Duggirala, A., Dey, U., Paul, S., Acherjee, B., and Mitra, S. (2021), 'Optimization of laser welding parameters of aluminium alloy 2024 using particle swarm optimization technique.', presented in CAMMP-2021, Malaviya National institute of technology, Jaipur (Accepted for publication in *Manufacturing and Processing of Advanced Materials*, Bentham Science publication).
3. Duggirala, A., Acherjee, B., and Mitra, S. (2022), 'Laser welding of materials: A comprehensive study.', in Dikshit, M. (Ed) in '*Futuristic Manufacturing: Perpetual Advancements and Research challenges*' (Accepted for publication).
4. Dey, U., Duggirala, A., Acherjee, B., and Mitra, S. (2022), 'Numerical analysis of conduction mode laser welding of aluminium alloy 2024 in lap joint configuration.' In: Dikshit, M. K., Soni, A., Davim, J. P. (Eds) *Advances in Manufacturing Engineering. Lecture Notes in Mechanical Engineering*. Springer, Singapore. pp.163-173, https://doi.org/10.1007/978-981-1408-2_12.
5. Paul, S., Duggirala, A. and Mitra, S. (2020), 'Study of Laser Beam Welding of AA 2024 Using Taguchi Methodology.', *2020 IEEE India Council International Subsections Conference (INDISCON)*, pp. 248-253, Doi: 10.1109/INDISCON50162.2020.00058.

Statement of Originality

I, A SUDHA KIRAN DUGGIRALA registered on 5th February, 2018 do hereby declare that this thesis entitled "Laser welding of Aluminium Alloy 2024: Experimental Investigation, Numerical Simulation and Optimization" contains literature survey and original research work done by the undersigned candidate as part of the Doctoral Studies.

All information in this thesis have been obtained and presented in accordance with existing academic rules and ethical conduct. I declare that, as required by these rules and conduct, I have fully cited and referred all materials and results that are not original to this work.

I also declare that I have checked this thesis as per the "Policy on Anti Plagiarism, Jadavpur University, 2019", and the level of similarity as checked by iThenticate software is 6%.

Signature of the Candidate:

Date: 18.10.22

Certified by Supervisor(s):

(Signature with date, seal)

1.  · 18/10/22

Professor
Production Engineering Departt
Jadavpur University
Kolkata - 700 032

2.  18/10/22

DR. BAPPA ACHERJEE
ASSISTANT PROFESSOR
DEPARTMENT OF PRODUCTION & INDUSTRIAL ENGINEERING
BIRLA INSTITUTE OF TECHNOLOGY
MESRA, RANCHI - 835215, INDIA

Certificate from the Supervisors

This is to certify that the thesis entitled “Laser welding of Aluminium Alloy 2024: Experimental Investigation, Numerical Simulation and Optimization” submitted by **Smt. A Sudha Kiran Duggirala**, who got her name registered on 5th February 2018 for the award of Ph.D. (Engineering) degree of Jadavpur University is absolutely based upon her own work under the supervision of **Prof. Souren Mitra** and **Dr. Bappa Acherjee**, and that neither her thesis nor any part of the thesis has been submitted for any degree / diploma or any other academic award anywhere before.

1. Smt. A Sudha Kiran Duggirala 18/10/22

Signature of the Supervisor
and date with Office Seal

Bappa Acherjee 18/10/22

2. _____
Signature of the Supervisor
and date with Office Seal

Professor
Production Engineering Department
Jadavpur University
Kolkata - 700 032

DR. BAPPA ACHERJEE
ASSISTANT PROFESSOR
DEPARTMENT OF PRODUCTION & INDUSTRIAL ENGINEERING,
BIRLA INSTITUTE OF TECHNOLOGY
MESRA, RANCHI - 835215, INDIA

ACKNOWLEDGEMENTS

Firstly, I want to thank my supervisors Dr. Souren Mitra, Professor, Department of Production Engineering, Jadavpur University and Dr. Bappa Acherjee, Assistant Professor, Department of Production and Industrial Engineering, Birla Institute of Technology, Ranchi for giving me an opportunity to work on this thesis and providing me valuable guidance and feedback and challenging me to grow as a researcher.

I would like to put on record my sincere gratitude to Mr. Dipten Misra, Director, School of Laser Science and Engineering, for providing necessary support during the entire research work. In addition, I would like to mention the support rendered by Dr. K. Paramasivan for all the value-added technical discussions and for being always there for discussion about anything I was unsure on.

A special thanks to Sri Rabi Shankar Pramanik, staff member of Production Engineering Department for his assistance towards the sample preparation and Sri. Kingsuk Pal, staff member of School of Laser Science and Engineering, Jadavpur University for all the support.

I would like to highlight the truly exceptional support I received from my teammates Souradip Paul and Upama Dey, Research scholars, School of Laser Science and Engineering for the all-round support, motivation, sharing of work and knowledge along with their truly friendly presence.

I want to give my deepest appreciation to Somnath Paul, Ishani Mitra, Ankita Das, Anusree Das, Prithvi Raj Roy for being a great bunch of people in and out of the lab. Their friendship made the work much more enjoyable and kept me sane throughout the whole process.

My sincere thanks to Prof. Dipankar Bose, Head of the department, NITTTR, Kolkata and Arindam Dhar, Research scholar, IEST, Shibpur, who took their time for helping in the microscopic studies along with the infrastructure.

Most importantly, I would like to express my deepest gratitude and affection for my family, for being a constant source of encouragement in the moments of happiness and despair. Without their support this thesis wouldn't have been what it is. They are the constant motivators and the encouraging voices in my head throughout.

DEDICATION

**Dedicated to Vijayawada Kanaka Durga devi and
My Parents...**

PREFACE

Laser welding involves focusing the beam on a small spot using the lens and is a high-intensity heat source. It helps in the processing of a variety of materials which are hard to join with tools. It has high consistency and repeatability. The present research includes the investigation of laser welding on aluminium alloys through experimental and numerical analysis. The research objectives are: developing a thermo-fluid model to analyse the thermal history and defects; experimental investigation of the aluminium alloys for defects; prediction of weld metrics using Gaussian process regression and optimization of parameters employing the particle swarm optimization.

A three-dimensional thermo-fluid model is developed using a finite element model to investigate laser welding of metals welded using a moving heat source. The commercial finite element software COMSOL multi-physics is employed to attain the time-temperature history and defects obtained in the welding process. Results attained from the numerical model are validated with the experimental results and are in fair agreement. A parametric sensitivity study is carried out using the model outputs to determine how different values of an input parameter affect a particular response. The sensitivity study results are further analysed to find a physical explanation of the mechanisms of the process.

The formation of defects is studied exclusively, and the three-dimensional thermo-fluid model on humping is developed to study the influence of parameters on hump formation. The results reveal that the peak power is an influencing factor when laser welding is performed without considering the scanning speed. The Marangoni effect in the molten pool is analysed by varying the input process parameters like peak power and scanning speed. The effect of velocity on the molten pool and variations in velocity with the input parameters is studied for different modes of laser welding. The impact of the molten pool dynamics and the resulting hump formation is evaluated. The simulation studies are conducted for the continuous laser welding and spot-welding processes. The results indicate that the molten pool is laminar, and the Marangoni force is dominant in the melt pool. The design of experiments is performed using the response surface methodology. Structured experiments and further analyses are

performed to construct the empirical models that establish the relationship between the process parameters and responses. The numerous parameters involved in the laser welding operation are optimized to obtain target weld metrics using particle swarm optimization. Finally, the results of the various studies are enumerated, and the future scope of work is proposed. The analysis of variance indicated that the parameters; peak power, frequency, scanning speed and pulse width are all significant when weld width and depth of penetration are the responses. The empirical models find optimum welding conditions to achieve the desired weld quality. The findings of this study can be used to improve weld quality and process control by effectively utilising the laser beam welding process.

VITAE

A Sudha Kiran Duggirala is a research scholar in the School of Laser Science and Engineering, Jadavpur university, was born in Tenali, Andhra Pradesh. She completed her early education in Tenali and obtained her B.E in Mechanical Engineering from Anna University in 2006. Later, she joined as a faculty in MVSR engineering college, Hyderabad. There she taught subjects namely Engineering Mechanics, Heat transfer and Production drawing along with Computer aided design laboratory for B.E Mechanical Engineering, Production and Automobile Engineering students. She got admission into M. Tech in Industrial Engineering and Management in Maulana Abul Kalam Azad University of Technology (MAKAUT) and earned her degree in the year 2016. She secured first position and was awarded gold medal. Subsequently, she joined School of laser science and engineering of Jadavpur university as a research scholar in 2018. Her research interest includes laser material processing, Computer aided engineering, process and design optimization techniques, especially welding. She published papers in journal *Optik* and has presented papers in international conferences along with a book chapter in *Futuristic manufacturing: Perpetual advancements and Research Challenges*. She is a freelance writer in boloji.com.

TABLE OF CONTENTS

Topic	Page No.
LIST OF PUBLICATIONS	I
STATEMENT OF ORIGINALITY	II
CERTIFICATE FROM THE SUPERVISORS	III
ACKNOWLEDGEMENTS	IV
DEDICATION	V
PREFACE.....	VI
VITAE.....	VIII
TABLE OF CONTENTS.....	IX
LIST OF FIGURES.....	XIII
LIST OF TABLES.....	XVII
1. Introduction: Laser Welding of Materials	1
1.1 Chronology of Laser Welding Progress.....	2
1.2 Process Fundamentals	4
1.2.1 Characteristics of Lasers for Welding	6
1.3 Process Mechanics	8
1.3.1 Role of vapour plume in laser welding.....	10
1.3.2 Metallurgical Aspects of Laser Welding	11
1.4 Process Requirements.....	14
1.4.1 Process Parameters	16
1.5 Joint Configuration.....	20
1.6 Quality Aspects in Laser Welding	22
1.6.1 Defects that occur in laser welding	22
1.7 Organization of the thesis.....	29
Chapter 2:.....	30
Literature review and research objective.....	30
2.1 Introduction.....	30
2.2 Review of literature on experimental and analytical studies	30
2.3 Review of literature on optimization techniques in welding	46
2.4 Research status on laser welding of aluminium alloy	48
2.5 Motivation for the present research.....	49
2.6 Objectives of the present research.....	52
Chapter 3: Materials, Experiments and testing	53

3.1 Introduction	53
3.2 Materials	53
Aluminium alloys	53
3.2.1 Grouping of aluminium alloys.....	53
3.2.2 Factors that affect the laser weldability of alloys	54
3.2.3 Laser weldability of aluminium alloys	55
3.2.4 Characteristics of aluminium alloy 2024.....	56
3.2.5 Thermo physical properties of AA 2024	58
3.3 Experimental details	58
3.3.1 Laser welding equipment	58
3.3.2. Technical data of the welding machine	62
3.3.3 Experimental design	62
3.3.4. Pre-experimental procedures	63
3.3.5. Experimental procedure.....	63
3.3.6. Post-welding process	64
3.3.7. Description of the testing equipment.....	65
3.4 Methodologies	66
3.4.1 Response Surface Methodology	66
3.4.2 Response surface experimental designs	67
3.4.3 Gaussian process regression	69
3.5 Particle swarm optimisation	72
3.5.1 Theory of optimisation	72
3.5.2 Classification of optimisation problems	72
3.5.3 Multi-objective optimisation	73
3.6 Approximate Methods for Solving Multi-objective Problems	75
3.6.1 Scalarization method	75
3.6.2 Nature-inspired metaheuristics	76
3.6.3 Theory of particle swarm optimisation.....	76
3.6.4 Multi-objective particle swarm optimisation (MOPSO)	81
3.6.5 Current status of PSO	82
3.6.6 Status of PSO mechanical engineering field	82
3.7 Summary	83
Chapter 4: Finite element modeling of heat transfer and weld pool dynamics	84
4.1 Introduction	84

4.2 Objectives.....	84
4.3 Physical models	85
4.4 Solid-liquid model governing equations.....	87
4.4.1 Model of a laser heat source	87
4.4.2 Theoretical equations	88
4.4.3 Driving forces.....	89
4.4.4 Meshing	90
4.5 Validation of the developed numerical simulation.....	91
4.6 Results and discussion	93
4.6.1 Temperature distribution and fluid flow inside the molten pool	93
4.6.2 Evaluation of weld width and depth of penetration.....	95
4.6.3 Effect of Marangoni convection on weld pool dimensions	100
4.7 Dimensionless melt pool simulation and analysis.....	104
4.8 Summary.....	106
Chapter 5: Experimental investigation on laser welding of AA 2024	107
5.1 Introduction.....	107
5.2 Laser welding of the AA 2024	107
5.2.1 Experimental details	108
5.3 Empirical modelling using RSM.....	108
5.3.1 Results of the experiment	108
5.4 Validation of the developed models.....	115
5.5 Effect of process parameters on the responses	116
5.6 Results and discussion on welded specimens.....	119
5.6.1 Welding Quality Acceptance Criteria	120
5.7 Prediction of weld metrics using the Gaussian process regression.....	125
5.7.1 Training process using Gaussian process regression.....	125
5.7.2 Development of the GPR models	126
5.8 Performance of the depth of penetration and weld width.....	127
5.9 Implementation of the model	129
5.10 Summary.....	130
Chapter 6: Formation of defects and simulation of humping during laser welding of Aluminium alloy 2024	132
6.1 Introduction.....	132
6.2 Defects on the welded samples	132
6.2.1 Hot cracking	132
6.2.2 Porosity.....	134

6.2.3 Softening of fusion zone.....	134
6.2.4 Undercut	135
6.2.5 Loss of alloying elements.....	136
6.2.6 Humping.....	137
6.3 Numerical model of humping formation in laser welding of AA2024.....	138
6.3.1 Proposed Thermo-Fluid model.....	138
6.3.2 Development of the model	138
6.3.3 Laser parameters.....	140
6.3.4 Numerical model	140
6.3.5 Mesh.....	141
6.3.6. Results and discussions	141
6.4. Summary.....	147
Chapter 7: Optimization of process parameters of laser welding of AA 2024	149
7.1 Problem Statement and Methodology.....	149
7.2 Process parameters and ranges	149
7.3 Objective functions	149
7.4 Results of the optimization.....	150
7.5 Time Complexity of the Algorithms.....	151
7.6 Summary.....	151
7.7 Parameter values to obtain the optimized value	152
Chapter 8: Conclusions and future scope.....	158
Bibliography	161

LIST OF FIGURES

Figure 1.1 Different stages in laser beam emission	6
Figure 1.2 Different zones in a laser-welded component	8
Figure 1.3 Pictorial representation of conduction mode laser welding.....	9
Figure 1.4 Pictorial representation of keyhole welding	10
Figure 1.5 Plasma plume surrounding the laser beam and the component's surface	11
Figure 1.6 Epitaxial growth of the grains in a metal.....	13
Figure 1.7 Block diagram of a typical Nd: YAG set-up	16
Figure 1.8 The two plates are placed close to each other without any air gap..	21
Figure 1.9 This welding occurs when welding is done along the overlapping edges by placing the components one upon the other.....	21
Figure 1.10 Welding occurs when a laser is moved along the edges of the plates placed on the other.....	21
Figure 1.11 Welding occurs when a laser is moved along the edges of the plates placed on the other This welding occurs when welding is done by placing the components one upon the other in a T shape.	21
Figure 1.12 Welding occurs when a laser is moved along the edges of the plates placed on the other Welding is done by moving the beam along the edge of the component after placing them one upon the reverse T- shape.	21
Figure 1.13 Pictorial representation of the undercut.....	24
Figure 1.14 Pictorial representation of humping.....	25
Figure 1.15 Appearance of cracks on welded components.....	26
Figure 1.16 Pictorial representation of pores in the weld zone.....	26
Figure 1.17 Incomplete penetration of the weld seam	27
Figure 3.1 Factors affecting the weldability of alloys.....	55
Figure 3.2 Laser welding set-up.....	59
Figure 3.3 Main menu tab of the laser welding machine.....	60
Figure 3.4 Welder mode tab on the laser welding machine	60
Figure 3.5 Work status of laser welding machine.....	61
Figure 3.6 Chiller unit of laser welding machine.....	61

Figure 3.7 Butt welding set-up.....	64
Figure 3.8 Cutting of the component on the shearing machine	65
Figure 3.9 Scanning electron microscope with EDX.....	65
Figure 3.10 Central composite design points in design space	68
Figure 3.11 Box-Behnken design points in design space	69
Figure 3.12 Early variants of PSO. Image courtesy: [134].....	78
Figure 4.1 Pictorial representation of the thermo-fluid model (a) Boundary conditions used in the simulation. (b) dimensions of the workpiece. (c) Mesh used for the modeling.	91
Figure 4.2 Simulated weld pool dimensions for (a) P= 750W, S= 750mm/min, $\alpha=90^\circ$, (b) P= 1250W, S= 750mm/min, $\alpha=90^\circ$, (c) P= 1250W, S= 1250 mm / min, $\alpha=90^\circ$, (d) P= 1000W, S= 1000mm, $\alpha=90^\circ$, (material. AISI 304, beam location y = 10 mm).	92
Figure 4.3 Temperature (K) distributions with fluid flow fields and melt pool evolution at different time instances along the scanning line on the X-Z plane at (a, b) y = 1 mm, (c, d) y = 5 mm, (e, f) y = 10 mm, (g, h) y = 15 mm, and (i, j) y = 19.5 mm.	94
Figure 4.4 Variation of weld width along the scanning path with (a) laser power, (b) scanning speed, and variation of average weld width with (c) laser power, (d) scanning speed when all other parameters remain constant.	95
Figure 4.5 Variation of the depth of penetration with (a) laser power and (b) scanning speed when all other parameters remain constant.....	96
Figure 4.6 Variation of the melt pool volume with power.....	97
Figure 4.7 Variation of melt pool volume with the scanning speed.	98
Figure 4.8 Pictorial representation of the evolution of weld pool during welding at (a) 1 mm, (b) 5 mm, (c) 10 mm, (d) 15 mm, and (e) 19.5 mm (Parameters. laser power = 5 kW, scanning speed = 15 mm/s, and beam radius = 0.36 mm).	99
Figure 4.9 Phase separation and spatial velocity field due to Marangoni convection (Parameters. laser power = 5 kW, scanning speed = 15 mm/s, beam radius = 0.36 mm).....	100

Figure 4.10 Direction of natural convection of the molten pool on YZ plane for different laser power, (a) $P = 2.5$ kW, (b) $P = 3$ kW, (c) $P = 3.5$ kW, (d) $P = 4$ kW, (e) $P = 4.5$ kW, (f) $P = 5$ kW, at scanning speed = 10mm/s, and beam radius = 0.36 mm.	101
Figure 4.11 The direction of natural convection of the molten pool on the YZ plane for different scanning speeds, (a). $V = 10$ mm/s. (b) $V = 15$ mm/s. (c). $V = 20$ mm/s. (d). $V = 25$ mm/s. (e). $V = 30$ mm/s, at laser power = 5kW and beam radius = 0.36mm.	102
Figure 4.12 Velocity field in YZ-XZ planes (a). Isometric view of the velocity field in two mutually perpendicular places. (b). Front view for laser power = 5 kW, scanning speed = 25 mm/s, and beam radius = 0.36 mm.	103
Figure 4.13 Scatter plots of (a) dimensionless width vs Marangoni number. (b). dimensionless width vs Reynold number for different levels of laser power.	104
Figure 4.14 Scatter plots of (a) dimensionless width vs Marangoni number. (b) dimensionless width vs Reynold number for different levels of scanning speed.	105
Figure 4.15 Variations of dimensionless melt pool dimensions with (a) Laser power, (b) Scanning speed.	105
Figure 5.1 Plot of actual vs predicted response of depth of penetration results.	115
Figure 5.2 Plot of actual vs predicted response of weld width results.	116
Figure 5.3 Perturbation plot shows all factors' effects on the penetration depth.	117
Figure 5.4 Perturbation plot shows all factors' effects on the weld width.	117
Figure 5.5 Contour plots indicating the effect of peak power and scanning speed at a frequency of 8Hz and pulse width of 7 ms.	118
Figure 5.6 Response surface plot between peak power and scanning speed ..	118
Figure 5.7 Image showing the weld zone along with heat affected zone and parent material at low power.	124
Figure 5.8 Image showing the weld zone along with heat affected zone and parent material at moderate power.	124

Figure 5.9 Image showing the weld zone along with heat affected zone and parent material at high power.....	124
Figure 5.10 Architecture of the gaussian process regression model.....	126
Figure 5.11 Analysis of regression between the target values and the predicted values for depth of penetration.....	128
Figure 5.12 Analysis of regression between the target values and the predicted values for weld width.....	129
Figure 6.1 Crack present in the weld zone extending to the heat-affected zone.....	133
Figure 6.2 Solidification crack propagating in the heat-affected zone.....	134
Figure 6.3 Columnar dendritic structure at high scanning speed.....	135
Figure 6.4 Honeycomb structure in the fusion zone.....	135
Figure 6.5 Undercut seen on the welded sample at a peak power of 4.75kW.....	136
Figure 6.6 Scanning electron microscope image showing the composition.....	136
Figure 6.7 Hump formed at a peak power of 4.5kW.....	137
Figure 6.8 Hump formed at a peak power of 4kW and 1.4 mm/s.....	138
Figure 6.9 Meshed component.....	141
Figure 6.10 Temperature distribution in the components at different time steps.....	142
Figure 6.11 Fluid velocity in the components at different time steps.....	143
Figure 6.0.12 Flow field and fluid distribution.....	144
Figure 6.13 Hump and root drop.....	144
Figure 6.14 The hump height and molten pool velocity variation with peak power. (a) Variation of hump height with peak power. (b) Variation of velocity with peak power.....	145
Figure 6. 15 Variation in hump height and molten pool velocity with pulse width. (a) Variation of hump height with pulse width. (b) Variation of velocity with pulse width.....	146
Figure 6.16 Evolution of humping with pulse width. (a) Fluid flow pattern at 2 ms. (b) Fluid flow pattern at 3 ms. (c) Fluid flow pattern at 4 ms. (d) Fluid flow pattern at 5 ms.....	147
Figure 7.1 Pareto graph between weld width and depth of penetration.....	151

LIST OF TABLES

Table 1.1 Timelines in the evolution of laser welding.....	2
Table 1.2 Different types of joint configurations welded using laser welding mechanism as shown in Figures 1.8 – 1.12.....	21
Table 3.1 Chemical composition of the aluminium alloy 2024.....	57
Table 3.2 Properties of AA 2024	58
Table 3.3 Technical details of the laser welding machine	62
Table 3.4 Process control parameters and their limits used in the butt joint experiments	62
Table 4.1 Validation of weld pool dimensions	93
Table 5.1 Process control parameters and their limits	108
Table 5.2 Design matrix and measured experimental results.	109
Table 5.3 ANOVA for the weld width model (before elimination).....	110
Table 5.4 ANOVA analysis for the weld width model (after elimination).....	111
Table 5.5 ANOVA for the depth of penetration model (before elimination).	113
Table 5.6 ANOVA for the depth of penetration model (after elimination). ...	114
Table 5.7 Validation test results.....	115
Table 5.8 Tests to be conducted on welded joints [151].....	119
Table 5.0.9 Different weld acceptance criteria	121
Table 5.10 Different covariance and their performance in terms of error	127
Table 5.11 Error obtained from the proposed composite model.....	130
Table 7.1 Process parameters and ranges.....	149
Table 7.2 Values to obtain the optimized value	152

Chapter-1

1. Introduction: Laser Welding of Materials

Welding is a metallurgical fusion-based joining method. The edges of the two joining components are heated above their melting point and allowed to solidify. The melting and solidification result in a permanent joint that is as strong as or more robust than the parent materials. Due to this quality, welding is the most sought-after fabrication process.

Laser welding has emerged as an indispensable joining method in industries to join different materials with varied thicknesses based on the respective applications. The features like narrow heat-affected zone, remote location operations, and automation make laser welding a preferred choice for aerospace, automobile, shipbuilding and defence applications [1]. The body in the white concept of the car is manufactured using laser welding due to its precise heat application and ability to weld sheet metals with 56 slender thickness. The idea of laser welding started with the advent of the CO₂ laser, the most robust laser for welding to date. Subsequently, the variants like Nd: YAG, semiconductor and diode lasers have made laser welding more desirable. The keyhole mode welding firmly joins materials as thin as 10mm in less time. These characteristics have made laser welding more advantageous for weldments formed of materials with varying compositions and qualities. Some of the advantages of laser welding are:

- i. Availability of high-power densities
- ii. Possibility to weld thicker sections and dissimilar materials
- iii. Precise heat input that produces a small heat affect zone and less thermal distortion
- iv. Can be reached in inaccessible places
- v. Absence of contamination.
- vi. Suitable for non-contact welding
- vii. Highly accurate and gives low-distortion joints
- viii. The need for further finishing process is not present

Though there are many advantages of laser welding, certain drawbacks limit the wide usage of the process.

- i. High initial and operating costs of the equipment.
- ii. The presence of hard intermetallic components weakens the joint.
- iii. Chances of defects like pores and cracks due to the high intensity of the beam.
- iv. Vaporization of volatile elements leading to defects like an undercut, humping
- v. Need for higher safety precautions as the radiation affects the operator
- vi. Need for strict joint fit-up
- vii. Precise beam and joint alignment.
- viii. Backpropagation of radiation while welding reflective materials damage the lens.
- ix. Requirement for the skilled workforce

1.1 Chronology of Laser Welding Progress.

Different steps in the advancement of laser welding are given in Table 1.1 [2].

Table 1.1 Timelines in the evolution of laser welding

Year	Significant development
1917	lasers originated with Einstein's 1917 derivation of Plank's law of radiation.
1939	Valentin Fabrikant invented the concept of stimulated emission to amplify radiation
1950	The quantum theory of stimulated emission helped to develop the "maser."
1959	A narrow beam of coherent light called a "laser" was obtained from an optical resonator.
1960	The first laser prototype using synthetic ruby with a wavelength of 694.3nm was developed at the Hughes research laboratory in Malibu, California.

1963	Kumar Patel developed a low-cost, high-efficiency CO ₂ laser at AT&T Bell labs in 1963. For more than 50 years, this was the most widely used industrial laser
1970	New soldering techniques were developed to aid in the advancement of electronic miniaturization.
1980	The science of welding was advanced through robots, various gas mixtures and a wide range of electrode materials.
1985	This year saw the introduction of exciting multi-kilowatt radiofrequency units.
1988	One-kilowatt Nd: YAG laser came into commercial use
The 1990s	Lasers progressed from laboratories to industrial units
1997	Rofin-Sinar produced two-kilowatt diffusion-cooled CO ₂ machines. Trumpf and Luminoics brought out 4 kW Nd: YAG machines that operated on a continuous welding mode.
2000	Magnetic pulse welding was introduced. Diode laser welding joins thin foils made of steel and titanium.
2008	Development of laser-arc-hybrid welding development.
2013	Gas Metal Arc Welding-Brazing was developed as a procedure to weld the steel used in automobiles.
2015	The Ohio State University invented Vaporizing Foil Actuator Welding (VFAW) for joining dissimilar materials. The procedure is comparable to a hybrid of explosive and magnetic pulse welding (MPW).
2016-till date	Laser welding is predicted to grow moderately during this period. The market is growing due to increased demand from end-user industries such as automotive, medical, and electronics. In the medical and jewellery sectors, laser welding is utilised for limited manual welding, die and tool fabrication and maintenance.

Laser micro-welding: Micro-welding using lasers is a process that is gaining prominence in the fabrication of electronic and medical equipment. Highly precise and no-contact workpieces are required for medical applications and are produced by laser welding. The components produced by laser welding have better surface attributes than those produced by resistance welding. But defects like lack of fusion, distortion, and cracking are typical in laser-welded ultra-thin materials. Micro welding using lasers has similar processing parameters and principles as macro laser welding, but the size of the components is minimal and thinner than the standard welding components. The laser beam can be focussed into minimal beam radii of tens micrometres. But, the high amount of heat generated during the welding process creates a HAZ that sometimes affects the fundamental component in the case of micro-welding. The impact on the HAZ is because the component's dimensions are very small. Cracking is a significant problem in micro-welding. The cooling pattern of the thick and long components differs from that of thin and small parts. So handling the defects like humping, cracks and pores is a big challenge that needs to be addressed to obtain sound joints in micro-welding. The problem of micro welding is still more challenging in the case of light metal alloys like aluminium, as high energy density is required initially to overcome the reflectivity of the components.

1.2 Process Fundamentals

Laser welding technology uses the thermal and photonic attributes of laser light. Coherent and monochromatic beams with low divergence and high brightness are more effective in concentrating heat at the weld joint. This light provides an incredibly effective joint prepared with very little energy. The high-intensity heat source is used for welding various materials with thicknesses ranging from a few microns to twenty millimetres [3]. This section addresses the fundamentals of laser welding.

The laser beam is formed in three stages, and each step is completed quickly. **Figure 1.1** depicts the stages in the generation of lasers employed for various material processing techniques.

- **Spontaneous emission:** The laser medium is excited by the pump's energy. This energy causes the electrons in the atoms to transition to a higher energy state. The attained higher state is temporary, and the electrons ultimately degenerate into a lower energy state. This activity generates photons, which are used to dissipate the excess energy received from the pump source. This activity does not require any stimulus. Hence it is termed a spontaneous emission process, the first step in producing a laser beam. Here the direction, momentum and polarisation of the beam are arbitrary.
- **Stimulated emission:** This step occurs when another photon activates an atom with higher energy. This event causes a change of energy from a higher to a lower level, which releases a photon. Both photons (induced and inducing) travel in the same direction and have the same polarization. This polarization results in a succession of photons exhibiting bosonic behaviour, with the photons tending to achieve the same state. This phenomenon is referred to as stimulated emission.
- **Population inversion:** The active medium consists of atoms, ions and molecules that decay from a higher state of energy to a lower state of energy by releasing electromagnetic waves. For stimulated emission to be successful, the upper energy level needs to be more populated than the lower ones. The lasing action occurs because of population inversion at the beginning of a pulse. The resonator mirror selects the polarization for a laser beam.
- Once the amplified beam is generated, it is focused on the surface of a material that needs welding. The concentration of the laser beam at a single point heats the surface, melts and vaporizes it. The molten material gets solidified once the laser beam is withdrawn jointly from the two edges.

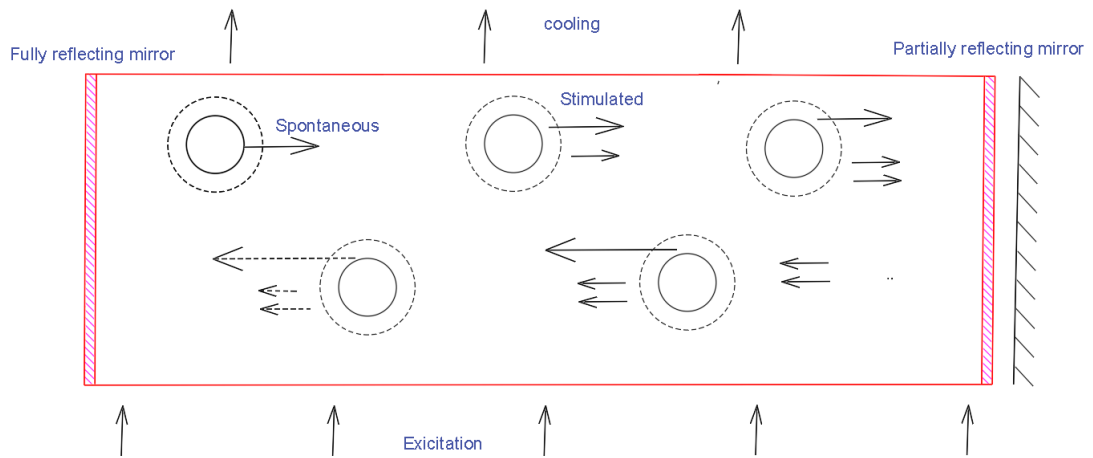


Figure 1.1 Different stages in laser beam emission

1.2.1 Characteristics of Lasers for Welding

Broadly lasers are categorised as gas lasers and solid-state lasers. Among gas lasers: He-Ne lasers, CO₂ lasers, and others are in use. Solid-state lasers have Nd: YAG laser, diode laser, disk laser and fibre laser in their category.

Gas lasers

This group of laser machines use pure gas or a combination of gases to intensify the light. This group's most extensively utilised lasers are helium-neon, argon ion, and carbon dioxide. The efficiency of the weld is higher because it requires less heat (energy). CO₂ laser welding machines are considered the most robust and employed for various applications, including laser welding, cutting, and other material processing techniques [4]. The CO₂ laser operates in the far-infrared range of the electromagnetic spectrum with a wavelength of 10.6 m. The lasing medium is a mixture of CO₂-N₂-He or water vapour that generates a maximum of 50 kW of power.

Solid-state lasers

They are also known as doped insulator lasers. The lasers are built around an insulating material doped with impurities like ions. These lasers' primary advantages are their durable build, ease of maintenance, and outstanding efficiency. They are capable of generating considerable peak powers. The active medium for the neodymium lasers is neodymium (Nd³⁺) (Nd: YAG). The oxide crystals of yttrium aluminium garnet (YAG) have been doped with Nd³⁺ ions to

generate lasers under the Nd: YAG group. These are the most frequently used solid-state lasers. The low excitation threshold and high thermal conductivity generate both pulsed and continuous waves. Nd: YAG laser with lamp pump has a wavelength of 1.06 μm and operates near-infrared rays. The shorter wavelength is suitable for welding aluminium alloys as they absorb 75-90% of the irradiation [5]. The pulsed Nd: YAG is ideal for micro welding and precise heat control applications. The 300W pulsed laser welding can produce a peak power of 5.06kW, helping make keyholes in highly reflective materials. Very high power can be attained when an Nd: YAG is pumped with a diode laser.

Diode laser

The diode lasers operate near-infrared rays at 0.8–1.1 μm . The continuous wave mode of the diode laser is comparable to the He-Ne gas laser. The stacking of diodes improves the power output considerably. For high-power diode lasers, the arrangement of diodes in a linear array form gives a better outcome. These lasers are suitable for laser welding plastics.

These lasers are doped with indium with a wavelength of 940nm. Indium gallium arsenide InGaAs is preferred to achieve stable output in the 750-850nm range. A wavelength of 808nm is suitable for laser material processing using diode lasers [6].

Fibre lasers

These lasers operate at a wavelength of 1.07 μm in the near-infrared region. The power is delivered through an optical fibre cable. The commonly doped elements are Erbium (Er), Neodymium (Nd) or Ytterbium (Yb). The diode laser is used for the pumping process. The lasers have a compact design, and the quality of the generated beam is also high. A relative output efficiency of about 50% can be achieved with these lasers. The demerits include possible damage to the cable at high power and difficulty coordinating the pump laser output and optical fibre.

Disk lasers

These lasers operate in the near-infrared region wavelength of 1.03 μm . The lasers are doped with Ytterbium or Yttrium Vanadate crystal. These lasers are designed to reduce the thermal lensing effect, and the heat produced in the disk

is eliminated by the heat sink placed on the other side of the disk, resulting in effective cooling. The beam quality is also good in disk lasers.

1.3 Process Mechanics

Laser welding is a joining technique that gives out three regions on the worked components. Base material remains unchanged after the process, and the fusion zone contains the materials that form when the molten pool solidifies. Then there is a heat-affected zone which is a part of the base material but has a considerable change in the material properties due to the influence of heat [Figure 1.2]. A series of events occur when the laser beam strikes the weldable surface. In the early stage, a considerable percentage of the beam is reflected. The absorbed amount of the beam heats the surface, increasing the temperature. This rising temperature causes the molten pool to form around the welded edges. Due to the alloying components and the high temperature, some of the material evaporates.

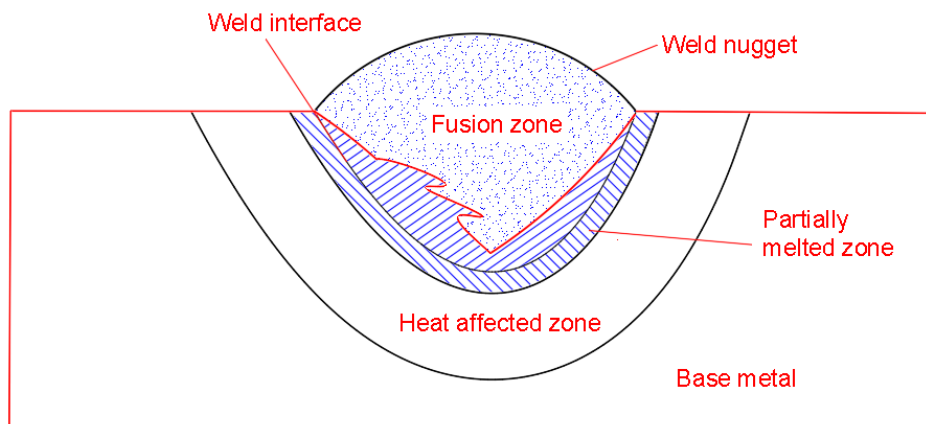


Figure 1.2 Different zones in a laser-welded component

Laser welding mechanics can be classified into two modes: i. conduction mode. ii. Keyhole configuration [5].

i. Conduction mode of welding occurs when the intensity of the absorbed beam is less than the threshold limit. **Figure 1.3** shows the representation of conduction mode welding. This depends on the material's absorptivity and scanning speed, including the input power. For most metals, a value higher than 105 W/cm² initiates the keyhole, and conduction mode welding occurs below this level. Evaporation is insufficient to form a vapour column leading to the

formation keyhole. The weld pool's dimensions are determined by the conduction of heat from the focussing lens and the speed of the beam. The heat transfer by conduction and the Marangoni surface effect is the predominant mechanisms in this welding mode [7]. The resulting heat-affected zone is shallow and broad when compared to the keyhole.

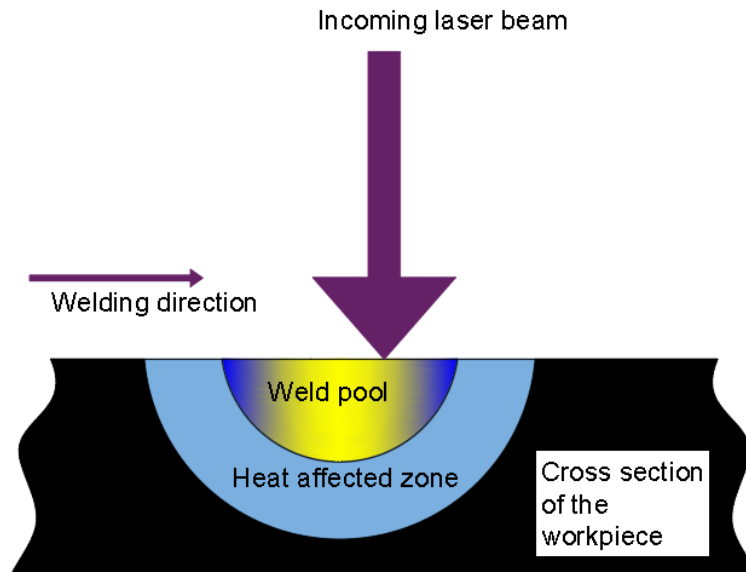


Figure 1.3 Pictorial representation of conduction mode laser welding

ii. Keyhole mode: This mode utilises the minimum amount of heat possible. As seen in **Figure 1.4**, the laser beam impinges on the surface of the specimen. While a significant quantity of heat is reflected away due to the characteristics of metals, the amount of radiation absorbed by the surface melts it above the melting point. The molten pool absorbs more radiation than solids because liquids absorb radiation better. As a result, the component is heated even further until it reaches vaporization temperature. Certain of the material evaporates, forming a cylindrical passage (cavity) known as a keyhole. The liquid with a vapour pressure is retained, and it ionizes the vapour by absorbing the incident radiation and radiating the heat outward along the keyhole wall. Additionally, the substance along the hole's edge absorbs energy from the laser beam. The energy is distributed throughout the keyhole, allowing for deep penetration. Due to the relative movement of the weld head and the workpiece, the keyhole passes through the material, forming a weld seam. As the beam moves along the joint, the molten metal surrounds the keyhole. Five different forces act on this cavity.

Some forces help the cylindrical passage sustain, while others assist in its collapse. The forces that collapse and sustain the keyhole are:

- i. Surface tension that occurs between the molten material and the vapour (plasma)
- ii. Buoyancy force that acts opposite to the direction of beam incidence.
- iii. The uncontrolled violent movement of molten fluid, inner eddies.
- iv. Recoil or vapour pressure occurs in the cylindrical channel in the melt pool. This pressure is higher than the atmospheric pressure and helps the fluid to move up to the surface.
- v. Vaporization of the molten metal that works along with the recoil pressure.

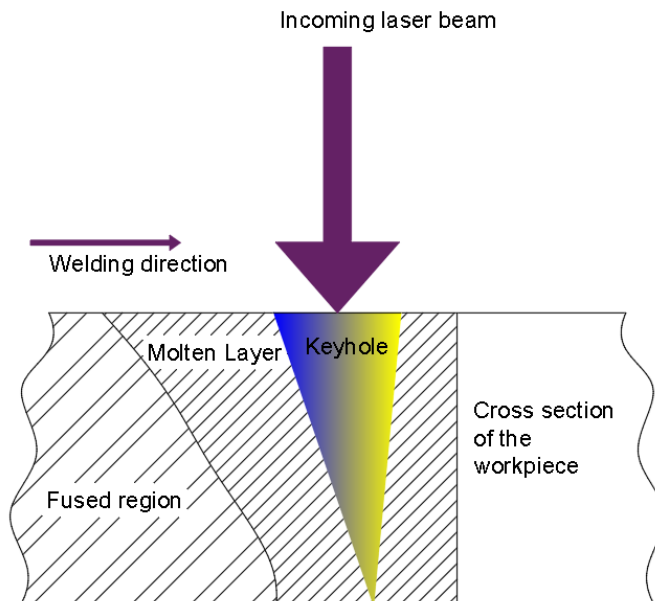


Figure 1.4 Pictorial representation of keyhole welding

1.3.1 Role of vapour plume in laser welding

As observed in **Figure 1.5**, the plasma plume surrounds the welding environment and the work specimen. Keyhole welding is accomplished by the high intensity of the laser light by producing a higher heat extraction rate than the supply rate. This is due to the conduction and convection phenomenon in the metal and back reflection [8]. The local heat increases beyond the boiling temperature of the metal, giving way to its evaporation and dispersion. These

conditions are the recoil pressure that forms a keyhole cavity by exerting a piston effect on the keyhole [9]. The metal vapour gets ionized due to its contact with the laser beam. This ionized vapour combines with the surrounding air and shielding gas and forms plasma inside the keyhole cavity, known as keyhole plasma and above the surface of the workpiece called a plasma plume [10]. This plasma is electrically neutral and consists of electrons and atoms in the excited state. This plasma supports the keyhole's backscattering, beam absorption and refraction processes by supplying the necessary energy [11-12]. Inverse Bremsstrahlung is the primary mechanism that leads to the absorption of the beam in the plasma. This phenomenon is more in the CO₂ laser due to the longer wavelength. This process continues until a threshold absorption factor and then decreases due to the decrease in the density of the plasma plume. The quality of the plasma plume depends on the surface purity and the ambient conditions [13]. High-speed cameras and x-ray imaging techniques are employed to study the plasma plume and its role in keyhole formation.

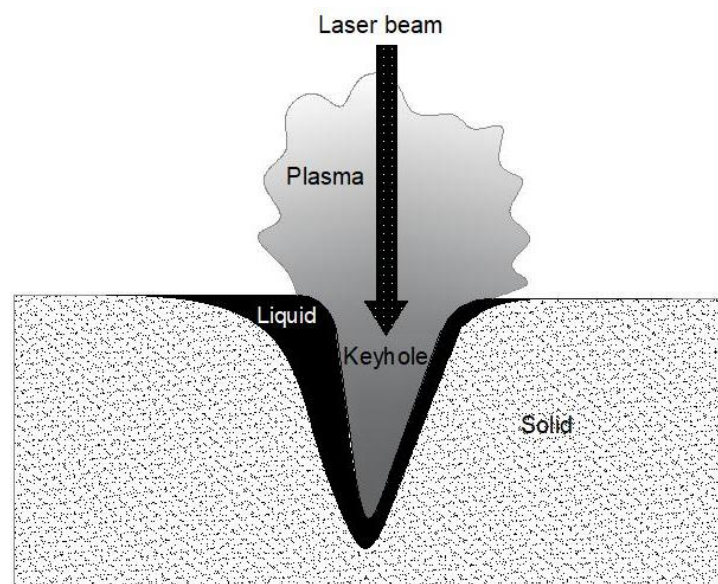


Figure 1.5 Plasma plume surrounding the laser beam and the component's surface

1.3.2 Metallurgical Aspects of Laser Welding

The flow of heat causes the phase transition and microstructure of the material during the welding process. The resulting microstructure affects the weldment's

characteristics, the presence of residual stresses, defects, and distortion. The laser beam generates heat during the laser welding process. Due to the target materials' surface qualities, the heat source's efficiency varies during welding. Irrespective of the surface conditions, three distinct zones are formed during the laser welding process: the fusion zone, the partially melted zone, and the heat-affected zone. The zones are classified according to the extent to which heat affects a specific area. Generally, the fusion area of laser-welded components has a fine-grain microstructure.

Fusion zone (FZ)

The Fusion zone is the place where actual melting occurs. Melting and solidification occur here to form the weld joint. This melting and solidification process is material- and structure-dependent. For instance, the cracking phenomenon in aluminium alloys can be minimized by utilizing a silicon-containing filler material [14]. The fusion zone in autogenous welding is just a melted and resolidified base material. The only change in the microstructure happens due to the alloying components evaporating. The composition of the material solidifying in the fusion zone is not as consistent as that of the base material. The solute's atoms redistribute, resulting in a change in composition. The phase diagram and kinetics, mass transfer and diffusion, undercooling, and other associated phenomena all affect this redistribution rate. A pure metal's solid-liquid contact is typically planar [15]. However, the solidification pattern might be cellular or dendritic, depending on the type of materials and thermal history. Grain development in the FZ is critical because it impacts solidification. In laser beam welding, the grains parallel to the fusion line serve as the nucleation substrate. Due to the proximity of the melt pool liquid to the underlying layer, nucleation occurs quickly. Epitaxial welding is the process of nucleation that occurs during autogenous mode welding and can be identified using the x-ray backscattering technique. The epitaxial grain structure enhances the weld's strength and minimizes its cracking susceptibility. It prevents the creation and progression of cracks. **Figure 1.6** illustrates epitaxial development in any metal. The $\langle 100 \rangle$ in **Figure 1.6** indicates the number of directions for grain development.

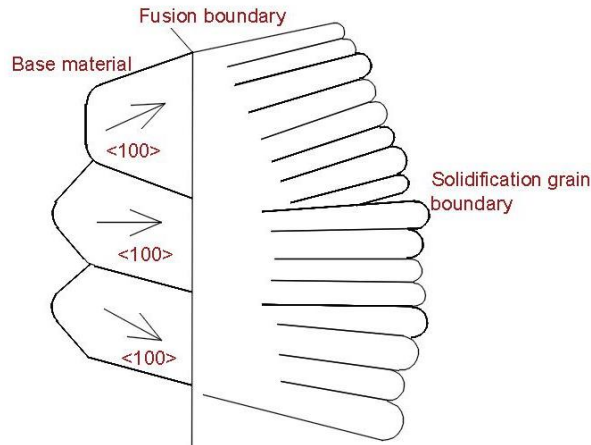


Figure 1.6 Epitaxial growth of the grains in a metal.

The following process variables affect grain development and microstructure:

The increased scanning speed produces an elongated shape for the weld and hence a columnar grain structure. When the traverse speed of the beam is high, fine grain size results in a refined dendritic structure due to the low heat input in the case of aluminium alloys, as reported by [16]. The effects of welding with an Nd: YAG pulsed laser machine on the microstructure of aluminium alloy 2024 are studied extensively. It is reported that pulsed mode laser welding results in finer inter-dendritic phases and that for low-duty cycles, the precipitates in the fusing region contain a small number of solute components [17]. Low-duty cycles provide a faster cooling rate than high-duty cycles. When welding at high speeds, columnar grain development is normal in the welding direction [18]. It's essential to consider grain growth while assessing the ductility of components. When the scanning speed is high, Nd: YAG lasers generate weldments with poor ductility [16]. In a component with a columnar grain structure, solidification and liquation cracks are more apparent [14,19]. When welding aluminium alloys, factors such as decreased welding speed and solidification rate, preheating, chemical composition changes in the melt pool due to filler material, and decreased undercooling contribute to epitaxial grain development.

Unmixed zone (UZ)

This zone is present in almost all fusion weldments. UZ is a stationary liquid layer that thrives when the fluid velocity approaches zero around the fusion line. Evaporation of the liquid metal from the fusion region of contamination on the surface, filler material selection, and process parameters all contribute to the formation of the unmixed area. This region's microstructure is identical to that of the fusion region. The unmixed zone may not be present in high-speed welding processes such as laser beam welding [14].

Partially melted zone (PMZ)

PMZ is the zone between liquid and solid, i.e., between the material's liquidus and solidus temperatures. Certain variables affect the PMZ range: The alloying elements or impurities in the base metal increase the base metal's actual melting temperature range. The PMZ of aluminium alloys is exceptionally narrow, about the size of a single grain or two grains [18].

Heat-affected zone (HAZ)

This zone is what separates the PMZ from the unaffected base metal. This region is not subject to melting or evaporation. However, the heating and cooling phenomena, input process parameters, and metallurgical reactions such as recrystallization, phase transitions, precipitate formation, residual stresses, and grain development impact the microstructure of HAZ. The heat-affected zone is relatively small when welding at low temperatures or in materials with a high thermal diffusivity. Laser welding has the advantage of delivering a narrow heat-affected zone compared to other welding methods.

1.4 Process Requirements

Achieving laser-based joining involves a proper selection of heat source, beam transmission equipment, processing set-up equipped with suitable optics, and attachments, as shown in **Figure 1.7**. Laser material processing employs a high-intensity focussed beam onto a component. The laser beam traces the defined geometry. Though the primary laser varieties and the parts used in the machines remain the same specific differences in the components lead to different material fabrication methods. The parameters at focus and the shielding gas supply

mechanism differentiate laser welding from other laser material processing techniques.

The process requirements for laser welding are

i. Laser generation: The interaction of electromagnetic radiation with the surrounding matter spurs spontaneous emission and absorption. When the atoms attain the excited state, stimulated emission is the initiator of laser light.

ii. Optical resonator: The primary purpose of an optical resonator is to define the direction of the laser beam. The photons attain their respective states using an optical resonator.

iii. Laser pumping: Lasers are also often classified by the pumping mechanism. This mechanism is also called population inversion and is the main reason for the occurrence of lasing action. The pumping mechanism is broadly divided into optical pumping and electrical pumping. Pumping can be either continuous or pulsed.

iv. Broadening mechanisms: This mechanism influences the profile of the spectroscopic line after the emission profile of the laser. When a laser is broadened homogeneously, the bandwidth of every atom in the beam is equal to the entire bandwidth of the laser beam. This mechanism is caused by the collision of molecules in the gas. If the atoms gain at various frequencies, then it is heterogenous broadening. The most common source of this mechanism is the doppler effect. The broadening mechanism provides the advantage of reducing the problems that occur by the air gap during butt welding.

v. Beam modification: Beam modification is accomplished using a focusing lens, cartesian axis or provision for translation of optics along with shield gas and filler materials. The lens with a small focal number is suitable for high-speed welding of thin materials. Generally, welding speed can be maximum if the focussing depth is equal to the thickness of the plates to be welded. The focusing lenses with a high f-number reduce the damage to the lens due to weld spatter or backscattering.

vi. Beam delivery: The delivery of the laser beam plays an essential role in laser material processing. The fibre optic beam delivery is the most common and

frequently employed system, a simple plug-in fixture with no mirrors attached. It has the flexibility to get connected to robots and in fully automated factories. CO₂ laser with a mirror delivery system consists of simple geometry and is most suited for symmetric components. Here the beam is fixed, and the components like the gear wheel and shafts are rotated to get joined. The components that are joined are placed on the spindle.

The shielding gas is used at the laser irradiation zone to protect the weld bead and molten pool from contamination using a gentle and unfocussed delivery.

Other related parameters for laser welding are:

- The shielding gas protects the weld bead and molten pool from contamination using a gentle and unfocussed delivery.

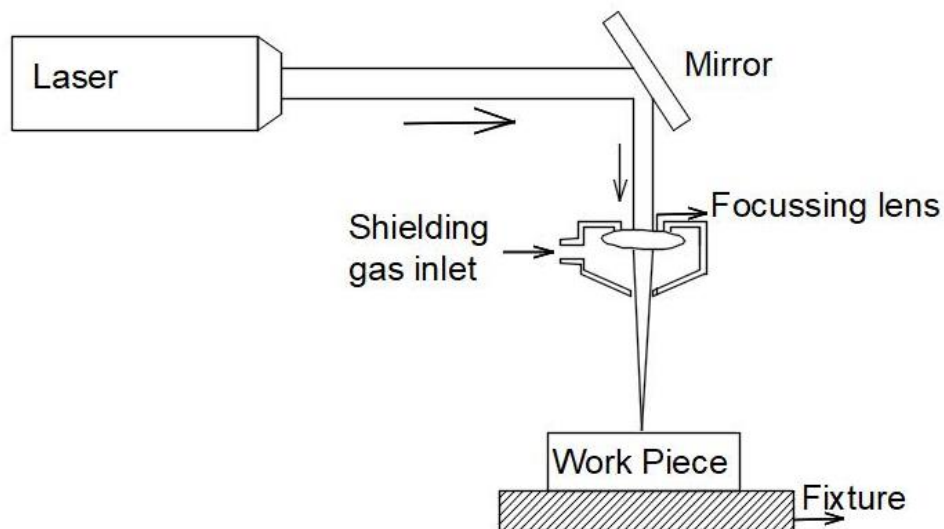


Figure 1.7 Block diagram of a typical Nd: YAG set-up

1.4.1 Process Parameters

Laser welding is a complex and multivariable process influenced by the properties of welding equipment, laser beam and workpiece (material and dimensions). The major contributing factors to laser material processing are:

- Beam power:** This is the most critical aspect of creating keyholes. Aluminium alloys require larger power densities for welding due to the material's physical features, such as greater reflection and thermal conductivity. Additionally, imperfections such as splatter, undercut, underfill, and dropout is typical at higher powers. [20] conducted several experiments

on aluminium alloy 7020 and reported that both the weld width and depth of penetration increased with the peak power. The higher penetration depth is because, at high peak power, the energy incident on the weld zone is higher, leading to higher melting and vaporization.

ii. Traverse speed: Beam traverse speed affects the penetration depth. When welding at a faster rate, the depth of the keyhole is reduced, and the weld geometry retains its shape. When the welding speed is reduced, conduction mode welding occurs. On the other hand, the ratio between the welding depth and weld width (d/w ratio) rises with welding speed, although insignificant and then stabilizes. The following are the advantages of high-speed welds: Minimum evaporation of alloying components results in a refined grain structure in the fusion zone, and the shape of the weld bead changes with a change in the scanning speed [20]. But the depth and width of the weld decrease as scanning speed is inversely proportional to input power for a unit length of the seam. With high scanning speeds, the weld becomes shallow and narrow.

iii. Wavelength: When incoming laser light strikes a material's surface, it is absorbed and performs the required activity, such as welding or cutting. This absorption is wavelength-dependent. The light with a longer wavelength reflects more and limits beams' application to alloys with high reflectivity. As a result, increased fluences are necessary for coupling with such materials. A shorter wavelength beam improves process stability, resulting in increased Fresnel absorptivity. If w_0 = radius of the Gaussian mode laser source and λ = wavelength of the incident laser light with focal length f_l , then the radius of focus w_f is given by

$$w_f = \frac{1}{\pi} \left[\frac{f_l * \lambda}{w_0} \right] \quad (1.1)$$

iv. Beam mode: The beam's energy distribution affects the weldment's final shape. A TEM00 mode has a higher d/w ratio than other modes of a higher grade. This higher is due to the smaller beam radius, which produces a highly focused beam. However, multimode beams have a bigger diameter and are suitable for butt welding, reducing the need for stringent edge fit-out. Input

energy affects vapour formation and the size and interactions of the keyhole and melt pool. These values are widely used to explain the stability of the process [21].

- v. **Beam stability:** Spatial and temporal variations in beam attributes influence beam stability. This factor, along with the properties like power available during welding, the material's absorptivity and others, influence the weld quality.
- vi. **Beam Polarization:** In practically any type of laser material processing, a laser beam's polarisation aspect significantly influences the outcome. The beam's polarisation direction in the plane of interaction is referred to as p-polarization, and its orthogonal direction is referred to as s-polarization. The angle of incidence on the surface is determined by the beam propagation and the normal on the surface. The incidence angle is close to 90 degrees in these geometries. The quantity of light reflected or transmitted varies depending on the incident polarization. The Fresnel equations demonstrate that obliquely incident light's transmittance and reflectance are polarised. The weld pool behaviour is directly impacted by energy accumulation, masking phenomena, and beam polarization. The effect of beam polarisation on the welding process is material- and process-dependent [22].
- vii. **Spot size and power density:** The obtainable power density is decided by the spot size. When the spot size is smaller, the power density is higher, leading to narrow welds without proper fusion.
- viii. **Beam divergence:** The expansion and propagation of a beam are termed beam divergence.
- ix. **Focal length:** Along with waist diameter and depth of focus, focal length determines spatter generation and the level of damage to optics.
- x. **Depth of focus (DOF):** the maximum deviation the component can make from the position of optimal focus while still maintaining a reasonable weld quality is DOF. When welding thicker pieces, a greater DOF is advantageous.
- xi. **Position of the focal plane:** The smallest waist diameter is generally at the focal plane. Positive focusing (above the material's surface) produces more plasma, which results in less energy reaching the material's surface. Through

repeated reflections and efficient coupling, negative focusing (below the material's surface) boosts energy absorption.

xii. Shield gas: Shielding gas hinders corrosion of the weld seam and prevents vitiation of the seam by moisture, grease, and other contaminants, and protects the optics; shielding gas also aids in the development of keyholes by minimizing their instabilities during welding. As a result, a poorly protected weld exposes the bead's porosity, undercut, and roughness. The melt pool is wider and deeper with filler material than with autogenous welding, indicating the need for improved shielding. Argon and helium are the frequently employed gases for laser welding.

- Argon (Ar): Ar is the gas of choice for low-power laser welding. Argon offers superior shielding and smoother surfaces and is also cost-effective. When Ar is employed in high-power applications, the gas absorbs most of the energy required for ionization, limiting penetration.
- Helium (He): Due to its higher ionization potential, He is best suited for low-speed applications. Due to the gas's lower density, more effective flow rates are required for adequate protection. As a result, greater threshold energy is necessary to generate a plasma plume. This plume boosts the laser light's transmissivity through the gas. Due to the lack of early connection between the radiation and the plasma, it is challenging to produce a keyhole. These phenomena are found when welding aluminium at a speed of around 3 m/min using a 2.5 kW laser and He as the shielding gas [3].
- Nitrogen (Ni): Ni is an excellent material for fabricating keyholes and deep penetration welds. Nitrogen is not extensively used as a shielding gas since it can potentially create nitrides, weakening the weldment. Thus, the weld's quality is determined by the shielding gas used. The effect is more evident at low welding speeds and higher power densities, as the local vapour density above the workpiece is substantially greater. Compared to Ar and

Ni, He performs better as a shielding gas under the given operating parameters and processing conditions [23].

xiii. Surface quality: The components to be welded ought to be freed from impurities, as local melting of contamination results in poor metallurgy and rapid material loss from the surface during the welding process. Surface characteristics such as roughness occasionally enhance the laser beam's absorption.

xiv. Joint design: The accurate and high-intensity beam requires appropriate joint alignment, and the acceptable joint gap tolerance is also relatively small.

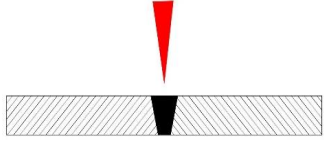
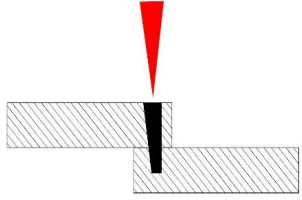
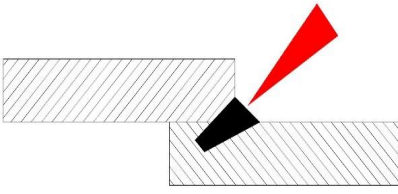
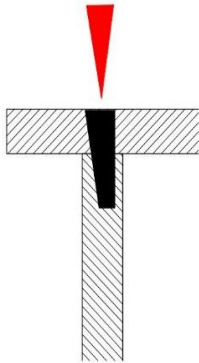
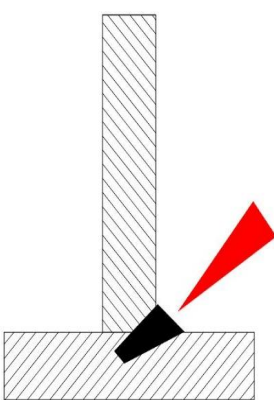
When functioning in pulsed mode, the welding is additionally impacted by the pulse energy and width, pulse shape and repetition rate, and average laser power. When experiments are conducted on AA 7020, the pulse which follows the ramp downtrend has shown no hot cracking defect. But the square pulse has induced hot cracking in the welds [20]. Additionally, welding time and weld length are significant criteria. Because the material must absorb the incident beam, weld quality is influenced by thermal conductivity, reflectivity, solidus and liquidus temperature, thickness, and heat capacity.

1.5 Joint Configuration

A variety of joint configurations is possible using the laser welding technique. The type of joint is often decided by the demand of the job at hand. A description of some joint configurations (though not limited) that are possible with laser welding is depicted in **Table 1.2**.

1. Butt joint
2. Lap joint
3. T-joint

Table 1.2 Different types of joint configurations welded using laser welding mechanism as shown in **Figures 1.8 – 1.12**.

Joint name	Figure	Preparation
Butt Joint		<p>Figure 1.8 The two plates are placed close to each other without any air gap.</p>
Lap Joint		<p>Figure 1.9 This welding occurs when welding is done along the overlapping edges by placing the components one upon the other.</p>
Lap Joint		<p>Figure 1.10 Welding occurs when a laser is moved along the edges of the plates placed on the other.</p>
T-Joint		<p>Figure 1.11 Welding occurs when a laser is moved along the edges of the plates placed on the other This welding occurs when welding is done by placing the components one upon the other in a T shape.</p>
T-Joint		<p>Figure 1.12 Welding occurs when a laser is moved along the edges of the plates placed on the other Welding is done by moving the beam along the edge of the component after placing them one upon the reverse T- shape.</p>

1.6 Quality Aspects in Laser Welding

ISO 5817:2014 and ISO 13919-1 mention various materials' acceptable defects in fusion-welded joints. It is applied to materials with thickness than or equal to 0.5 mm and ferrous and non-ferrous alloys, manually operated or machine controlled or automated welding including all positions and varieties of welds. Butt joint welds with full penetration and partial penetration and fillet welds are covered in these specifications.

The system prescribes three levels of quality, allowing welded joints to be used in various applications. The symbols given to the levels are B, C and D.

Level B has the highest quality and is used in thermal loading, corrosion, pressure and static loading applications. Several researchers reported that the relationship between the acceptance limit and the consequent fatigue life is linear for certain defects. There is a greater demand for designing and fabricating economic weld structures. Different aspects of production like material, fabrication, maintenance of tolerances within the cost and attaining the objectives like quality and price are often contradictory. Laser welding is a good choice for versatile materials. It has some drawbacks due to the high-intensity heat source and other requirements.

1.6.1 Defects that occur in laser welding

Depending on material composition, and welding conditions, various defects occur in laser-welded components. These imperfections are categorised into three types: Geometrical defects, (ii) internal defects and (iii) property defects.

Geometrical defects

i. Deformation or distortion

The thermal cycles like heating, melting, evaporation, solidification and cooling that occur in the metal during laser welding leads to changes in volume due to thermal expansion or contraction. These volume changes lead to distortion or the presence of residual stress and the formation of cracks in the joints. Though distortion is negligible in laser welding due to narrow weld beads, high speed and deep penetration are also responsible for distortion. The more significant

coefficient of thermal expansion of aluminium leads to distortion in the laser-welded components.

Suppression procedure

- Use of rigid fixture or jig
- Quick cooling and quenching of the final component
- Allowing the welded components to come to room temperature while in the fixture.
- Welding procedures optimization.

ii. Poor surface appearance of the laser welds

These are generally caused by oxidation, ultra-fine particles, fumes, or spatter. Pits and undercuts also render a poor surface appearance.

In laser welding, the metallic silver colour of certain metals like aluminium or titanium alloys may change to heavy blue, purple, black, or golden, based on the oxidation level.

Suppression procedure

- A proper shielding gas reduces oxidation when flown in an optimum direction.
- Using a laser beam in the defocussed conditions,
- Use of vacuum chambers
- Employing a beam with a smaller diameter than the molten pool is a technique that can be utilised in continuous-mode laser welding.
- While working in pulsed mode, increasing the power density deepens the keyhole, slowly reducing the spatter.

iii. Burn through or meltdown

This defect is said to occur when the molten metal drops down during welding to form a concave top surface while the bottom surface is convex-shaped.

This phenomenon generally occurs in welding thin sheets and when thick plates are welded at high power. The meltdown readily occurs in materials with lower surface tension.

Suppression procedure:

- Bottom humping can be prevented in materials with high Oxygen content.
- Optimization of welding conditions
- Employing a backing plate while welding
- Using appropriate shielding gas

iv. Undercutting

The notch that forms along the toe of the weld is called an undercut. This defect generally occurs due to the high pressure of assist gas, wide weld bead formed due to high power density, and ample shielding gas supply from the front side of the component. The effect of gravity also helps in the formation of the undercut. The undercut is represented in **Figure 1.13**.

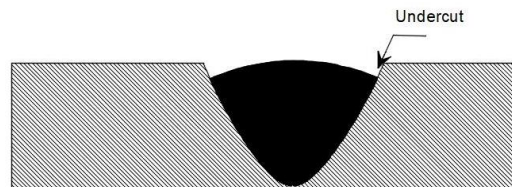


Figure 1.13 Pictorial representation of the undercut

Suppression procedure:

- Optimization of welding conditions
- Use of filler wire during welding

v. Underfilling

Underfills occur as concave surfaces on the weld bead. This underfill happens during the welding of butt joints with wide gaps and a shortage of filler rods. Burn-through and spattering accompany underfills in case of complete penetration.

Suppression procedure

- The utilization of filler rods, beam scanning, and a gradual increase of laser power suppress underfilling.

vi. Humping

The development of lumps of weld metal on the bead surface at some intervals is called humping. These lumps occur in narrow weld beads produced at high welding speed and small focussed beam, low vacuum welding. The higher surface tension of the molten pool and the backward flow of melt expulsion by plume ejection are the main reasons for humping. **Figure 1.14** indicates the humping in the welded joint.

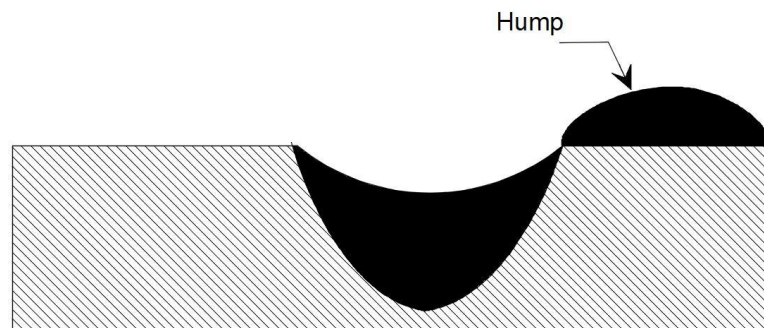


Figure 1.14 Pictorial representation of humping

Suppression procedure

- using defocussed distances
- Suppression of upward ejected melt.

Invisible defects

i. Hot cracking

High-temperature cracking on the weld fusion zone and heat-affected zone (HAZ) is called solidification cracking and liquation cracking, respectively. Cracking occurs along the grain boundary. The cause for solidification cracking is the formation of low solidification temperature liquid film along the grain boundary.

Suppression technique

- Select appropriate materials and processes to minimize tensile load at the welding time.
- Liquation cracking occurs due to the liquid trapped in the bottom part of the laser.

- Modifying the shape of the pulse in the case of pulsed laser welding [20].

ii. Cold cracking

This type of cracking occurs below 300⁰C. It is also known as delayed cracking or Hydrogen assisted cracking. A typical cracking on the weldments is represented in **Figure 1.15**.

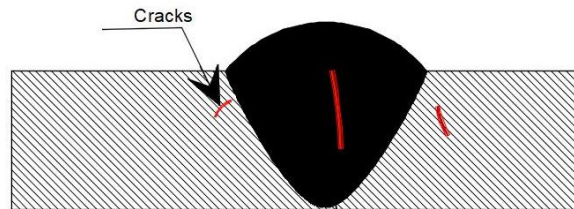


Figure 1.15 Appearance of cracks on welded components

Suppression technique

- Proper selection of filler wire
- Appropriate weld bead geometry

iii. Porosity

Porosity is the most common defect during laser welding, as shown in **Figure 1.16**. The bubbles generated at the tip of the keyhole during deep penetration stay as pores in the fusion zone of the weld. Welding conditions, surface cleanliness, and type of shielding gas affect the formation of pores.

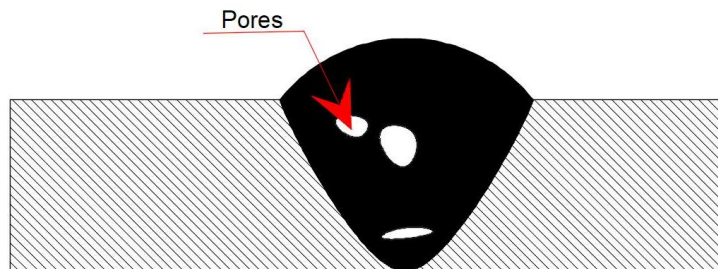


Figure 1.16 Pictorial representation of pores in the weld zone.

Suppression procedure

- Control of laser power density
- Choosing a suitable pulse profile towards the end of the laser irradiation

- Removal of the oxide film
- Performing conduction type of welding
- Low or high vacuum welding

vi. Spiking

Saw-like penetration with a periodical variation that forms near the bottom part of a partially penetrated weld bead is called spiking.

Suppression procedure

- Reduction of weld power density
- Beam scanning
- Tandem beam welding

vii. Swelling of lap joint

This type of defect takes place in thin Aluminium alloy when it is subjected to low welding speed and high heat input. When more welding occurs in the upper and lower sheets, swelling is said to occur.

viii. Incomplete Penetration

This type of defect occurs in the following ways:

- When the weld bead does not reach the bottom of the components.
- When weld beads that form from both sides do not fuse
- When welding starts like a bridge across two pieces

Incomplete penetration occurs in materials with high reflectivity and high conductivity, like Aluminium and Copper, as represented in **Figure 1.17**.

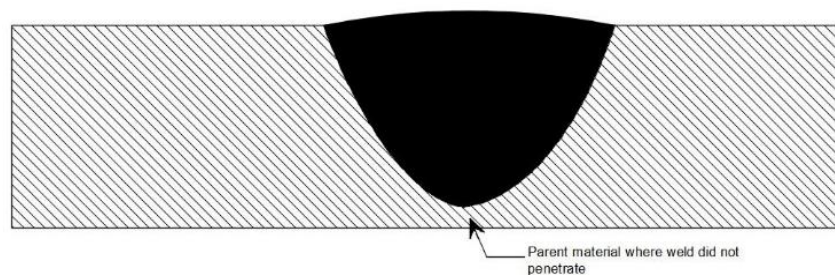


Figure 1.17 Incomplete penetration of the weld seam

ix. Inclusions

The oxide layer is present on the surface of the Aluminium components protecting them in corrosive applications that lead to inclusions. Nitrides can form in the melt pool when Nitrogen is used as a shielding gas. Nitrides in the molten pool of Aluminium 6xxx series protect it from solidification cracking. Though oxides and nitrides are beneficial, they stay as inclusions in the final weld bead, weakening it.

Suppression procedure

- Proper surface cleaning
- Usage of appropriate shielding gas.

x. Evaporation loss of alloying elements

The impurities on the surface, volatile elements with lower vaporization temperature than the base material when present as alloying elements, evaporate quickly at a higher amount.

Suppression procedure

- Using an appropriate filler material
- Adopting high-speed welding.

Quality or property defects

i. Reduction in mechanical properties

Certain welding defects like porosity and cracking degrade the mechanical properties of the welded joint. Experimental investigation on certain Aluminium alloys of the 5xxx series indicated that the strengths obtained from the welded joints are significantly lower than that of the parent material due to the presence of porosity cracks and underfills. Hence, to improve mechanical properties, obtaining defect-free welding is vital.

ii. Degradation in chemical properties

Stress-corrosion cracking and grain boundary corrosion may occur in the HAZ of certain metals and alloys. Improved chemical properties require a better choice of material, the employment of lesser heat input for the welding

operation, the elimination of residual stresses, and the appropriate protection of the weld to avoid oxidation by employing a suitable inert shielding gas.

1.7 Organization of the thesis

This thesis is written as a summary of the experimentation, numerical simulation and optimization of the laser welding of aluminium alloy 2024. The focus is on producing successful welding on the hard-to-weld aluminium alloy 2024, developing a 3-dimensional, transient numerical model to simulate the laser welding process and optimizing the process parameters involved in attaining successful welds.

Chapter 1 is a general and broad introduction to laser welding and different aspects of the process.

Chapter 2 reviews the latest and relevant state-of-the-art literature on the study area. It focuses on the literature published on analytical studies, experimentation, and optimization. This chapter outlines the research gaps, the study's need, and problem formulation and hypothesis for the thesis.

Chapter 3 describes the materials used in this study and the methodologies employed. It also describes the equipment used for experimentation and testing.

Chapter 4 gives the development of a numerical model for the simulation of laser welding on aluminium alloy 2024. Various process parameters' influence and impact are simulated and depicted using pictures and graphs.

Chapter 5 describes the results of the structured experiments and the response surface graphs. This chapter also describes the prediction of weld metrics using the deep-learning techniques

Chapter 6 discusses the various defects in the experimentation and simulates the humping phenomenon during high-speed techniques like laser welding.

Chapter 7 presents the results of optimization using the particle swarm optimization technique.

Chapter 8 gives general conclusions along with the inferences of the present work.

Chapter 2:

Literature review and research objective

2.1 Introduction

Laser beam welding occupies an indispensable position in the manufacturing industry. Light metal alloys are fast replacing traditional materials owing to their superior density, strength and economic properties. Aluminium alloys are prominent among light metal alloys due to their properties and availability. The aircraft and automobile industry is looking towards AA2024 as a prospective material to manufacture various components. Much research has been conducted to understand aluminium alloys' microstructural, metallurgical, and mechanical properties. However, based on the latest and available literature, the results reported so far are on the application-specific areas, material and its properties, numerical studies, the impact of process parameters and mechanical testing. They are specific to a particular series of alloys and cannot be implied to AA2024. The research on this alloy is minimal. This chapter reviews the material properties, variety of lasers for different welding alloys, microstructural and numerical studies, and the optimization techniques employed in the laser welding process that are relevant to this thesis.

2.2 Review of literature on experimental and analytical studies

Kou and Sun [24] used a computer simulation to study the effects of fluid flow patterns in the weld pool on weld penetration. The importance of three forces is explored, including buoyancy, surface tension, and electromagnetic force, as well as the role of surface-active elements. In addition, a novel approach to solving the heat flow and fluid flow boundary conditions is proposed.

Ratchev et al. [25] conducted several studies on aluminium alloys' precipitation and age hardening. The age hardening of an aluminium alloy with Al±4.2 wt% Mg±

0.6 wt% Cu alloy was investigated. A yield strength which increased linearly along with the logarithm of time at peak hardness after 11 days of ageing is reported in this study.

Frewin and Scott used [26] a 3-D heat transfer finite element model during pulsed mode laser welding in ANSYS because of its heat transport and parametric design features. The model determines the fusion zone, heat-affected zone, thermophysical characteristics, and experimentally determined beam profiles. The findings indicate that weld size and temperature profiles are vital factors.

Limmareevichitr and Kou [27] proposed visualizing Marangoni convection in weld pools formed during arc welding. It was concluded that Marangoni convection is noticeable when the diameter of the welding beam is reduced and the beam power is increased.

Miller et al. [28] reviewed using aluminium alloys in the automotive industry. The current and future trends in aluminium welding and brazing techniques are presented in detail.

Matsunava et al. [29] investigated critical hold behaviour during laser welding. It has been stated that evaporation at the local front, notably from the front wall of the keyhole's inner half, is the primary source of keyhole instability. Porosity is suppressed if the keyhole is stable. Pulse modulation is considered a crucial step in porosity suppression if the keyhole is stable when employed as a keyhole. Ni was also found to be beneficial in suppressing pores within aluminium alloys.

Borrisutthekul et al. [30] used laser welding to create a standard centre-line lap junction. The intermetallic layer generated at the intersection of two metals considerably lowered the joint's strength. A heat transfer analysis was performed using a finite element analysis technique to identify a method for controlling the depth and width of molten metal penetration, which aids in regulating the thickness of the intermetallic compound layer. Based on the FEM analysis results, edge-line welding of a lap joint was performed, resulting in easy control of the intermetallic layer's thickness and achieving high joining strength.

Zhou et al. [31] proposed a transient 3D heat transfer and melt flow to understand the keyhole collapse and melt solidification. It was reported that humping is caused by the combined action of two factors: high solidification rate and accumulation of the melt flow at the rear end of the keyhole due to the recoil pressure.

Fabbro et al. [32] investigated the effect of the contact between the vapour produced by the ablation process and the front keyhole wall. It was stated that the evaporation process is more significant at high velocities. The metallic vapour that hits the back keyhole wall opens the keyhole cavity. This collapse process is gradually controlled, and a suitable weld seam forms.

Kou et al. [33] investigated the aluminium samples, and the results reveal that decreasing the power value raises the welding speed required needed full penetration, hence increasing the penetration depth to bead width ratio and weld bead micro-hardness. According to the butt welding results, the tensile strength and total elongation qualities of the specimens with a high shielding gas flow rate are nearly three times higher than those with a low shielding gas flow rate. The higher test results are mainly due to the absence of hot cracking in the high flow rate specimens, a more refined microstructure, and reduced porosity. This study demonstrates that the effect of F on weld bead shape, microstructure, hot crack susceptibility, and mechanical properties is substantially more significant than that of P . However, the impact of altering welding speed is greater than that of a low flow rate.

Balasubramanian et al. [34] employed the finite element technique (FEM) to forecast the bead shape during laser welding of 1.6 mm thick AISI304 stainless steel sheets. A three-dimensional finite element model is used to investigate the temperature distribution in a T-joint and a butt-joint weld formed by the laser welding process. Temperature-dependent AISI304 stainless steel thermal properties, the effect of latent heat of fusion, and convective and radiative boundary conditions are all included in the model. The model's heat input is a 3D conical Gaussian heat source. An Nd: YAG laser with a maximum power of 2 kW in continuous wave mode is used to make the T-joint and butt-joint welds. Finally, the mathematically predicted molten pool morphologies are compared

to the experimental results. As the comparison shows, they are in good agreement.

Missori et al. [35] studied laser beam welding of C-Mn steel plates with nickel (Ni) powder as filler. Experiments are carried out, and the resulting data is fed into the neural network. The network calculates the amount of Ni present in the welded area. The goal of achieving optimum penetration with minimal powder loss is achieved by optimizing inputs such as the rate of powder addition and the joint shape.

Moraitis and Labeas [36] develop a thermomechanical finite element model for laser beam welding of aluminium lap joints that predicts residual stress and distortion fields. In this study, a keyhole model is employed to estimate the size and shape of the keyholes used for thermal analysis. On the other hand, the top and bottom sheets' contact heat flow is ignored.

Akman et al. [37] investigated welding parameters for connecting a 3-mm thick titanium alloy using the Lumonics JK760TR Nd: YAG pulsed laser. The pulse energy to pulse time ratio is essential in determining penetration depth. Variation in pulse duration with constant peak power has also been shown not to affect penetration depth. Consequently, the function of laser parameters such as pulse energy, duration, and peak power in joining 3mm thick Ti6Al4V has been investigated to improve welding penetration depth.

Ghaini et al. [38] studied the crack susceptibility of aluminium alloy 2024 during pulsed mode laser welding. The research was conducted better to understand solidification and fluid cracking. It was determined that the metal's parent material is related to the solidification cracks in the weld. The liquid backfilling phenomena have been studied regarding its impact on solidification cracking at the weld metal.

Amara et al. [39] studied deep-penetration laser welding at a high-welding speed regime, and a 3-D transient modelling based on the numerical resolution of the fluid flow and heat transfer equations is created, resulting in the humping phenomenon. This model includes physical mechanisms for matter melting, vaporization with recoil pressure, and resolidification. They tackled the problem

with specific and complex boundary conditions by implementing custom procedures known as User Defined Functions (UDFs) that interacted with the CFD Fluent code and a dynamic mesh approach. Therefore, recoil pressure, fusion, resolidification, and temperature dependency of physical parameters were considered. As a result, frequent humps on the weld seam could be seen following resolidification.

Amara et al. [40] proposed a deep penetration model for studying the effect of scanning speeds on humping. They adopted a dynamic mesh technique for simulating the melt pool. It was proposed that using the Bernoulli equation in the model enhances the hump dimensions.

Bachmann et al. [41] created a three-dimensional laminar steady-state computational model to explore the effects of an AC magnetic field on the weld pool dynamics and weld cross-section of a 20 mm thick aluminium plate in a flat situation in complete-penetration laser welding. The 3-D heat transfer, fluid dynamics with phase transition, and electromagnetic field PDEs were solved iteratively by COMSOL Multiphysics software, using the temperature-dependent material characteristics up to evaporation temperature. The Carman–Kozeny equation for porous media morphology was used to simulate solidification. The introduction of oscillating magnetic fields significantly altered the flow pattern in the melt and the temperature distribution. It has been demonstrated that applying an ac magnetic field to laser beam welding can eliminate gravity drop-out. The simulation outcomes are satisfactory.

Kalpan and Powell [42] explained spatter information and different types of spatter phenomena. They proposed a categorization technique to allow comparison and research on the spatter technique.

Turna et al. [43] explored the numerical simulation of thermal stress in tubes made of austenitic steel Cr Ni Steel the numerical simulation is validated with experimentation.

Volpp [44] created a quasi-static model of the keyhole made by laser welding. Here the keyhole geometry is calculated based on the spatial distribution of laser beam intensity, and the top-hat beam profile is employed. Further, the

numerical model is validated using the keyhole form produced by laser welding aluminium alloys.

Ilar et al. [45] used high-speed imagery of the melt pool to investigate root drop humping generated by droplet collection at the back end of the weld pool. Due to gravitational forces, the melt is pumped to the bottom of the keyhole.

Acherjee et al. [46] constructed a temporal numerical model based on conduction mode heat transfer to explore the effect of carbon black on temperature distribution and weld shape during laser transmission welding of polymers. The model's heat input is the volumetric Gaussian heat source. The modelling takes into account the temperature-dependent material properties of polycarbonate. The numerical results are acquired by executing a finite element code with ANSYS. The experimental results are compared to the numerically estimated dimensions of the weld pool. As a result, the model generated is also accurate enough to be used in the intended study.

Acherjee et al. [47] investigated the laser transmission-contour welding process utilizing the design of experiments and finite element analysis with ANSYS multi-physics. A 3-D thermal model is initially built to replicate the welding process with a moving heat source. The experiment design is then utilised with regression analysis to organize the experiments and construct mathematical models. The sensitivity analysis aimed to determine how different input variable values affect a specific output variable.

Enz et al. [48] investigated the effect of chemical composition modifications on mechanical properties such as strength and hardness. The effect of weld chemistry on the welding process is being explored to improve weld quality. It has been stated that the discrepancy in hardness and strength is due to the non-uniform distribution of lithium. According to studies, hot cracking is caused by silicon loss from the weld zone.

Courtois et al. [49] created a heat and fluid flow model with Comsol Multiphysics®, where the first stage involves simulating a static laser fired on a piece of steel. This 2D axial symmetric arrangement is used to investigate the critical physical processes involved in the development of the keyhole. This

model considers the vaporized metal, liquid phase, and solid foundation. The Level-Set approach is used to track the liquid/vapour interaction. The estimated velocity, as well as the free surface deformation, are investigated. When melt pool forms are compared to practical macrographs, the effect of various parameters, such as laser power, is investigated.

Courtois et al. [50] proposed that the simulation of laser welding procedures uses heat and fluid movements. This model was created entirely using a graphical user interface of a finite element computer. The model considers three stages: vaporization, liquidation, and solidus. A novel method for modelling energy deposition is provided, which involves treating the laser as a waveform and solving Maxwell's equations. They provided complete model validation and advice on what criteria to check. Several comparisons with specific experiments are provided to assess the model's validity.

Brock et al. [51] investigated vapour plume fluctuations during laser welding of steel sheets in lap joint arrangement. It was determined that as penetration depth increases, the position of the vapour plume shifts to the opposite direction of the welding. This displacement causes flaws such as blow holes and splatter.

Gao et al. [52] suggested a 3-dimensional numerical model explore the dynamic behaviour of the weld bead profile during high-intensity laser welding. Experiments are used to validate the numerical model. The proposed model discusses the interaction of welding process parameters with fluid flow, seam qualities, and mechanics equilibrium.

Akbari et al. [53] carried out numerical and experimental research on laser welding of titanium alloy (Ti6Al4V) to estimate the temperature distribution and forecast the heat-affected zone (HAZ), molten pool depth, and width. The intricate physical process that results in the formation of the keyhole has not been investigated. The experimental results and the finite volume thermal model were found to be in good agreement, also at different laser welding speeds, predicted temperature as a function of distance, and observed that the temperature profile declined dramatically near the beam centre, then declined modestly in the distant

region from the beam centre. The created model error was discovered to be between 2 and 17%.

Bachmann et al. [54] proposed a multi-numerical model to study the impact of a continuous magnetic field vertical to the welding direction throughout partial penetration of high-intensity laser welding of aluminium in the down hand position. COMSOL Multiphysics 4.2 successfully solved three-dimensional heat transfer, fluid dynamics with phase change, and electromagnetic field PDEs. Natural convection owing to the gravitational field, Marangoni convection on the weld pool's surface area, and the latent heat of the solid-liquid phase change were all taken into account. The Carman–Kozeny equation for medium absorbent morphology was used to simulate solidification. The computational results are in good accord with the experimental research findings with a 16-kW disc welding AlMg3. The magnetic flux density peaked at roughly 500 mT. It demonstrates that, regardless of polarity, the applied magnetic field has a substantial dissipating influence on the weld pool dynamics.

Bachmann et al. [55] examined the effect of externally imposed magnetic fields on laser beam welding quality. The findings of computer simulations were used to help optimize the process parameters. AC magnetic fields can reduce weld porosity by a factor of 10 compared to the reference joints in partial penetration welding tests with 4 kW beam power. The roughness of the weld surface was reduced by half, and investigated the effects of the AC magnetic field in keyhole welding with a laser using a 3-D turbulent steady-state numerical model with the help of COMSOL Multiphysics 4.2. The model included thermo-capillary (Marangoni) convection at weld pool borders, natural convection owing to gravity and density changes in the melt volume, and latent heat of solid-liquid phase transitions at phase boundaries. Welding experiments were carried out on stainless steel AISI 304 with a thickness of 20 mm and a laser beam power of 20 kW.

Lecoanet et al. [56] used COMSOL to do 3D finite element research to replicate the temperature profile produced by Rosenthal's method. The heat transfer formula used has been modified to approach Rosenthal's response. When the source and domain shapes are changed, the inconsistencies between the

simulation and Rosenthal's approach are investigated. The significance of thermal coefficients and C_p has also been studied.

Narsimhachary et al. [57] worked on a 2mm thick aluminium alloy 6061 using a CO₂ laser welding machine. Weldability, microstructure, and parameter selection were discussed to achieve a crack-free weld. Post-weld heat treatment was performed to enhance the hardness slightly. The temperature profile was determined, and the material's mechanical properties were found to have deteriorated with age.

Xiao and Zhang [58] discussed the drawbacks that creep up during the laser welding of Aluminium Lithium alloys. The formation and mitigation of defects like pores and cracks are investigated in this work. Microstructures, mechanical properties and future trends and discussed towards the end.

Zhang et al. [59] experimented on 2060 T8 Aluminium Lithium alloy fusion zone properties. Along with microstructure, the mechanical strength of the alloy is investigated. A filler rod of composition 5083 is employed to reduce crack formation. It was reported that an ultimate tensile strength of 317 MPA was obtained, which is 63% higher than the base material. The microhardness of the fusion zone is lowest due to the tensile fracture.

Alfiera et al. [60] studied welds with a high aspect ratio and reported that the welds generated less heat input than standard arc-welding techniques, resulting in increased productivity and lower distortion. Nonetheless, particular concerns must be addressed based on the material to be welded. This section discusses laser welding of AA 2024 in the T3 heat treatment state, which is one of the most common light metal alloys in aerospace. A complete assessment of variables influencing weldability is provided, combining ad-hoc experimentation with a Yb: YAG disk-laser source with existing knowledge in the relevant literature. As a result, several topics are being researched: the requirement for sufficient gas assistance, the irradiance threshold to be overcome for key-holing due to low absorptance, and tensile test on the specimens. Compared to other literature findings, significant results were obtained regarding heat-affected zone minimization and ultimate tensile strength.

Bachmann et al. [61] studied the influence of externally applied magnetic fields on laser beam welding quality. Welding experiments were carried out on stainless steel AISI 304 with a thickness of 20 mm and a laser beam power of 20 kW.

Chukkan et al. [62] used SYSWELD to conduct a thermo-elastoplastic investigation of category 316L stainless steel sheets in pulsed Nd-YAG Laser welding with three separate heat sources. The three heat sources employed were 3D conical, 3D conical with double ellipsoidal and 3D conical with cylindrical shell. Experiments accomplished validation of the simulated thermal cycles, residual strains, and deformation. The simulated heat cycles, the generated residual stress profiles, and the simulated distortion values were validated. The model predictions and experimental data agreed well. Compared to the other heat sources, the model using a 3D conical with a cylindrical shell heat source predicted the thermal cycles, residual stresses, and deformation more accurately.

Pang et al. [63] introduced a new 3D transient model with multiple phase consideration for deep penetration laser welding utilizing a fibre laser, describing a self-consistent keyhole, metallic vapour plume in the keyhole, and weld pool dynamics. Surface tension, recoil pressure, Marangoni shear stress, Fresnel absorption processes, heat transmission, and fluid movement in the weld pool are all considered, as are keyhole-free surface evolutions and solid-liquid–vapour three-phase transitions. Weld bead dimensions, weld pool dynamics, vapour plume dynamics, and transient keyhole instability are predicted, and excellent agreement with experimental and literature data is obtained.

Sheikhi et al. [64] conducted several bead-on-plate experiments and worked on laser welding of AA 2024. It was reported that the solidification and liquation cracking of the samples was severe at high pulse width and peak power.

Zhang et al. [65] performed full penetration laser welding on a 10 mm steel plate using a 16-kW maximum power continuous wave thin disk laser. To simulate the dynamic interaction between the keyhole and molten pool in laser full penetration welding, a three-dimensional laser deep penetration welding model was utilised, in which the volume of fluid (VOF) approach was merged with a

ray-tracing technique. On both the upper and lower sides, the estimated weld cross-section morphology and molten pool length accord well with experimental data

Zhang et al. [66] performed experiments on aluminium alloy 2060-T8 Alloy using an Al-Si filler rod. Due to this, the fusion zone displayed a dendritic solidification structure. The microstructure and mechanical properties are studied, and a tensile strength which is 80% more than that of the base material was reported

Atabaki et al. [67] investigated the partial penetration mechanism in AA5083 during autogenous welding. The effect of process parameters such as speed, peak power, and surface qualities on porosity creation and mitigation is investigated. A 3D finite element model is also proposed to investigate the welds' heat history. Helium was found to minimize the creation of pores when welded at low speeds. Pores form as a result of shield gas trapping as the keyhole collapses.

Bakir et al. [68] created a three-dimensional finite element model that mimics the formation and propagation of solidification fractures during laser full penetration welding of fully austenitic stainless steel using the contact element methodology. The percentage is 1.4376. During experimentation, the strain and displacement on the laser beam in the vicinity of the weld pool were measured. Experiments confirmed the model's predictions for local strain fields, global loads, and fracture lengths.

Courtois et al. [69] created a heat and fluid flow model with Comsol Multiphysics® involving the simulation of a static laser fired on a piece of steel. This 2D axial symmetric arrangement is used to investigate the essential physical processes involved in the development of the keyhole. This model considers the vaporized metal, liquid phase, and solid foundation. The level-Set approach is used to track the liquid/vapour contact. The estimated velocity, as well as the free surface deformation, are investigated. When melt pool forms are compared to practical macrographs, the effect of various parameters, such as laser power, is investigated.

Otto et al. [70] investigated the mechanism of humping generation during micro welding. Because of the solidification mechanism in thin sheets at very high welding speeds, this work is crucial. The fluid dynamics technique and the Plateau-Rayleigh instability of the liquid jet are used to discuss the occurrence of humping. Experiment findings are used to validate the model.

Ahn et al. [71] investigated the aluminium alloy 2024 using 4043 as a filler rod in many trials. The loss of volatile elements such as magnesium, copper, and silicon is thought to cause cracking. Higher feed rates caused weld pool instability, whereas lower feed rates did not affect weld pool chemistry. Using a filler rod reduced the number of defects that occurred during welding. The tensile strength was also increased with the addition of a filler rod.

Ai et al. [72] created a three-dimensional numerical model to investigate the characteristics of the weld formed in laser keyhole welding with a fibre laser. The gas layer above the molten pool was used in the simulation model to simulate the weld's top surface, and the free surface form of the keyhole was estimated using the volume of fluid technique. The evolution of the weld shape features was provided using numerical simulation results, which were utilised to determine the shape and sizes of the generated weld bead. According to the comparison, the expected outcomes of the weld bead correspond well with those of the experiments.

Ostuni et al. [73] investigated the performance of 2D and 3D Gaussian heat sources for thermal analysis of Titanium and AL dissimilar fibre laser welding. The numerical model was validated by testing. It was determined that a 2D heat source provided a better thermal field than a 3D heat source. When cooling rates were investigated, it was discovered that 3D heat sources were more precise compared to the 2-D source. The proportions of the weld pool's fusion zone shape were correct in both 2D and 3D heat sources.

Hong and Shin [74] thoroughly explained lightweight materials and their applications in high-volume vehicle manufacture. Various welding processes are discussed. It was determined that laser welding has a better future than other

approaches. The feasibility of incorporating microstructure changes and faults that occur during laser welding is thoroughly investigated.

Liebl et al. [75] have constructed a numerical model using the adaptive-intensity distribution technique. The impact of this innovative approach on process properties, temperature history, and molten pool geometry has been investigated. Experiment data is used to validate the proposed procedures. While developing this model, the Marangoni forces and recoil pressure are also considered. It is concluded that the procedure significantly minimized the hot cracking phenomena.

Meco et al. [76] studied the heat cycle used during the joining procedure to determine the integrity of steel-aluminium dissimilar alloy junctions. The temperature field has a direct influence on the formation of intermetallic compounds (IMC) formed by the reaction of iron (Fe) and aluminium (Al), but it also controls the size of the joint's bonding area. A finite element (FE) thermal model was created to predict the transient thermal cycle at the Fe-Al interface for varying applied energy levels by varying power density and contact time. The weld geometry, IMC layer thickness, and mechanical strength were all associated with the time-temperature profiles. The experimental results revealed that having a small bonding area is just as bad for the mechanical strength of the joint as having a large bonding area.

Longinava et al. [77] studied the influence of pulse laser welding settings and filler metal on the microstructure and the novel cryogenic heat-treatable mechanical properties Al-4.7Mg-0.32Mn-0.21Sc-0.1Zr alloy was examined. The optimal pulsed laser welding settings were discovered. They had a voltage of 330-340 V, pulse overlaps of 0.2-0.25 mm with a length of 12 ms, a speed of 2 mm/s, and a ramp-down pulse form. It was reported that pulsed laser welding without and with Al-5Mg filler metal produced duplex (columnar and fine grain) as-cast structures with hot fractures and gas porosity as weld zone defects. Welding with Al-5Ti-1B filler metal created a fine grain structure with an average grain size of 4 0.2 μ m and no weld flaws. The ultimate tensile strength is equal to the base metal.

Ng et al. [78] studied the usage of light metal alloys, the production of aluminium alloys, and their applications. This work extensively reviewed the available aluminium alloys, their use in several automotive applications, and the issues associated with heat treatment.

Sanchez-Amaya et al. [79] investigated titanium alloy's microstructure and mechanical properties. When tested for ultimate tensile strength, this conduction mode weld possessed approximately 78 per cent of the base material strength compared to a critical hole weld.

Shen et al. [80] proposed a continuum damage mechanics approach and studied the fatigue damage evolution of butt-welded joints under cyclic loading. A coupled thermal-mechanical analysis is performed to analyse the residual stresses caused by welding procedures, which are used as the beginning state in the fatigue damage analysis. An elastoplastic fatigue damage model that considers the porosity-induced stress concentration in the weld zones is created to examine the damage evolution of joints. The fatigue lifetimes of these joints with various pore conditions are predicted and agree with the experimental results. The residual stress level is discovered to decrease as a result of the combined impacts of the damage from fatigue

Svenungsson et al. [81] implemented a multi-phase Thermo-fluid model for keyhole laser welding. The model is validated by comparing the results with published test cases. The model predicts porosity by using Marangoni convection.

Xue et al. [82] investigated the impact of pulsed Nd: YAG laser beam welding settings on DP1000 butt joint penetration and microstructure characterization. Process factors such as sample preparation, proper fixture use, and adequate shielding gas parameters are set to achieve consistent welding. As a result, peak power, pulse width, and beam diameter significantly impact penetration, with peak power influencing penetration by up to 60%. ANOVA was used to determine the model's significance.

Ahn et al. [83] studied the impact of shielding gas on weld quality, defect formation, and microstructure. A comparison of the effects of He and Ar on weld

quality is made. The occurrence of defects such as undercut, porosity, underfill, reinforcement, and weld dimensions are explored when using each shielding gas. Both Ar and He produced good welds. However, He was more suited at low welding speeds due to its strong ionization capability, while Argon produced good overall weld quality.

Artinov et al. [84] created a computational framework for modelling steady-state thermal behaviour in keyhole welding. The main theoretical concepts, such as keyhole shape, thermo-capillary and natural convection, and temperature-dependent material features, are considered. The developed technology is utilised for complete penetration of keyhole laser welding on a 15 mm thick low-alloyed steel plate at a welding speed of 33 mm/s and laser power of 18 kW.

Fetzer et al. [85] used X-ray videography to examine bubble generation and collapse mechanisms in an aluminium Magnesium Silicon alloy. The melt pool was examined, and the geometry of the vapour capillary was measured at various input rates. The velocity fields inside the melt pool are constant at increased feed rates, which reduces pore formation.

Fotovvati et al. [86] conducted a literature review on laser welding experimental and modelling research, focusing on the impact of process parameters on melt-pool geometry, thermodynamics, fluid dynamics, microstructure, and porosity features. These findings could guide future experimental laser welding research and verify and validate outcomes.

Maina et al. [87] proposed strategies to increase keyhole stability during laser welding. It was discovered that dual-mode welding, which provides good temperature distribution and stabilizes the welding, may produce high-quality welds with sufficient deep penetration.

Panwiswas et al. [88] experimented with titanium alloy and developed a three-dimensional computational fluid dynamics model by considering all the relevant physics.

Patschger et al. [89] evaluated the creation of humping by taking into account characteristics such as volume flow rate, peak power, diameter in focus, welding circumstances, dimensions, and material thermophysical properties.

Artinov et al. [90] developed a three-dimensional numerical model for predicting the transient thermal cycle before and after fusion welding. So the modelling process was split in two. Initial simulation of complete-penetration keyhole laser welding in 15 mm low-alloyed steel plate with 18 kW laser power and 2 m/min welding speed was done. The energy absorption test and the model calibration used a fixed keyhole with a round cone shape. The effects of phase transition, thermo-capillary convection, natural convection, and temperature-dependent material characteristics were considered in computing the weld pool shape and the local temperature field. COMSOL Multiphysics 5.0 was used to solve a collection of PDEs that describe stationary heat transport and fluid dynamics. The transient heat transfer simulation used the node's temperature as an energy input which recreated the predicted local temperature field describing the equivalent volumetric heat source. Their translational motion was simulated using a moving mesh approach. It was used to smooth the polygonal mesh's elements' locations. The correlation between the computed and observed weld bead morphologies and transient temperature distributions was strong.

Mehrpauya et al. [91] created a numerical model to predict the best laser parameters for reducing the HAZ and FZ. Artificial neural networks were used as a tool to do nonlinear mapping between welding process inputs and outputs.

Ghosh et al. [92] investigated the 2205 Duplex stainless steel butt joint's laser welding process using the finite element approach, COMSOL Multiphysics, and statistical methodologies. The study's purpose was to investigate the effect of process variables on the development of the thermal field and the formation of weld bead shapes. RSM creates second-order equations to predict reactions accurately. Multi-objective optimization of weld width and penetration depth is carried out.

Cao et al. [93] developed a data-driven model for measuring weld seam during laser beam welding in the presence of magnetic fields. A radial basis function and backpropagation are used to simulate the system. A generalized regression neural network is proposed To link laser melt pool properties with the keyhole and the weld. According to the results, the suggested model efficiently monitors

the weld beam and modifies the process parameters in real-time to increase weld quality.

Feng et al. [94] developed a three-dimensional model using the ray-tracing approach. The multiple penetration states of laser-welded steel components are investigated in this model. It is concluded that the dynamics of the molten pool influence the penetration status and that keyhole, flow field, and temperature field are related to joint quality.

Moges et al. [95] proposed a data-driven integrated strategy for describing the relationship between process structural features and performance. Using artificial neural networks, the model combines data from simulation and testing to forecast melt pool width. This study is being hailed as a significant step forward in using hybrid models for prediction with enhanced accuracy.

2.3 Review of literature on optimization techniques in welding

Luo et al. [96] used an artificial neural network to detect welding defects. After extracting features from acoustic data and feeding them into the network, the network could distinguish between typical and defective welds.

Shanmugarajan et al. [97] used Taguchi basis grey relational analysis to optimize the laser welding process for P92 material. ANOVA is used to determine the effect of various parameters on the reaction. The results of the grey relational analysis are tested empirically.

Jiang et al. [98] investigated laser welding parameters optimized using the finite element method, a non-sorted genetic algorithm, and the Kriging method. Several processes' primary effects and contribution rates on the welding bead profile are investigated. When the inputs include laser power, welding speed, and focal length, the findings show that the optimal process parameters are reliable in calculating the weld bead profile.

Bagchi et al. [99] presented a numerical model to study the effect of welding speed, pulse energy and frequency on the aspect ratio and peak temperature. The optimal parameters for attaining the objectives are determined using a signal-to-

noise ratio. The simulated results are correlated with regression models and artificial neural network models. The macrographs obtained from experiments are in line with numerical simulation.

Zhao et al. [100] studied the ultrasonic welding process on different magnesium-titanium alloys to investigate the effects of welding settings on joint strength. The analysis of variance was used to investigate the importance of each welding parameter and its relationships. An artificial neural network (ANN) was used to predict joint strength. The results show that clamping force is the most critical factor in the ultrasonic welding of magnesium and titanium alloys, followed by vibration time and vibration amplitude; interactions between vibration time and vibration amplitude, as well as between vibration amplitude and clamping force, also have a significant impact on strength. Test data were utilised for training an artificial neural network, which was then used to predict the fluctuations in joint strength under different conditions.

Wang et al. [101] studied multi-response Gaussian process regression. A direct definition of the covariance function for multiple replies is proposed, and numerical examples are provided.

Lei et al. [102] proposed a fused neural network as an input with weld settings and melt pool characteristics. This model predicts the geometric features of weld beads. Principles component analysis is utilised to eliminate feature repetition. A genetic algorithm maximizes the initial weights required for training neural networks. Because the extraction time is less than 90 ms, it can be employed in large-scale real-time thin plate welding applications.

Zhang et al. [103] used deep learning algorithms to create a system for detecting porosity during laser welding. A convolutional neural network technique with compact architecture was used to understand the pattern changes in the weld pool for predicting porosity. The model detected porosity generation with 96.1 per cent accuracy.

Yusof et al. [104] proposed a weld penetration estimation model developed from the sound features extracted from the signal acquired during pulsed mode laser

welding. The predictive variable for the estimation model was identified using features selection analysis.

Oh et al. [105] suggested a deep learning model for predicting laser beam absorption capacity in keyhole laser welding by creating several hypothetical keyhole shapes. The network's optimal architecture estimates absorption capacity with an R^2 accuracy of 99.76 per cent.

Li et al. [106] created an artificial neural network model to forecast the geometry of the weld seam under variable scanning speed conditions. As a result, it was determined that a network with the structure 33-6-2 produced good accuracy in both the training and testing phases.

2.4 Research status on laser welding of aluminium alloy

AA 2024 is regarded as un-weldable material using traditional arc welding processes. This difficulty in traditional processes limits the use of the alloy in stress environments for which it is suitable. Laser welding of aluminium alloys dates back to the 1980s. [107] performed several trials on 6.4 mm thick aluminium alloys 5456 and 1100 on CO₂ laser at low power of 0.2kW and 1.3 kW. It was reported that joint configuration and surface conditions influence the absorption of the laser beam. Several researchers [108, 109] worked on aluminium alloys 5182, and 5757 using Nd: YAG and CO₂ laser welding machines and suggested welding parameters required to attain consistent welds. Till 2000, alloys 2008, 2010, 5083, 5182, 5283, 2456, 6013, 6061, 6063, and 6111 came into prominence, and a number of publications were made on these series [109]. A significant amount of research has been carried out on laser welding of 5xxx and 6xxx series of aluminium alloys using CO₂ and Nd: YAG lasers over the past decade, owing to the weldability and lesser crack susceptibility [110-117]. Publications on the 7xxx series of aluminium alloys, like laser welding of 7075 [48,112,118,119], came up. Though research on other series of aluminium appeared frequently, the work on AA 2024 is minimal. [120] 4Kw Nd: YAG laser welding machine to weld 13 mm thick component. It was reported that only partial penetration was achieved. [121] performed laser welding on 3mm thick specimens of AA 2024 in autogenous mode. Severe keyhole instabilities were

reported to have been observed at low input power, which gave poor weld bead with high porosity. The welding process was also reported to be more stable at high peak powers. Keyhole instability is due to high reflectivity, high heat intensity, and low boiling point elements like magnesium. These factors necessitate process optimization. [61] employed a diode laser to attain bead-on-plate welding on 2mm thick AA 2024 components and the components from other series. It was observed that only 2024 possessed poor weldability regarding penetration depth and crack susceptibility. Other works reported by [61,122,123] also indicated poor weldability of the AA 2024 components. Proper edge preparation and defocussing were two techniques suggested to improve weldability and reduce porosity. The higher power and defocussing lead to lesser porosity due to the improved convection vortex in the weld leading to keyhole stability. Tensile strength of 2/3 times greater than the base material was attained, making it suitable for industrial applications.

2.5 Motivation for the present research

In the past few years, laser beam welding of aluminium alloys has become a much sought-after technique for obtaining good-quality welds. Several researchers investigated both the experimental and microstructure aspects and applied numerical simulation to achieve good quality and control over the process. The progress in numerical techniques and improvements in high-speed computing techniques has allowed complicated calculations to be performed in a relatively short period with acceptable accuracy. Theoretical analysis of laser beam welding has gained prominence among researchers in the recent past, employing analytical and numerical methods to study various aspects of this technique. Numerical methods can explain the physics of some complex welding phenomena and process optimization. Finite element analysis is one of several numerical methods used to solve complex problems and is the dominant method used today. Some three-dimensional models have been developed to gain insight into the thermal history and defects during the welding process [6,9,11,26,31]. However, there is vast scope for refining these models and investigating additional parameters. Also, the studies on the aluminium alloy 2024 are just a handful. A comprehensive study on AA 2024 is imperative regarding the

importance and application of the material in the industry. The analytical models proposed in the available literature can be enhanced by introducing the temperature-dependent material properties, introducing the coupled physics and defining the parameters beyond vaporisation temperature, using Multiphysics to define the loading and boundary conditions. Therefore, an enhanced three-dimensional transient thermo fluid model of laser beam welding is much needed to study the effect of process parameters on temperature distribution and formation of weld profile, Marangoni convection and its impact on weld metrics and formation of defects during laser welding of AA 2024. The thermo-fluid model has been defined on various materials earlier, but a model simulating the behaviour of AA 2024 has not been attempted.

AA 2024 is an essential material in the light metal category and attempts to enhance the weldability of the material are imperative. The thermophysical properties of the target material play a key role in influencing the quality of the welded components. These components suffer from hot cracking, porosity, undercut, lack of penetration and humping once they are welded. Simulation of the process, experimentation and optimization is performed to reduce the formation of defects and increase the quality of the weld. A literature review of experimental studies reveals solidification cracking, incomplete penetration, and porosity. It is evident from the literature that the usage of filler material improves the weld quality, but most laser welding machines work in the autogenous mode. It is also observed that the shielding gas and thickness of the metal influence the welded joint. The critical process parameters are peak power, scanning speed, frequency and pulse width. These parameters control the temperature field inside the weld area and the quality. Edge preparation and pre-welding treatment do also have significant effects on weld quality. Many experimental research works have been carried out to study the influence of process parameters on weld quality with various materials [31,33,37,43]. But this type of investigation on AA 2024 is not available. Investigators have mainly considered the process parameters along with shielding gas on the laser welding of metal alloys. Most works were performed without the proper experimental design; hence, the results are far from optimum. The combination of process parameters should be selected carefully to get desired weld quality. Extensive work is therefore needed to

analyse and optimize the process parameters to understand the effect on the weld metrics. So far, no comprehensive study has been done on welding aluminium alloy 2024, which is highly useful in the aerospace and defence sectors. Modelling and optimization of laser beam welding of this material would be a potential area of interest.

2.6 Objectives of the present research

Keeping in view the past research works and the present need for research on laser welding of aluminium alloys, the objectives of the present work are as follows:

1. To develop a three-dimensional, transient, thermo-fluid model to simulate the laser welding process.
 - a. To study the temperature distribution during welding.
 - b. To estimate the weld pool dimensions.
 - c. To study the effect of Marangoni and non-dimensional numbers on weld geometry.
 - d. To analyse the influence of process parameters on the temperature profile and weld metrics.
 - e. To study the effect of non-dimensional numbers on the weld profile.
2. To extend the developed finite element model to study the formation of welding defects like humping.
3. To conduct an experimental investigation of laser welding of aluminium alloy 2024
4. To conduct numerical models based on experimental results
5. To identify the effect of process parameters on weld width and depth of penetration
6. Study the microstructure of the heat-affected zone, fusion zone and base material.
7. To predict the weld metrics using deep learning techniques
8. To establish and implement process optimization.

Chapter 3: Materials, Experiments and testing

3.1 Introduction

The materials used in the laser welding process and the significance of the target material are discussed in this chapter. The investigation of input process parameters influencing the laser weldability of materials is described, along with the characteristics of the selected material. A detailed description of the study's laser welding equipment and the pre and post-welding processes is given. The theory related to the methodologies used in the present study, like finite element analysis, response surface methodology, gaussian process regression, and particle swarm optimisation, are described with the necessary equations.

3.2 Materials

Aluminium alloys

Aluminium alloys are cost-effective in a wide variety of applications. They are used in the automotive and aerospace industries, in the construction of machines, equipment, and buildings, as kitchen utensils, as covers for electronic equipment housings, as cryogenic pressure vessels, and in an infinite number of other applications.

3.2.1 Grouping of aluminium alloys

Aluminium alloys are grouped into two categories: wrought and cast alloys

Wrought alloys are classified as follows:

1xxx series: Alloys in this series are of the highest purity. This alloy has applications in the chemical industry and electrical and electronic industries. They have the highest corrosion resistance and high thermal and electrical conductivity. Though they have good workability, they possess poor mechanical properties. Processes like strain hardening increase strength moderately.

2xxx series: Copper is the primary alloying element. Magnesium is also added as secondary material. Often solution heat treatment is needed to attain better mechanical properties. Precipitation hardening increases the mechanical properties further. 2xxx series materials are best used when the structures need

a high strength-to-weight ratio. Typical applications include wheels of aircraft and trucks, suspension parts, fuselage, wings and skin, and structural parts that must withstand high temperatures.

3xxx series: The principal alloying element is manganese. Alloys in this series are non-heat treatable and possess the strength of more than 1xxx series alloys. The popular alloy in this series is 3003, employed in applications requiring moderate strength and good workability.

4xxx series: These series are alloyed with silicon which is generally added up to 12%. The addition of silicon lowers the melting range without giving brittleness. Hence, they are used as filler rods during welding and brazing. Most of the alloys in this series are non-heat treatable. The popular alloy in this series is 4032, which has a low coefficient of thermal expansion and is used in engine pistons forged.

5xxx series: magnesium is the critical alloying element in this series. When this element is used along with manganese, it gives strength that ranges from moderate to high. This series of alloy possess good welding characteristics. They are used in marine applications due to their corrosion resistance. These alloys are prone to cracking due to stress corrosion.

6xxx series: The alloys are heat treatable by adding the required amount of silicon and magnesium, forming magnesium silicide. These alloys have good machinability, weldability and resistance to corrosion.

7xxx series: The alloying element Zinc gives high strength when combined with magnesium. Elements like copper, chromium, and Scandium are added in small quantities to attain necessary properties like fracture toughness. The aircraft structure, mobile equipment and other parts that undergo stress are manufactured with this alloy.

8xxx series: The materials in this series are alloyed according to the requirement and applications. When the need is good performance at high temperatures, dispersion strengthened aluminium-iron-copper alloys are used. The elements are made using a powder metallurgy process.

3.2.2 Factors that affect the laser weldability of alloys

The weldability of any sample depends on four factors

- i) Work sample: The thermo-physical properties of the model, along with the dimensions, influence the outcome of the weld. The joint set-up and the clamping pressure also decide the joint's quality.
- ii) Laser: Properties of laser-like beam characteristics, wavelength and beam diameter affect the weld quality
- iii) ambient conditions: Atmospheric temperature, pressure and humidity affect the surface of the work sample, which in turn affects the joint quality
- iv) Process conditions: The input process parameters like scanning speed, focussing distance, the orientation of the beam, and shielding gas properties influence the outcome of the weld.
- v) **Figure 3.1** shows that the fishbone diagram (Ishikawa diagram) explains the various factors influencing weld reliability.

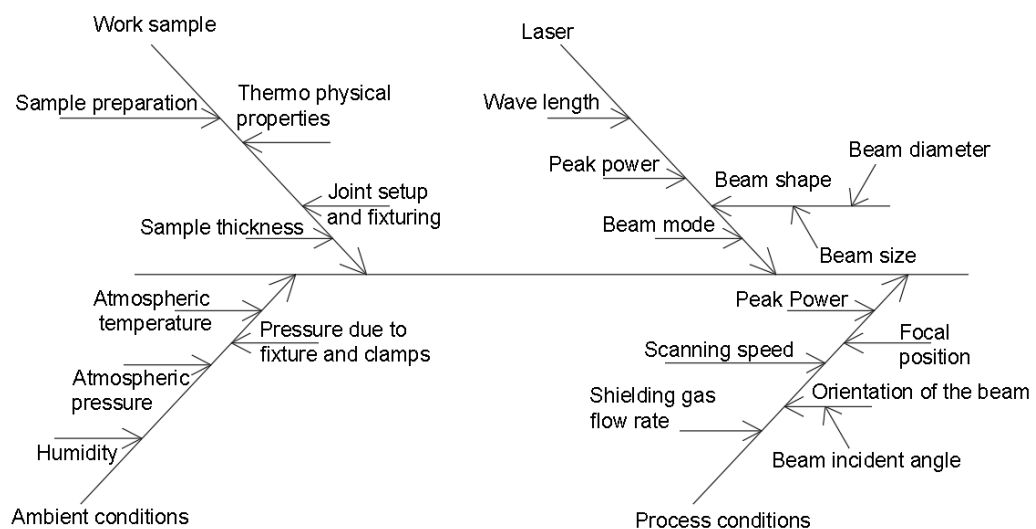


Figure 3.1 Factors affecting the weldability of alloys

3.2.3 Laser weldability of aluminium alloys

Laser welding offers many advantages over conventional joining techniques. The welding reliability of aluminium alloys is still low compared to other alloys due to the thermo-physical properties like high thermal conductivity, low viscosity and high reflectivity [124]. The thermal conductivity depends on several factors like the operating temperature, properties of the alloying elements

and the heat treatment. The thermal conductivity of pure aluminium is very high. Hence it evokes rapid heat transfer while welding with a laser. Thus the heat diffuses to the entire workpiece instead of focussing on the joint, which requires higher fluence to attain the melting temperature. Alloying elements like silicon, zinc and magnesium alter the thermal conductivity to a favourable range influencing the weldability. The addition of silicon reduces the thermal conductivity, qualifying it as a laser weldable alloy. Adding magnesium and zinc reduces aluminium's boiling point; hence, it becomes easier to attain keyhole when these are the principal alloying elements [125]. [126] conducted several studies on the alloying elements of aluminium and their impact on weldability. It is concluded that elements like silicon, magnesium and zinc reduce the thermal conductivity of the alloy and melting temperature, thus making it suitable for laser welding.

The second property that reduces the welding reliability of aluminium alloy is high reflectivity. The radiation absorption capacity of the alloy depends on the wavelength of the incident radiation and the surface properties of the specimen under consideration. It is reported that the absorptivity of laser radiation by aluminium alloys is high in the case of high-power diode laser rather than CO₂ laser [127]. However, the reflectivity of the aluminium alloys is almost 80%, irrespective of the laser employed for welding. Modification of surface roughness by way of sandblasting or application of a dark coating or texturisation helps in increasing the absorption capacity of the alloys [126]

The third property that reduces the weldability of aluminium alloys is the low viscosity of the weld pool. This property hampers the expansion of the weld pool before it solidifies. This property is cited as a persistent disadvantage while welding aluminium alloys.

3.2.4 Characteristics of aluminium alloy 2024

The first stage in analysing the characteristics of laser welded aluminium alloys is determining the effect of the alloy's composition, heat treatment, and thermal and physical properties. Consequently, a study of the characteristics of the material is the first step toward evaluating the weld samples.

Composition

The aluminium alloy under consideration belongs to the 2xxx series of wrought alloys. Copper is included in aluminium-copper alloys as a solid solution boosting the material's strength. Bulk strength is provided by the copper aluminide used in the alloy. It is present in grain as a fine and uniformly dispersed submicroscopic residue, which is then aged and heat treated. Aluminium alloys with a copper composition of 2-4% are exceedingly sensitive to hot tearing, to the point where the 2XXX was considered un-weldable. However, increasing the copper content to 6% or more significantly enhanced weldability due to the abundant eutectic available to back-fill hot cracks as they developed. Welding has the effect of re-dissolving the residues, resulting in a loss of up to 50% of ultimate tensile strength in a T6 condition alloy. Artificial ageing of the weldable alloy 2219 (AlCu6) can restore part of this reduction of strength, although a decreased flexibility generally accompanies this. The optimum results in this alloy need complete solution treatment and ageing following welding, which is not always available in a wholly manufactured structure. The less weldable alloy 2014 (Al Zn Mg Cu) can also be heat treated to regain some tensile strength. However, the recovery is smaller than with 2219 (AlCu6) and may result in an even more significant loss of ductility. Due to the availability of filler metals with comparable compositions, such as 2319 (AlCu6), weld metal strengths may be matched to the qualities of the HAZ. The design of the material under consideration, as given by the material vendor, is shown in **Table 3.1**.

Table 3.1 Chemical composition of the aluminium alloy 2024

Material	Cu	Mg	Mn	Fe	Si	Zn	Ti	Cr	Other	Al
% Composition	4.9	1.8	0.9	0.50	0.50	0.25	0.15	0.10	0.05	Remainder

Significance of the alloying elements

- *Copper*: Copper is the most significant alloying element in AA 2024. The presence of copper significantly enhances the strength. It contributes

to the alloy's precipitation hardening. However, the primary disadvantage is the reduction in corrosion resistance, ductility, and weldability.

- *Magnesium*: Magnesium enhances strength through solid solution strengthening and works hardening capabilities.
- *Silicon*: Silicon improves strength, ductility, and precipitation hardening.
- *Manganese*: This element strengthens solid solutions and enhances work-hardening ability.

3.2.5 Thermo physical properties of AA 2024

The thermos-physical properties of the aluminium alloy considered in this work are given in **Table 3.2**.

Table 3.2 Properties of AA 2024

Thermophysical properties	Value
Solidus temperature (K)	847
Liquidus temperature (K)	933
Vaporisation temperature (K)	2520
Specific heat (Solidus) (J/(kg.K))	1050
Density (solidus) (kg/m ³)	2660
Density (liquidus) (kg/m ³)	2380
Thermal conductivity (solidus) (W/(m.K))	235
Thermal conductivity (liquidus) (W/(m.K))	90
Latent heat of fusion (J/kg)	3.87×10^5
Surface tension (Nm ⁻¹ K ⁻¹)	-1.55×10^{-4}

3.3 Experimental details

3.3.1 Laser welding equipment

A 300W Nd: YAG laser welding equipment with a wavelength of 1064nm, installed at the school of laser science and engineering at Jadavpur university, is employed for AA 2024. The set-up used for the current research work is given in **Figure 3.2**



Figure 3.2 Laser welding set-up

Throughout the welding trials, the 300W pulsed laser welding machine is employed. The device can accommodate 32 distinct weld schedule parameters using waveform control. The system's low energy loss ensures that each delivery produces almost identical output power. The output of the shielding gas is coaxial with the outcome of the laser beam.

The welding system's primary components are the front cover, the up cover, the front gate, the right gate, the left gate, the back cover, the fibre fixation frame, the emergency stop switches, and the laser switch. The components are depicted in **Figure 3.2**.

A controlling unit is placed separately from the components shown in **Figure 3.2**. Its panel has the options shown in **Figure. 3.3**



Figure 3.3 Main menu tab of the laser welding machine

This tab in **Figure 3.3** helps in setting the time, date, and number of good shots to Control the pulse frequency and process parameters that are needed to control the welding machine.

Welder mode: The welder mode tab, as shown in **Figure 3.4**, allows for the modification of welding parameters. Variables on this machine include peak power, frequency, pulse width, and scanning speed.



Figure 3.4 Welder mode tab on the laser welding machine

System work mode: This tab is a sub-tab from the welder mode and displays the system's status. While welding, a high voltage should be used. Additionally, the total number of shots taken till the machine shot is displayed. **Figure 3.5** shows different options available in system work mode.

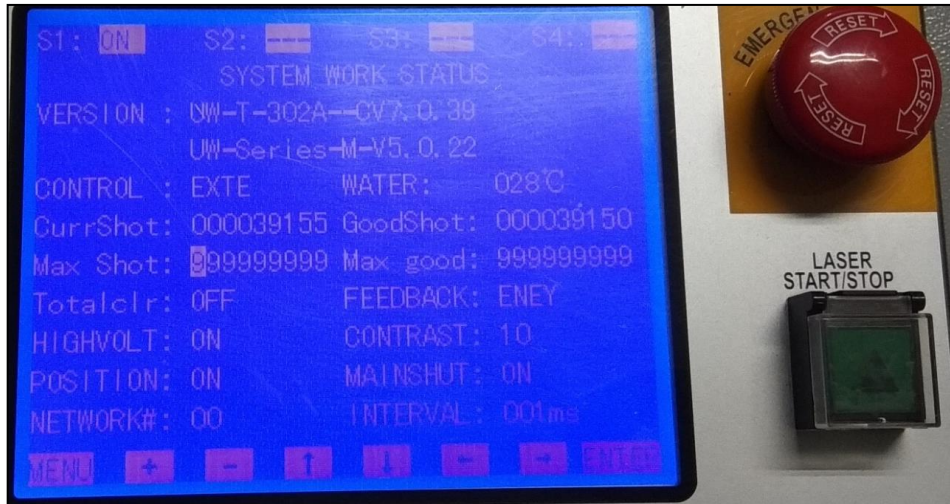


Figure 3.5 Work status of laser welding machine.

Chiller unit: The cooling system for this welding set-up is water-cooled. A chiller unit is installed to keep the laser system's temperature within a safe operating range. The chiller unit is shown in **Figure 3.6**.



Figure 3.6 Chiller unit of laser welding machine

3.3.2. Technical data of the welding machine

The power, frequency, pulse diameter and the related data of the machine are mentioned in **Table 3.3**.

Table 3.3 Technical details of the laser welding machine

Average power	300 W
Peak power	6 kW
Pulse energy	60 J
Pulse duration	0.5-50 ms
Pulse frequency	Max 100 Hz
Welding spot diameter	0.6 mm (fixed)
Focusing optics diameter	150mm
Pulse shape	Adjustable
Workpiece motion	Fixed
Scanning speed	Max. 25 mm/s

The first step is to conduct bead-on-plate studies to determine the range of parameters within which a suitable weld can be obtained from the target material. After each trial, the findings are analysed to determine practicable process parameters for the next step. Once the range has been determined, the response surface methodology is used to carry out the design of experiments. The present work studies the weld metrics in butt joint configuration.

3.3.3 Experimental design

The parameters and limits employed in the design of experiments are given in **Table 3.4**.

Table 3.4 Process control parameters and their limits used in the butt joint experiments

Parameters	Units	Notations	Limits				
			-2	-1	0	+1	+2
Peak Power	kW	<i>A</i>	4.00	4.25	4.50	4.75	5.00
Scanning Speed	mm/s	<i>B</i>	1.0	1.4	1.8	2.2	2.6
Frequency	Hz	<i>C</i>	6	7	8	9	10
Pulse Width	ms	<i>D</i>	5	6	7	8	9

3.3.4. Pre-experimental procedures

The following are different steps involved in sample preparation [128]:

Step 1: Collection of samples

The samples are cut to the necessary size from the supplier's long bars. The following sample dimensions are required for butt joint and lap joint welding of Aluminum alloy 2024: 75mm x 25mm x 2mm. The dimensions for spot welding are 75mm x 25mm x 0.25mm in length, width, and thickness.

Step 2: Edge preparation

The samples are mechanically filed with a rough file and then finished with a single cut file. Later, the samples are polished using a lapping machine for a smooth finish.

Step 3: Surface preparation

The specimen surface is cleaned with a stainless-steel wire brush and then with 99.99% pure acetone of industrial grade to ensure it is spotless. Cao et al. [129] reported that the quality of the surface influences the absorption of the laser beam incident on the samples during the welding. After the oil and grime have been removed from the samples, they are submerged in 30 % concentrated Hydrofluoric acid for less than 2 minutes to eliminate the oxide layer that has formed. After that, the samples are cleaned with water and dried before they are ready for welding.

3.3.5. Experimental procedure

Welding is performed parallel to the rolling direction of the sample as per the guidelines laid by the American welding society C7.2 document, ISO recommendations and BS EN recommendations [130, 131, 132]. The welding parameters explored in this study are peak power, scanning speed, pulse width and frequency. Argon is used as a shielding gas at a pressure of 3 bar and as a backing plate. **Figure 3.7** shows the welding set employed during the welding of AA 2024 samples.

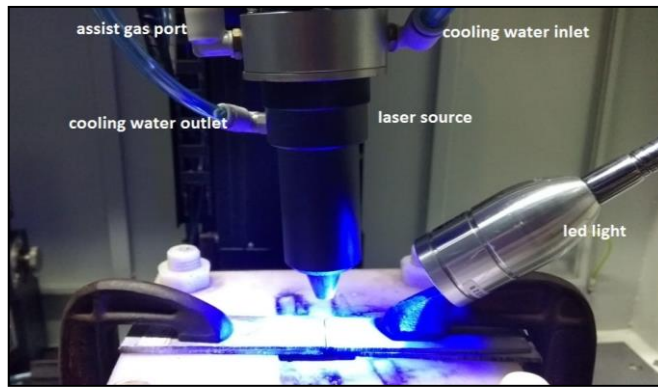


Figure 3.7 Butt welding set-up

3.3.6. Post-welding process

Post-welding processes are carried out per the guidelines in [133]. Once the welding process is complete, the samples are cut using a shearing machine employing its maximum load, as shown in **Figure 3.8**. Then the pieces are polished using different grades of sandpaper and velvet cloth in an automated polishing machine. Before measuring, the samples are etched using Keller's and Baker's reagent.

Different grades of sand papers and polishing time employed in the present work are:

SiC sandpapers of grades 100, 200, 400, 600. On each sandpaper, polishing was done for 3 mins in horizontal and vertical directions. 800, 1200, 1500, 200, and 2500 grades of sand papers are used, and on each paper, 2 mins of polishing only in the horizontal direction. The diamond paste is used to polish on an automatic polishing machine; after completing all these processes, a mirror finish polishing is obtained, which is necessary for microscopic and metallographic measurements.



Figure 3.8 Cutting of the component on the shearing machine

3.3.7. Description of the testing equipment

Optical microscope

The weld images and weld measurements are taken using an optical microscope with a 5x, 10x, 20x, and 50x zoom. Olympus software was used to collect data.

Scanning Electron Microscope (SEM) with EDS



Figure 3.9 Scanning electron microscope with EDX

The scanning electron microscope with EDX is shown in **Figure 3.9**, which can be operated in both high and low vacuum modes. The model is JOEL JSM IT1500. Its magnification ranges from 5X to 5X to 3,00,000X. The machine can accommodate a specimen of a maximum size of 200 mm. It has five axes which are fully motorized. It can be tilted between 10^0 to 90^0 and has 360^0 rotation. It has a magnification range between 5x to 3,00,000x. It has facilities for scanning control, image storage, auto bias and image processing and detection.

EDX machine is abbreviation of energy dispersive x-ray spectrometer. It has detection capacity from Be(4) to Am(95). It is useful in quantitative, qualitative analysis, mapping, line scan and has area analysis capabilities

3.4 Methodologies

3.4.1 Response Surface Methodology

A combination of statistical and mathematical methods known as Response Surface Methodology (RSM) can be used to create, enhance, and optimise processes. In 1951, George E. P. Box and K. B. Wilson introduced this technique. The field of response surface methodology includes an experimental method for examining the range of the process parameters, experimental and mathematical modelling to establish a suitable correlation between the output and the process parameters, and optimisation techniques for identifying the process parameter quantities that produce preferable values of the response.

Response surface methodology is one of the modelling and optimisation techniques currently popularly used to describe how welding operations function and identify the optimal responses of concern.

When all independent variables ($\xi_1, \xi_2, \xi_3, \dots, \xi_k$) are measured, controllable, and continuous in the investigations with minimal error, the response surface y can be defined as follows.

$$y = f(\xi_1, \xi_2, \xi_3, \dots, \xi_k) + \varepsilon \quad (3.1)$$

Where the form of the genuine response function f is unknown and perhaps quite complex, the term ε stands for additional causes of variability that f does not consider. In most circumstances, ε considers effects like measurement error on the response, ambient noise, and the influence of other parameters. ε is commonly seen as a statistical error. The anticipated response can therefore be expressed as follows:

$$E(y) = \eta = E[f(\xi_1, \xi_2, \xi_3, \dots, \xi_k)] + E(\varepsilon) = f(\xi_1, \xi_2, \xi_3, \dots, \xi_k) \quad (3.2)$$

$\xi_1, \xi_2, \xi_3, \dots, \xi_k$ in eq.(3.2) are called natural variables because they are expressed as measurements in units such as degrees Celsius or pounds per square inch. It is easy to change natural parameters to coded parameters in RSM work

$x_1, x_2, x_3, \dots, x_k$. These coded variables are typically described as having a mean zero and the same standard deviation and being dimensionless. So, the response function (Eq. 3.2) can be written as:

$$\eta = f(x_1, x_2, x_3, \dots, x_k) \quad (3.3)$$

Creating an approximate model for the genuine response surface is essential to use RSM in practical applications. The approximation model is an empirical model based on observed data from the process. A group of statistical methods known as multiple regressions can be used to create the several kinds of empirical models needed in RSM. The first-order model for the scenario of two independent variables, in respect of the coded variables, is:

$$\eta = \beta_0 + \beta_1 x_1 + \beta_2 x_2 \quad (3.4)$$

When there is an interaction between such coded variables, the following can be included in the model:

$$\eta = \beta_0 + \beta_1 x_1 + \beta_2 x_2 + \beta_{12} x_1 x_2 \quad (3.5)$$

This term is an interaction-based first-order model. The response function becomes curved when the interaction term is included. In these cases, a second-order model is necessary. The second-order model is the case with two variables:

$$\eta = \beta_0 + \beta_1 x_1 + \beta_2 x_2 + \beta_{11} x_1^2 + \beta_{22} x_2^2 + \beta_{12} x_1 x_2 \quad (3.6)$$

Generally, the first-order model is

$$\eta = \beta_0 + \beta_1 x_1 + \beta_2 x_2 + \dots + \beta_k x_k \quad (3.7)$$

RSM often use a second-order polynomial equation:

$$\eta = \beta_0 + \sum_{j=1}^k \beta_j x_j + \sum_{j=1}^k \beta_{jj} x_j^2 + \sum_{i < j} \sum_{j=2}^k \beta_{ij} x_i x_j \quad (3.8)$$

Where, $\beta_{i,j} = 0, 1, \dots, k$ are the regression coefficients.

3.4.2 Response surface experimental designs

RSM offers improved process optimisation, reproducibility, and a clear perspective for developing predictive models. Response surfaces in RSM are graphical representations that show how process variables interact with one another and how that interacts with the response. The two main factorial designs

used to evaluate the quadratic response surface and create second-order polynomial models in RSM are Central Composite Design (CCD) and Box-Behnken Design (BBD).

Central composite design

A CCD contains three design points: axial (star), centre, and two-level factorial or fractional. It was constructed using a 2^k factorial design point set and improved with many centre points and 2^k axial (star) points, as shown in Figure 3.10. Two design criteria must be specified: the distance of the axial runs from the design centre and the total number of centre points. A face-centred central composite design (CCD) with $\alpha = 1.0$ can alter the five levels of the standard main composite design for each factor. Each part of the face-centred design has only three layers. The 2^k factorial points were initially utilised to fit a first-order model, but this model failed to fit; hence, the axial model was developed, which permits the inclusion of quadratic terms.

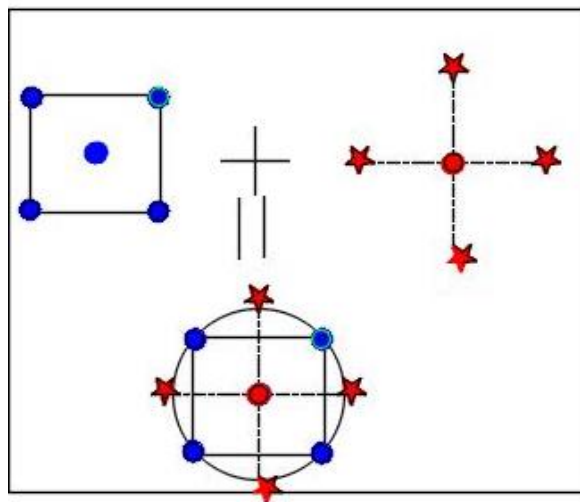


Figure 3.10 Central composite design points in design space

The number of experimental runs in the factorial section of the central composite design affects the value of α :

$$\alpha = [\textit{number of factorial runs}]^{\frac{1}{4}} = [2^k]^{\frac{1}{4}} \quad (3.9)$$

Box-Behnken design

Box-Behnken designs require fewer runs to produce higher-order response surfaces than a standard factorial approach. It combines a 2^k factorial design with an incomplete block design, with particular positioning of design points (**Figure 3.11**). Three levels are needed for each element in these designs. It produces a robust estimate in the design space's centre, where the optimum is thought to lie but is weaker towards the cube's edges, where there are no design points. The accuracy of the remaining runs becomes crucial to the model's reliability if experimenters miss any experiments. The more initial runs the central composite designs have, the more problem-resistant they are.

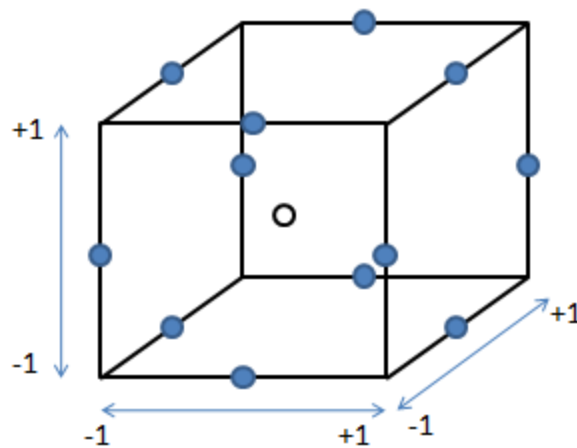


Figure 3.11 Box-Behnken design points in design space

3.4.3 Gaussian process regression

The Gaussian processes model is a frequently used probabilistic supervised machine learning methodology for classification and regression problems. A Gaussian processes regression (GPR) approach provides uncertainty metrics for predictions that involve previous information (kernels). The statistics and computer science groups created a supervised learning technique called the Gaussian processes approach.

Basic concepts of GPR

Gaussian process regression (GPR) is used to model the data-controlled technique used in this study. A Gaussian process (GP) is given as a mean

function and a covariance or kernel function. GP is a linear model of random variables which possess normal distribution. Hence, the mean function is considered zero or linear. Consider training a set y of n parameters having an input matrix $x \in R^n$ and the output is a variable where $y \in R$. The GP is represented as

$$y_* = GP(m(x)k(x, x')) \quad (3.10)$$

Here, the mean function is stated as $m(x)$, and the covariance is designated as $k(x, x')$.

The $m(x)$ in the GP is related to the expected value of the function at any input matrix point given as

$$m(x) = E[f(x)] \quad (3.11)$$

The $k(x, x')$ is the confidence level for the mean function and is given as

$$k(x, x') = E[(f(x) - m(x))(f(x') - m(x')))] \quad (3.12)$$

The covariance or kernel function helps control the function's smoothness and periodicity. GPR is performed using the Bayesian regression framework. This process is a non-parametric, Bayesian approach to regression that works well on small datasets and can provide uncertainty measurements on the predictions.

The response variable y is expressed as a function of p -dimensional variables in linear regression. $x = [x_1, \dots, x_p]^T$ parametrised by $w = [w_1, \dots, w_p]^T$:

$$y_i = \sum_{d=1}^p w_d x_{id} + \varepsilon_i \quad i = 1, \dots, n \quad (3.13)$$

Here n represents the number of data points, x_{id} is the d -th covariate of x_i and ε_i denotes the additive Gaussian noise with zero mean and unknown variance σ_ε^2 .

GPR with zero mean function and covariance as the squared exponential variant is given as

$$k(x, x') = \delta_f^2 \exp\left[-\frac{r}{2}\right] \quad (3.14)$$

Here r is given as $r = \frac{|x-x'|^2}{l^2}$. The hyper-parameters, noise (δ_f), and the length scale l impact the outcome of the GPR.

The various kernels that are used in GPR are given as follows:

1. Matern 5/2: $k(x, x') = \delta_f^2 \left(1 + \sqrt{5r} + \frac{5r}{3}\right) \exp[-\sqrt{5r}]$ (3.15)

2. Rational quadratic: $k(x, x') = \delta_f^2 \left(1 + \frac{1}{2\alpha l^2} (x - x') (x - x')^T\right)^{-\alpha}$ (3.16)

3. Exponential: $k(x, x') = \delta_f^2 \exp[-\sqrt{r}]$ (3.17)

The value of the predicted function (y_*), called Gaussian prior distribution, is obtained as $y_* | y \sim N(\bar{f}_* \text{cov}(f_*))$.

Here \bar{f}_* is the mean value of the prediction and yields a reasonable estimate for y_* . ($\text{cov}(f_*)$ gives uncertainty in the projection. The mean prediction value is a linear set of target y , while the uncertainty in the prediction varies according to the inputs.

$$\begin{pmatrix} y \\ f_* \end{pmatrix} \sim N \begin{pmatrix} m(X) \\ m(x_*) \end{pmatrix}, \begin{bmatrix} K(X, X) + \sigma_n^2 & K(X, X_*) \\ K(X, X) & K(X_*, X_*) \end{bmatrix} \quad (3.18)$$

Here, the matrix $K(X, X)$ is the covariance of the training data set and $K(X_*, X_*)$ is the matrix of training data which resembles the $N \times N_*$ covariance matrix attained from training and testing data. The marginal likelihood function for the f_* is given as

$$P(f_* | X, y, x_*) \sim N(\bar{f}_*, \text{cov}(f_*)) \quad (3.19)$$

Here,

$$\bar{f}_* = E(f_* | X, y, x_*) = mX_* + K(X_*, X)[K(X, X) + \sigma_n^2 I]^T [y - m(x)] \quad (3.20)$$

$$\text{cov}(y_*) = K(X_*, X_*)[K(X, X) + \sigma_n^2 I]^{-1} K(X, X_*) \quad (3.21)$$

Using the logarithmic identifier to simplify the expression, the log marginal likelihood is given as

$$\log P(y | X, \theta) = -\frac{1}{2} y^T (K(X, X) + \sigma_n^2 I)^{-1} y - \frac{1}{2} \log |K(X, X) + \sigma_n^2 I| - \frac{n}{2} \log 2\pi \quad (3.22)$$

Here, θ denotes the set of hyperparameters necessary for the covariance function under consideration. The minimum posterior hyperparameter represents the covariance function obtained by maximising or minimising the negative log marginal likelihood.

3.5 Particle swarm optimisation

3.5.1 Theory of optimisation

Optimisation is a way of getting the best result in a given environment. It can be defined as finding the conditions that yield any function's minimum or maximum value. Since no single method is available for solving all optimisation problems efficiently, numerous optimisation methods have been developed for solving various optimisation problems. Optimal searching methods are frequently referred to as mathematical programming. These mathematical techniques aid in determining the minimum of a function of numerous variables given a set of restrictions.

3.5.2 Classification of optimisation problems

There are different criteria for classifying an optimisation problem are described below:

Based on the existence of constraints

Depending on whether or not limitations exist in the issue, the optimisation problem can be classified as constrained or unconstrained.

Based on the nature of the design variables

Optimization tasks are classified into two major types based on the design variables involved. The first type of problem is a parameter or static optimisation problem, in which a set of design parameters is addressed to minimise some preset function of these parameters while adhering to certain constraints. The second type of problem is a trajectory or dynamic optimisation

problem, where the goal is to find a collection of design parameters that are all continuous functions of some other variables and minimise an objective function subject to a set of restrictions.

Based on the nature of the equations involved

Depending on the nature of expressions for the objective function and the constraints, optimisation problems can be classified as linear, non-linear, geometric and quadratic programming problems.

Based on the permissible values of the design variables

Optimisation problems can be classified as integer and real-valued programming problems.

Based on the deterministic nature of the variables

Optimization processes can be classed as deterministic or stochastic programming depending on the nature of the variables involved.

Based on the concept of 'function separability,'

Non-separable and separable programming problems are two types of optimization problems.

According to the number of objective functions

Optimisation problems are classed as single or multi-objective programming problems based on the number of objective functions to be minimised (MOPP). The current research focuses on multi-objective optimisation problems.

3.5.3 Multi-objective optimisation

Multi-objective optimisation problems contain many objectives that need to be handled simultaneously. They should be either maximised or minimised concurrently. The multi-criteria nature of these problems requires a redefinition of the optimality of a solution, often termed as Pareto optimality.

Trade-offs characterise multi-objective issues, as opposed to single-objective optimisation. So, many Pareto optimal solutions correspond to different settings of the considered multi-objective problem.

Let the search space $S \subset \mathbb{R}^n$ be an n -dimensional one, and $f_i(x), i = 1, 2, \dots, k$ be the k number of objective functions defined in S . Consider that f is a vector function defined as

$$f(x) = [f_1(x), f_2(x) \dots f_k(x)], \text{ and}$$

$g_i(x) \leq 0, i = 1, 2, \dots, m$ be m inequality constraints. Then, $x^* = (x_1^*, x_2^* \dots x_n^*)$ is a solution that minimises $f(x)$.

The objective functions $f_i(x)$ may be conflicting, making finding only one global minimum at the single point in S impossible. The optimality of a solution in multi-objective problems should be redescribed for this purpose.

Suppose, $u = (u_1, u_2 \dots u_k)$ and $v = (v_1, v_2 \dots v_k)$ are two vectors present in S . Then, u dominates v , if and only if $u_i \leq v_i$ for all $i=1, 2, \dots, k$, and for a minimum of one component. This quality is known as *Pareto dominance*.

A multi-objective problem solution, x , is said to be Pareto optimum if and only if there is no other solution, y , in S such that $f(y)$ dominates $f(x)$. In this situation, x is therefore said to be non-dominated for S .

The Pareto optimal set, generally represented as P^* , is the collection of all Pareto optimal solutions for a given problem. The set $\mathcal{PF}^* = \{f(x): x \in P^*\}$, is called the Pareto front.

A convex pareto front is the one, for all $u, v \in \mathcal{PF}^*$ and for all $\lambda \in (0, 1)$, there exists a $w \in \mathcal{PF}^*$ such that $\lambda \|u\| + (1-\lambda) \|v\| \geq \|w\|$, and the concave front exists only when $\lambda \|u\| + (1-\lambda) \|v\| \leq \|w\|$.

A Pareto front can also be concave, convex, or discontinuous. Most multi-objective optimisation techniques consider these scenarios to be the most difficult.

Because the detection of a single solution, which is adequate in the single-objective situation, is not valid in many circumstances, including competing target functions, the unique nature of multi-objective issues necessitates the development of new goals for the optimisation approach. Detecting all Pareto optimal solutions is the major goal in multi-objective optimisation issues, according to the notion of Pareto optimality. However, because the Pareto

optimal set can be infinite and our computations are constrained by time and space, the goals are adjusted to be more practical.

3.6 Approximate Methods for Solving Multi-objective

Problems

In many circumstances, Pareto curves may not be calculated efficiently. Even if finding all these points is feasible, they are frequently of exponential scale. So, these problems are usually solved using approximation methods. In general, many practical issues pose challenges for the decision-maker to have all of the facts correctly and completely formulated. In such cases, the decision maker is more likely to learn more as soon as preliminary solutions are provided. As a result, in such circumstances, having some approximation solutions can aid in determining whether a precise method is required and, on the other hand, utilising such a solution to improve the problem formulation. There are different situations where approximating methods can be used: representing the solution set when the objective function is numerically available; approximation of the solution set in case only a few but not the entire set of the Pareto curve is numerically available; reaching the solution set when the whole efficient set is not numerically available. Scalarization is one such approximation technique that optimises the considered objectives.

3.6.1 Scalarization method

Generally, multi-objective optimisation is carried out by weighing the objectives and combining them into a problem with a single objective. This process is called scalarisation and minimises a positively weighted convex sum of all objectives.

$$\sum_{j=1}^n r_j * f_j(x) \tag{3.23}$$

$$\sum_{j=1}^n r_j = 1 \tag{3.24}$$

$$r_j > 0; \quad j = 1, 2, \dots, n; \quad x \in A$$

This represents a new problem with a unique optimisation function denoted as $P_A(r)$. The obtained value is the minimised value of the original multi-objective problem. Its image belongs to the Pareto curve.

3.6.2 Nature-inspired metaheuristics

Generally, the traditional algorithms are deterministic, like the scalarisation method described in the earlier section is a part of linear programming which is deterministic. Some techniques like Newton-Raphson are gradient-based, utilising the function's derivatives, including the function itself. But the main drawback is that it requires continuous data. But if there is any discontinuity in the data, gradient-free methods like the Nelder-Mead downhill algorithm are preferred. Stochastic algorithms come to use when there is randomness or probability in the data. These are again classified as metaheuristic and heuristic algorithms. Heuristic algorithms work on a trial and error, wherein obtaining the optimal solution is not always assured. Local search and randomisation of the particles are the two methods in metaheuristic optimisation. Since randomness provides search on a global scale, they are also called global optimisation techniques. The essential components of these algorithms are exploitation and diversification. The search space is exploited to obtain a diverse solution on a global scale. The local search space is also used to get the best solution, termed the global best. Randomness is introduced in the search to avoid being trapped in the local optimum solution. Metaheuristics help in convergence to the optimal solution at the earliest. Metaheuristics are again divided into population-based algorithms and trajectory-based algorithms. Genetic algorithm, Particle swarm optimisation, and firefly algorithm come under population-based algorithms. Trajectory-based algorithms utilise a single particle which moves along the search space in a piecewise manner. Simulated annealing falls under this category.

3.6.3 Theory of particle swarm optimisation

Particle swarm optimisation is a stochastic, iterative search algorithm which is modelled on the social behaviour of birds and flocks. Kennedy and Eberhart first introduced the PSO algorithm in 1995. It is based on the natural process of group communication of sharing individual knowledge when a group of birds search for food or migrate in a search space. Since the PSO algorithm is learned from

animal activity or behaviour to solve optimisation problems, it is dealt with under swarm intelligence techniques of metaheuristics [134].

Swarm intelligence is a class of algorithms replicating natural and artificial processes of individuals collaborating among themselves through decentralised control and self-organization. The algorithm focuses on group behaviour that emerges from members' local interactions with one another and the ecosystem in which they live. Ant and termite colonies, fish schools, bird flocks, and animal herds are all prominent instances of swarm intelligence systems [135].

An ideal swarm intelligence system has the following properties [136]:

- It is comprised of many individuals.
- The swarm are reasonably cognate.
- The individuals interact by exchanging local information directly or via the environment.
- The local interactions of the individuals among themselves and the environment defines the system's global behaviour.

Swarm intelligence has already been used in many fields since its introduction. Swarm intelligence research and applications primarily focus on ant clustering conduct, wasp and termite nest-building behaviour, flocking and schooling in birds and fish, ant colony optimisation, particle swarm optimisation, swarm-based network management, and cooperative behaviour in robot swarms.

The main rules employed in PSO match the velocity and acceleration of the nearest neighbour distance for a collective search of food as suggested by [136] through their experimental analysis simulated this behaviour. **Figure 3.12** shows the early variations proposed to the original PSO.

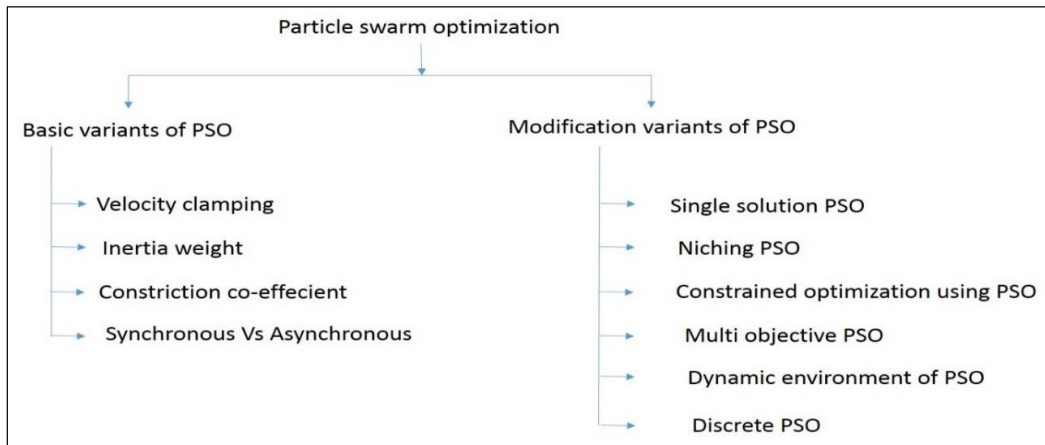


Figure 3.12 Early variants of PSO. Image courtesy: [134]

The mathematical framework of PSO

- Let the space where the swarm searches be denoted as $A \subset \mathbb{R}$
- $f: A \rightarrow Y \subseteq \mathbb{R}$, is the objective function.
- Assume that A is also the feasible space of the problem under consideration. Hence, no other constraints are imposed on the solution exclusively.
- Since the current algorithm is population-based that utilizes a population of possible solutions to analyse the search space concurrently, the population are called a swarm, and its individuals are denoted as particles.

Consider that $S = \{x_1, x_2 \dots x_N\}$ indicates the swarm with N number of particles (candidate solutions), defined as: $x_i = (x_{i1}, x_{i2} \dots x_{in})^T \in A, i = 1, 2 \dots N$. The particles are randomly given the indices. N is a parameter that is defined by the operator.

Let the objective function $f(x)$ relate to all the data in A . So, each particle has a specific value of the function. $f_i = f(x_i) \in Y$.

It is considered that the particles fly inside the search space, A , iteratively. The movement in the search space is enabled by altering the position of particles with the help of an appropriate position shift attained by the velocity component. Velocity is represented as: $v_i = (v_{i1}, v_{i2} \dots v_{in})^T, i = 1, 2 \dots$

N . The Velocity is also adjusted iteratively to enable the possibility of visitation of any region in space A for the particles. When t the iteration counter, the present position of the i^{th} particle and its velocity are represented as $x_i(t)$ and $v_i(t)$, correspondingly. Velocity is revised with the data obtained in previous steps of the algorithm. For this purpose, the swarm maintains a memory where it stores the information about the best position a particle has ever visited during its search. The memory set maintained by PSO is given by $P = \{P_1, P_2 \dots P_N\}$. The memory set P maintains the information about the best positions visited, which is given by $p_i = \{p_{i1}, p_{i2} \dots p_{in}\}^T \in A, i = 1, 2 \dots N$. These positions are defined as $p_i(t) = \text{argmin} f_i(t)$. Here ' t ' implies the iteration counter.

Since the PSO algorithm depends on the simulation of the social behaviour of birds, information is exchanged as a part of communication. This exchanged information leads the solution towards approximate global maximisation. Let g be the index of the best position with the lowest function value in P at a given iteration t , i.e., these positions are defined as $p_g(t) = \text{argmin} f(p_i(t))$

Then, PSO is defined by the following equations

$$v_{ij}(t + 1) = v_{ij}(t) + C_1 R_1 (P_{ij}(t) - x_{ij}(t)) + C_2 R_2 (p_{gj}(t) - x_{ij}(t)) \quad (3.24)$$

$$x_{ij}(t + 1) = x_{ij}(t) + v_{ij}(t + 1), \quad (3.25)$$

where $i = 1, 2, \dots, N$; $j = 1, 2, \dots, n$, where t denotes the iteration counter; R_1 and R_2 are random variables uniformly distributed within $[0,1]$; and C_1 and C_2 , are weighting factors. They are also called cognitive and social parameters, respectively.

From Eq. 3.24, it is evident that the revision of the velocity of each particle consists of three components:

They are:

1. The previous velocity, $v_{ij}(t)$, is known as the 'inertia part'. It imparts the required momentum for the particles to roam in the space to be exploited.
2. The 'cognition' part, $C_1 R_1 (P_{ij}(t) - x_{ij}(t))$, represents the particle's own experience
3. The 'social' part, $C_2 R_2 (p_{gj}(t) - x_{ij}(t))$, reflects the information shared among all the particles.

Explanation of the terms in the eq. 3.[134]

- The previous velocity term: Situated on the right-hand side of equation (3.3), this term provides a kind of inertial movement to the particle by considering its last position shift. This property guides the global best, x_g , particle, preventing it from getting entrapped in local minima if sub-optimal information is stored.
- Suppose a particle, x_i , finds a new position with a minimum function value compared to the existing best position, then it is considered the global best (i.e., $g \leftarrow i$), and its best position, p_i , coincides with p_g and x_i in the subsequent iteration. In that case, the two stochastic terms in eq. (3.3) vanishes if no previous velocity term exists in eq. (3.3), the particle stays at the same position for several iterations till another particle detects a new best position. In contrast, the velocity term enables this particle to continue its search after its previous location shift. The particle velocity is determined by its personal and global best positions when there is no inertia part.
- When the social and cognition terms $C_1 = C_2 = 0$ indicate that there are no 'cognition' and 'social' components in the updated velocity. The particle flies in a linear direction until it reaches the search space's boundary. There can be no ideal solution unless the solution is on its way.
- When $C_1 = 0$, the system lacks 'cognition' part in eq. 3.24. The updated velocity equation is considered to be in 'social-only' model. The PSO algorithm can reach a new search space with the interaction among particles. The particle swarm, on the other hand, converges at a reasonably fast rate. For complex issues, the algorithm is easily caught in local optima, however it performs better in solving particular specialised problems.
- When $C_2 = 0$, 'social part' will not be there in the updated velocity. This condition indicates that there is no sharing of the information among the particles. The PSO algorithm is said to be in 'cognition-only' model. Also, choosing $C_1 > C_2$ would bias the result towards local convergence, while in the opposite case, $C_1 < C_2$, sampling towards the direction of global convergence.

The operation of PSO given in pseudocode

Input: Number of particles, N ; swarm, S ; best positions, P .

Step 1. Set $t \leftarrow 0$.

Step 2. Initialise S and Set $P \equiv S$.

Step 3. Evaluate S and P , and define index g of the best position.

Step 4. While (termination criterion not met)

Step 5. Update S using *Eqs.* (3.24) and (3.25).

Step 6. Evaluate S .

Step 7. Update P and redefine index g .

Step 8. Set $t \leftarrow t+1$.

Step 9. End While

Step 10. Print best position found

3.6.4 Multi-objective particle swarm optimisation (MOPSO)

The solution set of multi-objective optimisation aims to find a collection of different solutions called the Pareto optimal front. Generally, three goals should be achieved in the case of multi-objective optimisation:

1. Increase the number of members in the Pareto optimum set.
2. Reduce the distance between the Pareto front generated by the technique and the real (global) Pareto front.
3. Increase the spread of solutions identified so that the vector distribution is homogeneous and smooth.

There are three main issues to be considered when employing PSO to multi-objective optimisation [137]:

1. In what ways do chosen particles (to be utilised as leaders) select non-dominated solutions over dominated solutions?
2. How to keep the non-dominated solutions discovered during the search process in order to present non-dominated solutions for all populations including the present and the previous one, along the well-spread Pareto front?

3. How can the swarm preserve diversity while avoiding convergence to a single solution?

Several studies have been carried out in MOPSO to augment its usage for diverse problems.

The classification of current MOPSOs as mentioned in [137] are sub-population techniques, aggregating methods, lexicographic ordering method, pareto based strategies and others methods by combining the available techniques.

3.6.5 Current status of PSO

- PSO is used to optimise the complicated multi-dimensional non-linear functions.
- PSO outperforms other recognised global optimisation techniques in terms of performance.
- It is possible to use it directly if the specified parameter settings are used.

Among others, applications for and in:

- ✓ Neural Networks training
- ✓ Video analysis applications
- ✓ Design optimisation applications

3.6.6 Status of PSO mechanical engineering field

Many mechanical engineering optimisation applications give PSO new dimensions and hybridisation, with the following works mentioned as an example. A novel algorithm for dynamic task scheduling was proposed using the concepts of particle swarm optimisation [138]. An extension of the particle swarm optimisation (PSO) algorithm, which conforms to actual nature, is introduced to solve combinatorial optimisation problems [139]. The development of this algorithm is essentially based on the balanced fuzzy sets theory. The balanced fuzzy particle swarm optimisation algorithm is used for the fundamental optimisation problem entitled the travelling salesman problem (TSP). The method was used for TSP problems and convergence inspecting the new algorithm. A study was conducted on applying an improved PSO algorithm in hydraulic press system identification by changing the inertia weight [140].

3.7 Summary

The material adopted in this present work is aluminium alloy 2024. This material is welded on an Nd: YAG laser welding machine with a typical wavelength of 1064nm. The pre-welding and post-welding operations related to the welding process and the set-up employed in the welding operation are explained. The theories related to the design of experiments: response surface methodology, Gaussian process regression and particle optimisation are discussed.

Chapter 4: Finite element modeling of heat transfer and weld pool dynamics

4.1 Introduction

The development of a transient 3-D thermo-fluid model to mimic heat transport and weld pool dynamics during deep penetration laser welding of the aluminium alloy AA2024 is described. This investigation of the influence of driving forces on the dynamics and geometry of melt pools is carried out using numerical modelling and non-dimensional analysis techniques. The impact of temperature-driven surface tension on weld pool shape is investigated by altering the input parameters. The normalised dimensions of the weld pool are plotted against dimensionless quantities, such as the Peclet, Reynolds, and Marangoni numbers, to understand the process's uncertainty and variations. The melt flow in the weld pool is laminar for the material and process parameters evaluated in this study. The findings reached in this study potentially help to explain Marangoni convection in materials with a negative gradient of surface tension, as well as give insight into the formation of defects and their elimination during laser welding of aluminium alloys. The constructed model is tested against experimental data, and it is found to be in excellent agreement.

4.2 Objectives

The objectives of the present study are:

1. Developing a numerical model in COMSOL Multiphysics' Computational Fluid Dynamics (CFD) module for simulating the flow field and heat transfer in aluminium alloy weld pools exposed to a laser heat source during continuous mode laser welding.
2. To answer the following questions: (a) How do input factors such as scanning speed and peak power impact the temperature profiles and flow pattern in the melt pool at different times? (b) How do the melting pool's temperature profile and flow pattern change over time? (c) How does the

weld width, penetration depth, and melt pool volume vary in response to the input parameters?

3. To investigate the physics of the molten pool flow using the numerical model that has been constructed. In particular, what is the effect of Marangoni-driven flow in the weld pool on the form of the final fusion zone? (b) How does fluid velocity in the weld pool rely on the amount of heat given to the weld and the traverse speed of the laser beam? Moreover, (c) What is the relationship between the dimensionless melt pool and dimensionless numbers considering the uncertainty in the process?

4.3 Physical models

This work presents a numerical model constructed to simulate a transient 3-dimensional thermo-fluid model, consisting of two phases: solid and liquid. The liquid gas interface is considered non-deformable in this technique and oriented with the border of the computational domain in this approach. Further, this method deals with the melting front by linking the energy equation with the proportion of liquid in the respective equations. Subsequently, conservation equations are solved on a fixed mesh structure to capture the melting front at the surface of the weld pool. Many studies demonstrate that this model has been extensively used in the weld pool flow-modelling domain for a long time.

[141] examined the influence of Marangoni convection and Peclet number on the weld pool dynamics during laser spot welding of stainless steel. They revealed that convection dominates the weld pool dynamics after the system reaches a steady state. Using computer simulation, [142] has created a three-dimensional transient model for studying the weld bead profile in laser welding. The variations in the weld bead profile that occur due to the varied welding process parameters and fluid dynamics are investigated. Numerical simulation is used to investigate the influence of process parameters on the formation of an hourglass-shaped melt pool when laser welding is performed on stainless steel [143]. A thorough understanding of the driving mechanisms in the molten pool is necessary to study the influence of input parameters on different processes

connected to the weld pool. Several scientific investigations have been conducted to investigate the influence of temperature history and surface tension-driven fluid flow on the dynamics of the melt pool [141 - 143]. Keyhole behaviour and root hump creation in full penetration laser welding of aluminium alloy were attributed to the alloy's keyhole behaviour [144]. Techniques of the volume of fluid and ray tracing methods are employed to follow the free surface deformations in the molten pool. The coalescence of bubbles and the efficiency with which they coalesce are investigated to understand porosity creation better. The driving forces and mechanisms are studied by [145] to understand better the surface tension-driven flow and solidification behaviour in stainless steel parts. The surface tension-driven flow is analysed, and metallurgical properties are investigated to comprehend the flow's solidification morphology.

Finite element simulations are employed to investigate weld bead characteristics, thermal history, flaws, and keyhole instabilities, among other things. It is possible to better understand the weld pool dynamics by modelling heat transmission and fluid movement in keyholes [28, 144, 148]. [149] examine the simulation of molten pool dynamics by taking into account the Marangoni convection, recoil pressure, and buoyancy force, among other things. The geometry of a weld fusion zone is predicted using a constructed single-phase model. Using a three-dimensional heat and fluid flow model, Courtois et al. [47,48,49] were able to predict the evolution of melt pool morphologies. The level-set approach is used to represent the interface between liquid and vapour. The laser is considered a waveform, and the answer is obtained by solving the Maxwell equations for the laser. The geometry and proportions of the fusion zone are described in detail, utilising various approaches and methods. Nevertheless, in simulations, the effect of factors such as Marangoni convection, buoyancy, or gravity, as well as their influence on fluid flow, which are all part of the complicated melt pool phenomena, is not thoroughly investigated.

Many forms of melt flow, such as Marangoni flow generated by surface tension gradients, build-up of downward flow at the keyhole wall, and internal eddies, can be observed in the weld pool.

4.4 Solid-liquid model governing equations

This study aims to create a transient thermo-fluid model to comprehend the thermal properties and fluid dynamics of AA2024 during laser welding. Simulation is performed with a power varied from 2.5 kW to 5 kW and scanning speed in the range of 10mm/s to 30mm/s. The laser beam has a width of 0.36mm. The workpiece is 37.5 mm long and 20 mm wide with a thickness of 2mm. The beam is defocused at zero. Welding involves a complicated multi-physical process that involves fluid movement, heat transfer, mass transfer, and phase interaction. Numerous simplifications have been made to the simulation model to run the model.

The following assumptions are made:

1. The substance of the workpiece is homogenous and isotropic.
2. The distribution of laser intensity is considered to be Gaussian.
3. Conduction and convection are used to move heat within the workpiece. Radiation occurs between the component's surface and the surrounding air.
4. The shielding gas's effects are overlooked, and
5. Continuous laser mode is used throughout the procedure.

The laser beam is modelled as a heat flux flowing down the plate's y-axis in short intervals. As a result, the thermal history is investigated in terms of time and location. The beam travel time is calculated by considering the plate width and scanning speed. The time increment is proportional to the overall travel time and the load step count.

4.4.1 Model of a laser heat source

Pavelic et al. [18] were the first to propose that the heat source should be spread and presented a Gaussian distribution of flux deposited on the surface of the workpiece. According to [148], the laser heat source has an axisymmetric distribution with a Gaussian distribution:

$$Q_0 = \frac{3AP}{\pi r_b^2 h} \exp \frac{-3(x-x_c)^2}{r_b^2} \exp \frac{-3(y-y_c)^2}{r_b^2} \exp \frac{-3(z-z_c)^2}{h^2} \quad (4.1)$$

Where A denotes the absorption coefficient, P denotes the laser power in watts, r b denotes the laser beam radius in meters, and h is the height of the volumetric heat source in metres (equal to the plate thickness). The words x-x_c, y-y_c, and z-z_c refer to the radial distance between the corresponding coordinates and the beam centre.

4.4.2 Theoretical equations

The mass, momentum, and energy equations regulate the simulation [17]. The conservation of mass is primarily regarded during phase transitions, such as evaporation and solidification. The momentum equation considers the loss of momentum during metal solidification and the buoyancy caused by the temperature difference in the molten pool. Specifically, the energy term considers the laser heat source and energy losses caused by different heat transfer mechanisms in the melt pool.

$$\text{The mass conservation equation is } \nabla \cdot (\rho \mathbf{u}) = 0 \quad (4.2)$$

where ρ is the molten metal's density, and \mathbf{u} is the velocity vector.

The following is the equation for momentum conservation:

$$\rho \frac{\delta \mathbf{u}}{\delta t} + \rho (\mathbf{u} \cdot \nabla) \mathbf{u} = \nabla \cdot \left[-p \mathbf{I} + \mu (\nabla \mathbf{u} + (\nabla \mathbf{u})^T) - \frac{2}{3} \mathbf{u} (\nabla \cdot \mathbf{u}) \mathbf{I} \right] + K \mathbf{u} \quad (4.3)$$

M is the fluid's viscosity, and p is the fluid's pressure. K is the drag coefficient in the mushy area, which is calculated as follows:

$$K = \frac{C_1(1-f_l)^2}{f_l^2 + C_2} (\mathbf{u} - \mathbf{u}_{weld}) \quad (4.4)$$

C_1 is the constant operator denoting the mushy region circumstances. f_l is the liquid fraction or Darcy's damping specified for frictional dissipation in the mushy zone, and C_2 denotes a positive value to prevent division by zero. The mushy zone between solidus and liquidus is represented using the energy-temperature equation [12]. It is defined as follows:

$$f_l = \begin{cases} 0 & 0 < T < T_s \\ \frac{T-T_s}{T_s-T_l} & T_s \leq T \leq T_l \\ 1 & T \geq T_l \end{cases} \quad (4.5)$$

f_l is defined as the liquid fraction or Darcy's damping for frictional dissipation in the mushy zone. It varies between 0 and 1 when the temperature changes from solidus to liquidus. $f_l=0$ in the solid phase and 1 in the liquid phase. The solidus (T_s) and liquidus (T_l) temperatures of the target material are assumed to be 847 K and 933 K, respectively.

The conservation of energy is mathematically expressed as follows:

$$\rho C_p^* u \cdot \nabla T = \nabla \cdot (\lambda \nabla T) \quad (4.6)$$

During the welding process, the temperature in the fusion zone surpasses the material's melting point. As a result, phase change phenomena are incorporated in finite element simulations through the enthalpy technique [17].

$$C_p^* = C_p + \frac{\exp\left(\frac{(T-T_{melt})^2}{\delta T}\right)}{\sqrt{\pi} \delta T} H_f \quad (4.7)$$

where H_f denotes the latent heat of fusion and T denotes the mushy zone's temperature range. C_p denotes the specific heat capacity, whereas C_p^* is the apparent specific heat characterising the melting phase. The Reynolds-Averaged Navier-Stokes (RANS) equations for momentum conservation and the continuity equation for mass conservation are used to solve the simulation.

4.4.3 Driving forces

Within the melt pool, the major driving factors are surface tension, Marangoni convection, buoyancy, and gravity. Surface tension variation can be caused by temperature or composition/concentration factors, resulting in a considerable spatial variation in surface tension that shows Marangoni stresses at free surfaces. This Marangoni-driven flow can significantly affect the ultimate geometry of the weld. On the top and bottom surfaces of the plate, Marangoni convection is used to model the fluid flow caused by temperature-dependent surface tension [Eq. 8]. Surface tension is assumed to be linearly related to temperature [Eq. 9] indicating the presence of Marangoni convection.

$$d\sigma = \frac{\partial\delta}{\partial T} dT + \frac{\partial\delta}{\partial C} dC \quad (4.8)$$

$$\gamma = \gamma_m + \left(\frac{\partial\delta}{\partial T}\right) (T - T_m) \quad (4.9)$$

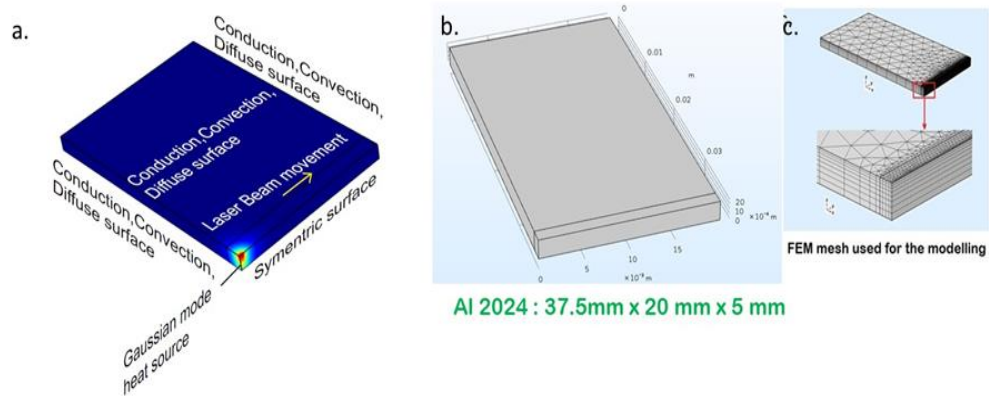
Where T and C denote temperature and concentration, σ denotes the surface tension at the melting point T_m [K], $(\partial\delta/\partial T)$ is the thermal coefficient of surface tension, T denotes the ambient temperature and Stefan Boltzmann constant $5.6703 \times 10^{-8} \text{ W/m}^2\text{K}^4$.

The workpiece's top surface is exposed to ambient conditions, while the workpiece's top and bottom surfaces are treated with slip. Due to the fixture's placement, the bottom surface is not exposed to ambient conditions. Each of the three sides (except the symmetrical one) is given a no-slip condition.

4.4.4 Meshing

Figure 4.1 illustrates the developed thermo-fluid model schematically. Free triangular and sweeping meshes are used to mesh the component. A highly refined mesh pattern is placed along the laser beam's scanning path to improve the results, as seen in **Figure 4.1**. (c). The remainder of the workpiece is meshed with coarser components to reduce computing time and memory requirements. Increased element count had no discernible effect on the result but increased computing time. As a result, a geometric model consisting of 15,984 mesh pieces is used and maintained throughout the simulation.

Boundary conditions



Mechanism of heat transfer in fluids

- Conduction
- Convection
- Radiation

Forces acting on the workpiece

- Surface tension
- Buoyancy force
- Gravity

Figure 4.1 Pictorial representation of the thermo-fluid model (a) Boundary conditions used in the simulation. (b) dimensions of the workpiece. (c) Mesh used for the modeling.

4.5 Validation of the developed numerical simulation

Experimental data published by [34] is used to validate the weld pool dimensions calculated from the simulation. The steel used in the experiment is AISI 304, high-quality stainless steel. The inputs are the power of the laser beam, the scanning speed, and the angle of the laser beam. It is the weld width and depth of penetration that are measured as output variables. The plate used in the experiments is 60 mm x 20 mm x 1.6 mm in size, with the dimensions 60 mm x 20 mm x 1.6 mm. All of the experiments are performed with the help of a continuous wave Nd: YAG laser system. The beam is angled at three different orientations from the workpiece in the experiment: 85° , 90° , and 95° .

On the other hand, the simulation is only performed for the beam angle of 90° degrees. Because the produced model is parametrically constructed, it is possible to vary the material qualities and process parameters while maintaining the model's physics. Several experimental circumstances developed by Balasubramanian et al. [34] are given to the model to verify it. These conditions

include material and process characteristics. The simulated results are then compared to the experimental data to determine whether the model is valid.

Figure 4.2 depicts the results of a simulation of the weld pool dimensions. The depth of penetration (DOP) and weld width (WW) of the weld pool is represented in **Table 4.1**. It is discovered that the findings obtained from the constructed simulation are pretty close to those obtained from previously published experimental data.

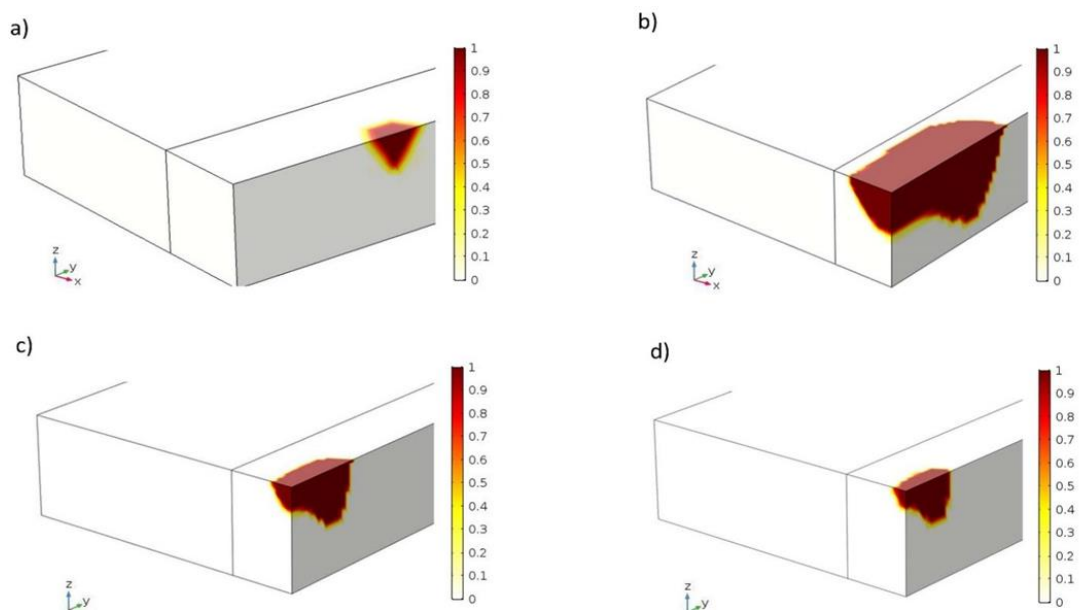


Figure 4.2 Simulated weld pool dimensions for (a) P= 750W, S= 750mm/min, $\alpha=90^\circ$, (b) P= 1250W, S= 750mm/min, $\alpha=90^\circ$, (c) P= 1250W, S= 1250 mm / min, $\alpha=90^\circ$, (d) P= 1000W, S= 1000mm, $\alpha=90^\circ$, (material. AISI 304, beam location $y = 10$ mm).

Table 4.1 Validation of weld pool dimensions

Sl. No	Laser power [W]	Welding speed S [mm/min]	Beam angle α [Degrees]	Experimental results		Simulation results		Percentage Error	
				DOP [mm]	WW [mm]	DOP [mm]	WW [mm]	DOP [%]	WW [%]
1	750	750	90	0.53	0.97	0.54	0.96	1.89	1.03
2	1250	750	90	1.48	1.26	1.46	1.30	1.35	3.17
3	1250	1250	90	0.71	1.14	0.75	1.16	5.63	1.75
4	1000	1000	90	0.68	1.05	0.71	1.00	4.41	4.76

4.6 Results and discussion

The following section discusses the results obtained by simulating the developed numerical model.

4.6.1 Temperature distribution and fluid flow inside the molten pool

The molten pool's temperature, fluid flow, and development through time at various time intervals (time steps) are depicted in **Figure 4.3**. The process parameters employed included a laser with a power of 5kW working at a scanning speed of 10 mm/s and a scanning time of 10 seconds. On the other hand, it has been found that the penetration depth expanded with time and reached complete penetration at around 0.355 seconds. The process reaches a maximum temperature of 2075.3 K at its peak, which is achieved directly below the point of incidence of the laser beam. The geometry of the molten pool impacts the fluid flow and the outer weld contour. The current simulation shows that the molten pool eventually expands wider and takes on the shape of an hourglass due to the shift in heat transmission mode from conduction at the beginning to convection at the end of the simulation. The peak temperature continues to rise until the heating process is completed. This increase in temperature may be seen in **Figure 4.3** (a-j), which depicts the distance between the starting point of welding and the end point of welding. Because aluminium

alloys have a higher thermal conductivity than other metals, the component becomes heated as it absorbs heat from the laser beam. Due to this, there is an increasing molten pool in the shape of an hourglass. A representation of the fluid flow field is also presented in **Figure 4.3**. As shown in **Figure.4.3**, w denotes the molten region on the plate, d represents the depth of the molten section, and Δd indicates the unmolten portion of the component. Fluid travels radially outwards, and the fluid flow field corresponding to the melt zone is shown in **Figure 4.4**.

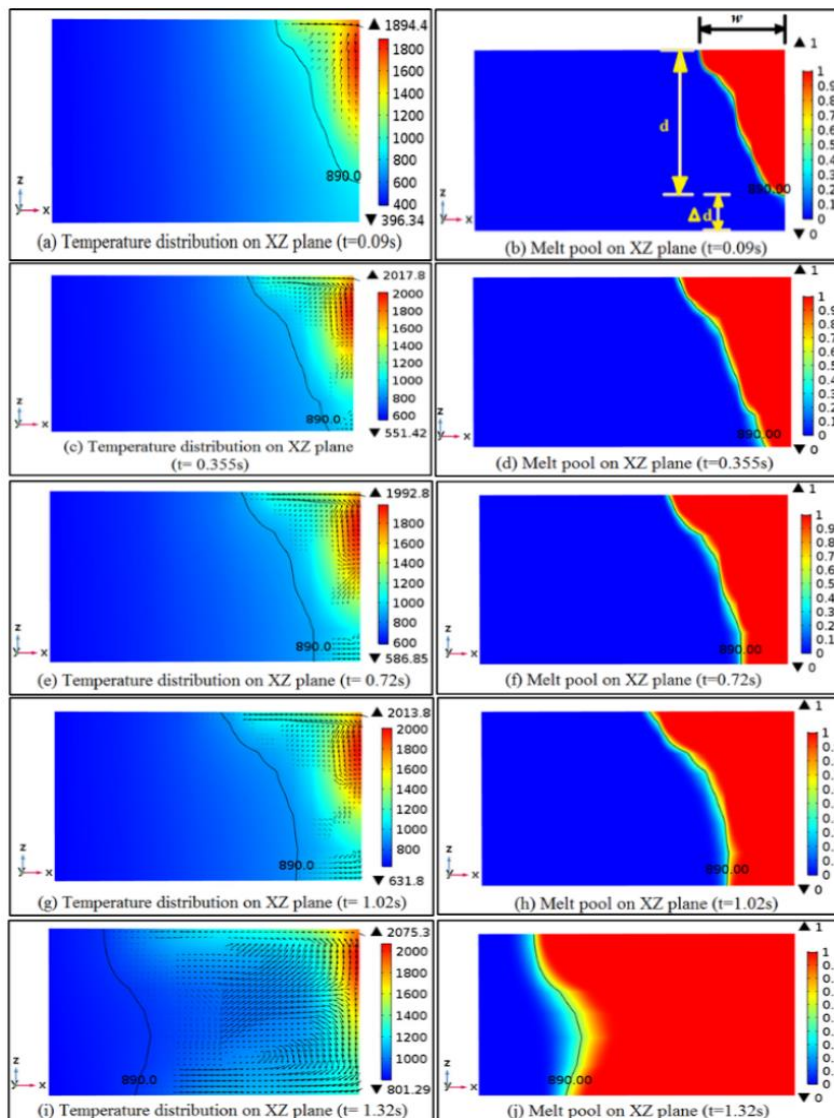


Figure 4.3 Temperature (K) distributions with fluid flow fields and melt pool evolution at different time instances along the scanning line on the X-Z plane at (a, b) $y = 1$ mm, (c, d) $y = 5$ mm, (e, f) $y = 10$ mm, (g, h) $y = 15$ mm, and (i, j) $y = 19.5$ mm.

4.6.2 Evaluation of weld width and depth of penetration

Figure 4.4 shows the variation in weld width with laser power and scanning speed. The laser power and scanning speed are varied between 2.5 – 5 kW and 10 – 30 mm/s, respectively, while keeping the beam spot radius at a constant value of 0.36 mm.

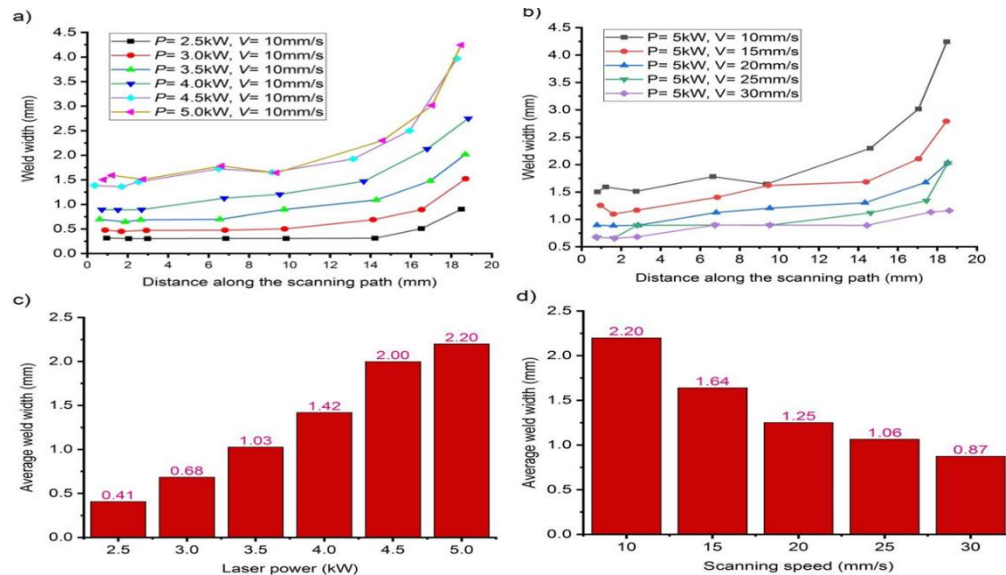


Figure 4.4 Variation of weld width along the scanning path with (a) laser power, (b) scanning speed, and variation of average weld width with (c) laser power, (d) scanning speed when all other parameters remain constant.

Effect of laser power on weld width: While keeping the scanning speed constant and varying the power in small increments from 2.5-5 kW, an increment in weld width is seen, as illustrated in **Figure.4.4 (a)**. The bar diagrams demonstrate that increasing the laser power from 2.5 kW to 5 kW increased the average weld width from 0.41 mm to 2.20 mm. This increase is due to a more significant rate of accessible input energy to the workpiece, which increases weld width when power is increased.

Effect of scanning speed on the weld width: When it comes to weld width, scanning speed impacts it. By increasing the scanning speed, the plots presented in **Figure.4.4(b)** are drawn to indicate the fluctuation in weld width. As the scanning speed is increased, it is seen that the weld width shrinks proportionally.

Increased input energy to the material allows wider weld widths to be produced at lower scanning speeds, resulting in broader weld widths. As shown in **Figure 4.4**, increasing the welding speed from 10 mm/s to 30 mm/s reduces weld width from 2.20 mm to 0.87 mm, as seen in **Figure 4.4. (d)**.

Effect of laser power on the welding depth: According to the data displayed in **Figure 4.5 (a)**, the penetration depth rises as the laser's strength increases. This rise in depth is consistent with previous observations. The maximum penetration depth into the material is not obtained with the 2.5 kW laser power employed in this investigation, even at the lowest level of scanning speed utilised in this study and within the dimensions of the workpiece taken into consideration. When a fixed power level is used, it can be observed that the depth of penetration grows gradually when the scanning distance is increased.

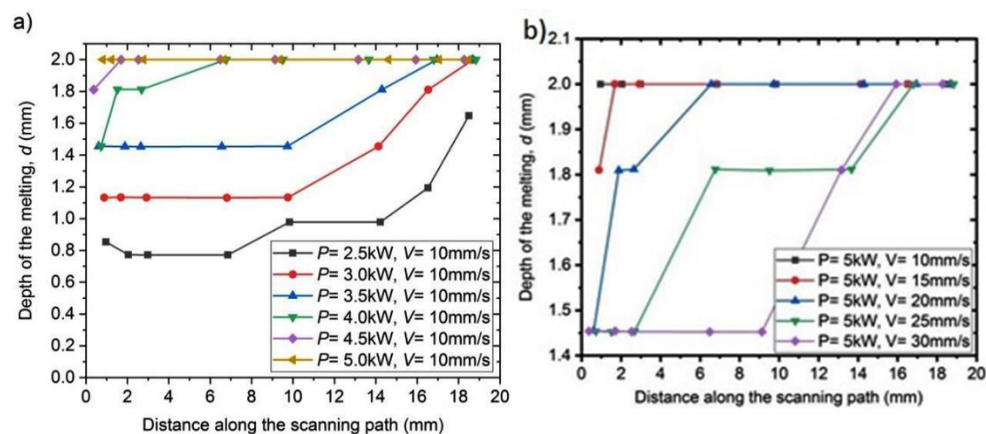


Figure 4.5 Variation of the depth of penetration with (a) laser power and (b) scanning speed when all other parameters remain constant.

After a certain amount of time, complete penetration is achieved when laser energies of 4 kW or 4.5 kW are applied. The depth of penetration is directly proportional to the density of laser energy. The penetration depth grows linearly as the power density of the system increases. However, it takes time before it can pass through the barrier and become stable. The total penetration point is reached after the beam has gone a specific distance along the scanning line when the input power is 4 kW.

Effect of scanning speed on welding depth: **Figure 4.5(b)**, the depth of penetration decreases as the scanning speed increases. Welding speed is an

essential element since it influences the grain size and cooling rate, as well as the breadth and depth of the weld. Because of the longer irradiation duration and higher energy input to the workpiece, a lower scanning speed resulted in complete penetration in a shorter amount of time.

Prediction of the volume of the weld pool

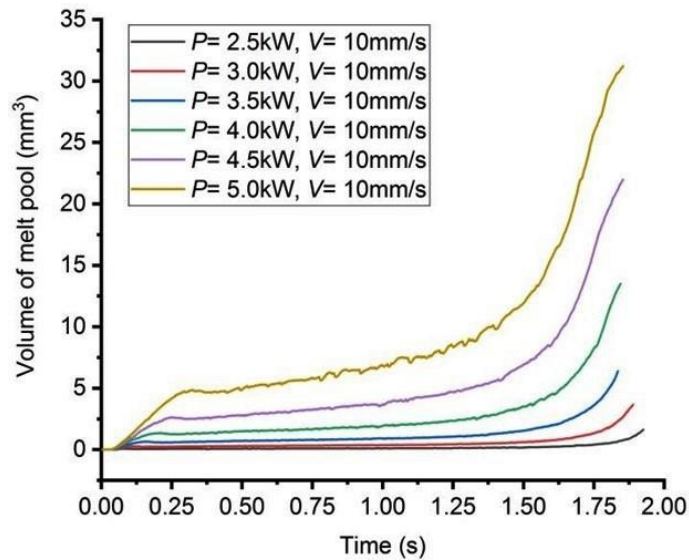


Figure 4.6 Variation of the melt pool volume with power.

It is shown in **Figure 4.6** that the influence of laser power on the melt pool volume is more significant at higher levels of laser power, which is due to the larger laser fluence as the laser power increases. The melt pool volume is at its highest for the maximum power level, i.e., 5 kW, with a significant increase in the first transition time of roughly 0.25s. The melt pool volume is at its minimum for the lowest power level, i.e., 1 kW. With increasing amounts of power, more heat is provided to the material, resulting in a larger volume of the melting pool. Until the beam reaches the end of the plate, the application of the smallest amount of power, 2.5 kW, does not result in a large melt pool. As the beam approaches the end of the welding plate, the whole amount of heat gets collected there. Hence, for all power levels tested in this study, melt pool volume increases as the beam progresses toward the end of the plate.

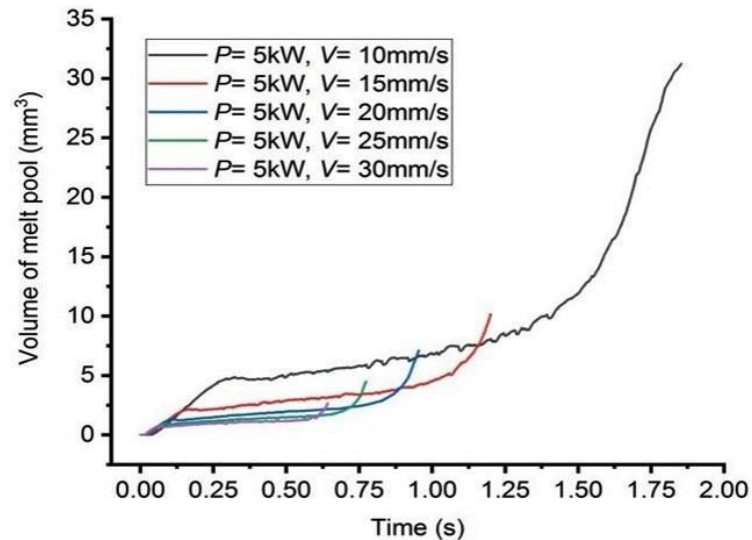


Figure 4.7 Variation of melt pool volume with the scanning speed.

The growth of the melt pool over time is seen in **Figure 4.7**. The time indicated on the x-axis corresponds to the distance travelled by the laser beam along the scanning line. Based on **Figure 4.7**, it is concluded that the melt volume is most significant while welding at slower scanning speeds. When scanning at a speed of 10mm/s, the melt pool stabilises after around 0.25 seconds. When using a laser with a power of 5 kW and a scanning speed of 10 mm/s, the melt pool volume achieved at 0.25 s is around 5 mm³. In response to an additional increase in scanning speed, the melt pool volume diminishes and eventually becomes practically constant at scanning speeds greater than 25 mm/s. Heat build-up causes a rapid volume rise at the plate's end. The accumulation is particularly noticeable when scanning at slower rates because of the prolonged irradiance time. When the scanning speed is 10 mm/s, the melt pool stabilises after approximately 0.25 seconds.

Figure 4.8 depicts the evolution of melt pool volume as a function of scanning time and distance. By examining the plots, it is evident that the melt pool volume grows from 0.2339 mm³ in the initial time step to 3.177 mm³ by the time the beam reaches the end of the plate.

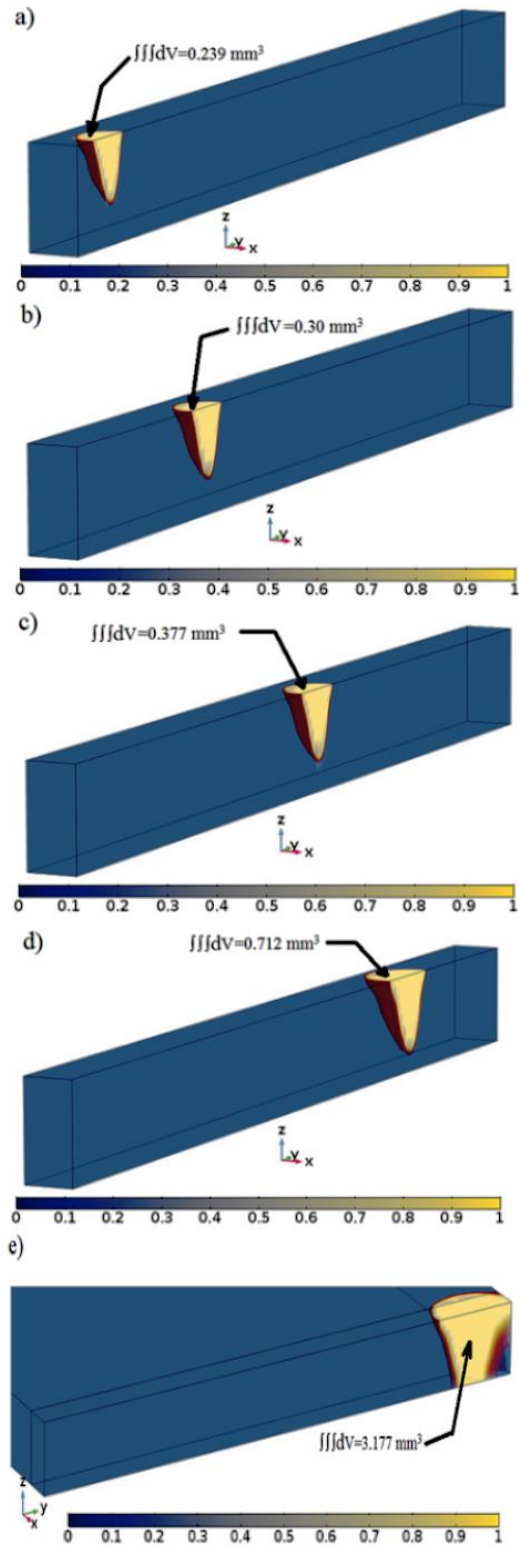


Figure 4.8 Pictorial representation of the evolution of weld pool during welding at (a) 1 mm, (b) 5 mm, (c) 10 mm, (d) 15 mm, and (e) 19.5 mm (Parameters. laser power = 5 kW, scanning speed = 15 mm/s, and beam radius = 0.36 mm).

4.6.3 Effect of Marangoni convection on weld pool dimensions

Phase separation and spatial velocity field caused by Marangoni convection are shown in **Figure 4.9**. The observations were obtained using a laser with a power of 5 kW, a scanning speed of 15 mm/s, and a beam radius of 0.36 mm. It has been found that the surface tension acting on the weld pool results in a velocity pattern directed towards the edge of the keyhole. The velocity of the molten fluid is calculated to be 0.6446 mm/s. **Figure 4.10** depicts the direction of natural convection in the weld pool as well as the change in velocity of the molten fluid during the welding process. High-temperature zones have higher surface tension, which causes a radially inward flow of hot metal, which results in deeper welds. Conversely, low-temperature regions have lower surface tension, which results in broader welds.

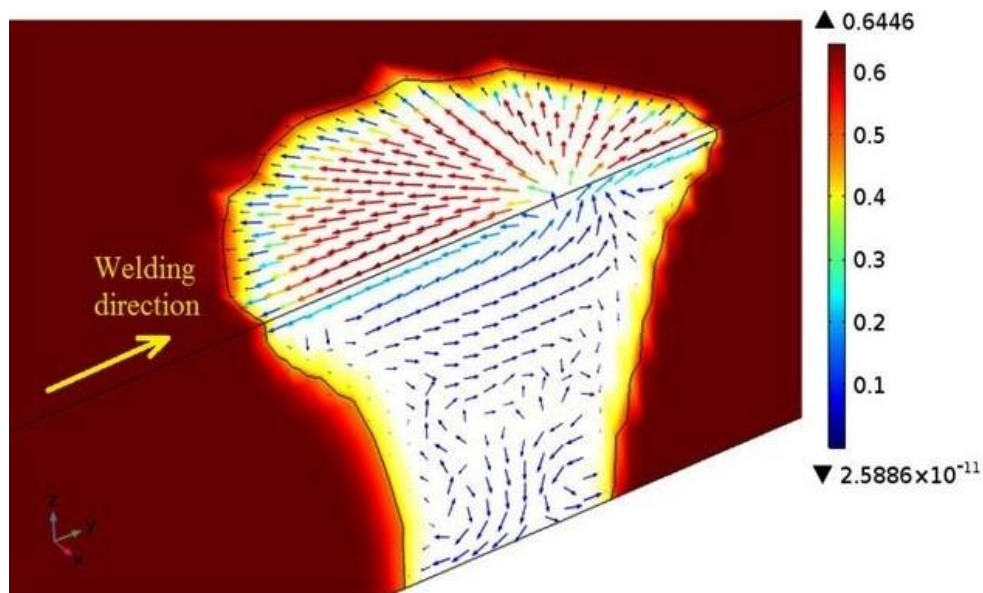


Figure 4.9 Phase separation and spatial velocity field due to Marangoni convection (Parameters. laser power = 5 kW, scanning speed = 15 mm/s, beam radius = 0.36 mm).

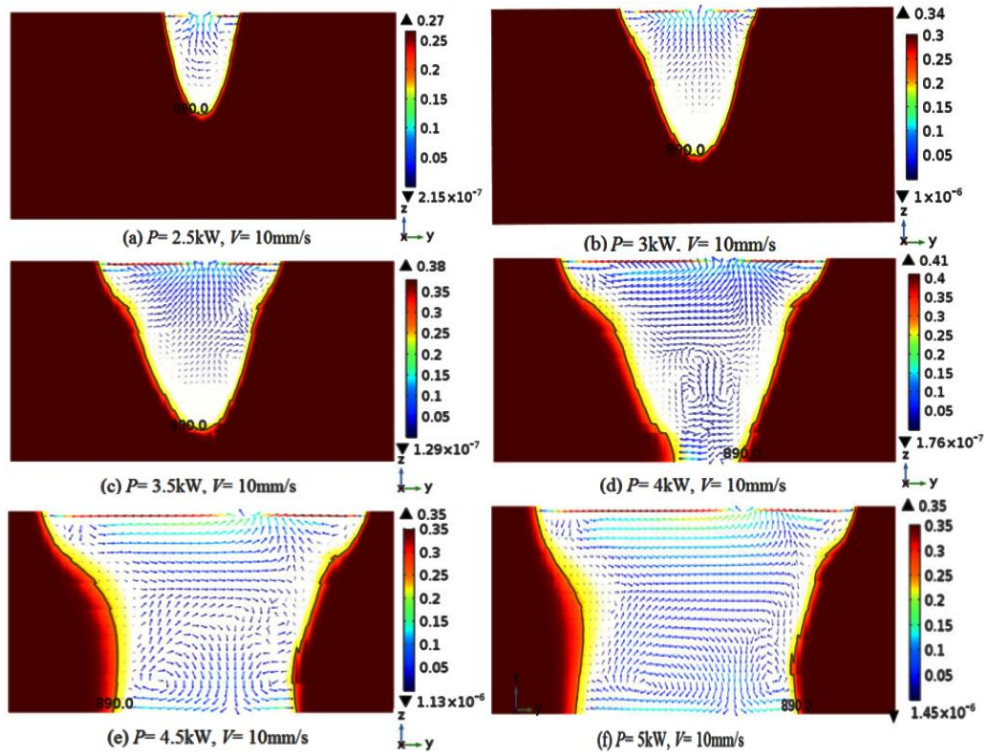


Figure 4.10 Direction of natural convection of the molten pool on YZ plane for different laser power, (a) $P = 2.5 \text{ kW}$, (b) $P = 3 \text{ kW}$, (c) $P = 3.5 \text{ kW}$, (d) $P = 4 \text{ kW}$, (e) $P = 4.5 \text{ kW}$, (f) $P = 5 \text{ kW}$, at scanning speed = 10 mm/s , and beam radius = 0.36 mm .

In **Figure 4.11**, the fluid flow patterns demonstrate the impact of scanning speeds on melt circulation and the direction of natural convection. The velocity of the molten pool is changed between 0.35 m/s for the lowest level of scanning speed and 0.39 m/s for the most significant level of scanning speed. The lowest level of scanning speed is 0.35 m/s , and the highest level of scanning speed is 0.39 m/s . **Figure 4.12** displays the velocity field in two planes that are mutually perpendicular to one another (along the scanning line and perpendicular to it).

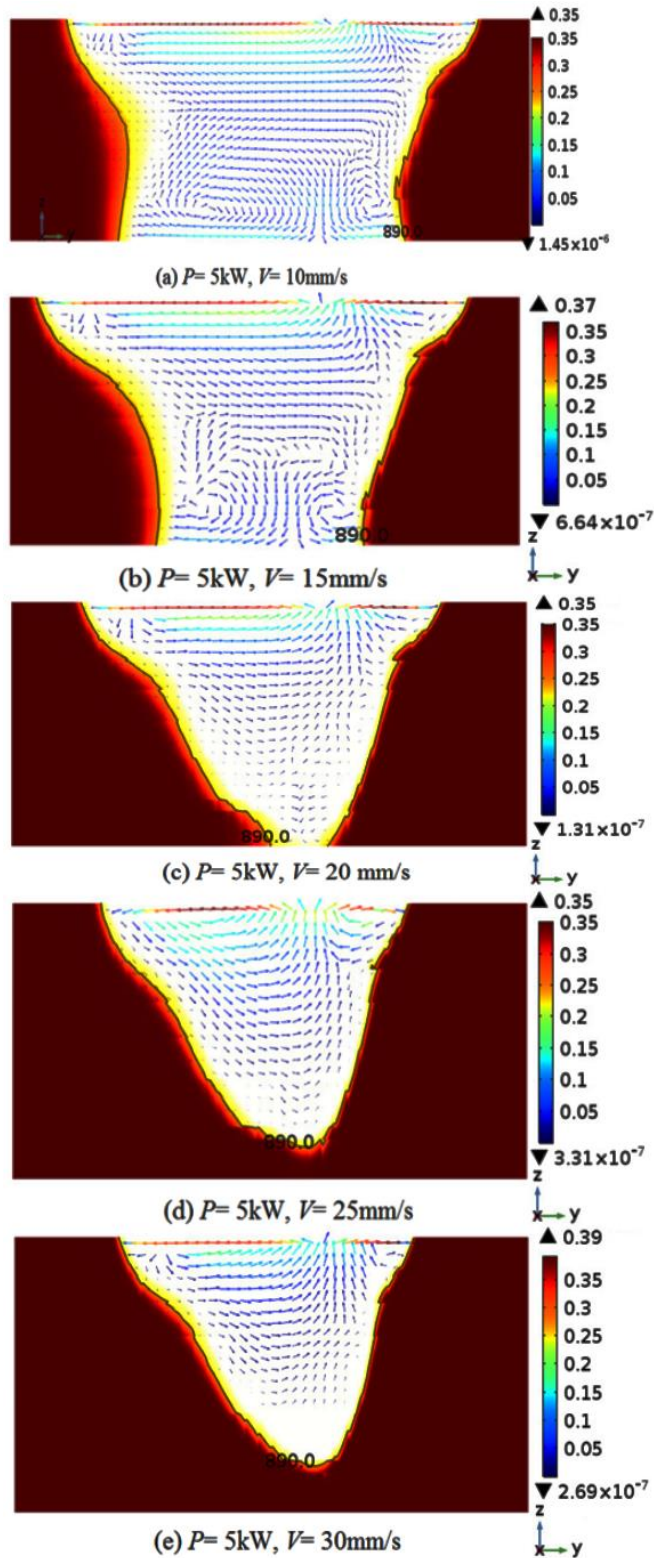


Figure 4.11 The direction of natural convection of the molten pool on the YZ plane for different scanning speeds, (a). $V=10\text{mm/s}$. (b) $V=15\text{mm/s}$. (c). $V=20\text{mm/s}$. (d). $V=25\text{mm/s}$. (e). $V=30\text{mm/s}$, at laser power = 5kW and beam radius = 0.36mm.

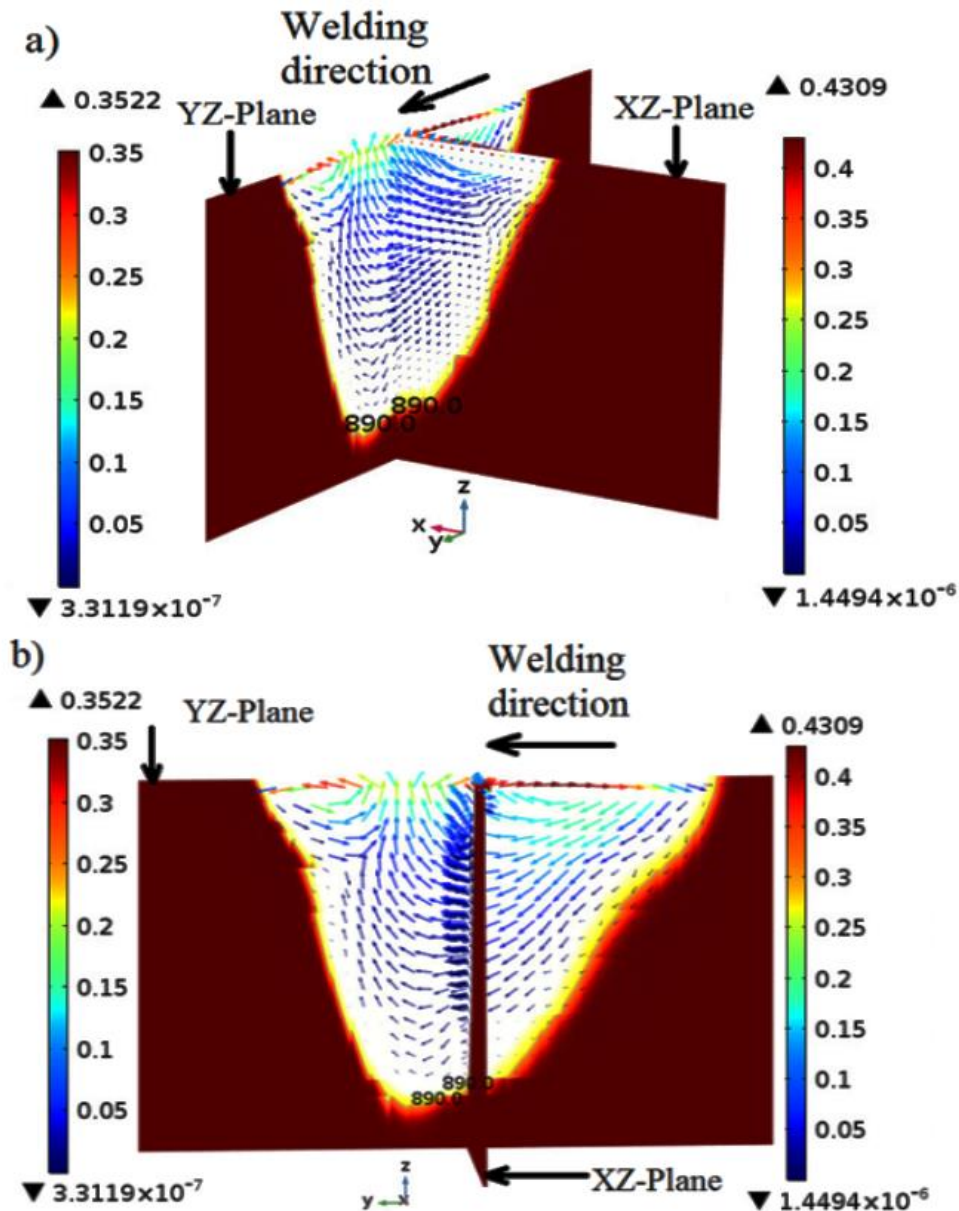


Figure 4.12 Velocity field in YZ-XZ planes (a). Isometric view of the velocity field in two mutually perpendicular places. (b). Front view for laser power = 5 kW, scanning speed = 25 mm/s, and beam radius = 0.36 mm.

The velocity pattern in a plane perpendicular to the scanning line is represented in **Figure 4.12 (a)**. This data is taken along the scanning line. The fluid has a velocity of 0.3522 m/s along the Y-Z plane and 0.4309 m/s along the plane perpendicular to its travel plane. This trend shows that the fluid is behaving more violently, showing its impact on weld width. **Figure 4.12(b)** shows the X-Z plane's alignment and the direction in which the welding takes place. An increase in the fluid velocity in the X-Z plane is noticed, which is 0.4309 m/s greater than

the velocity of the fluid in the Y-Z plane. An extremely intense melt flow emerges, leading to a weld with a larger aspect ratio.

4.7 Dimensionless melt pool simulation and analysis

The scatter plots depicted in **Figure 4.13** show the relationships between the width of the dimensionless melt pool and the dimensionless numbers. These plots help comprehend the inter-relationships between the process components while taking into account the uncertainty in the procedure. The plots' outputs are the Marangoni number and the Peclet number, defined in terms of the normalised value of the pool width, respectively. It is necessary to transform the actual weld width into a dimensionless width with a normalised value w/L to treat all variables as unitless.

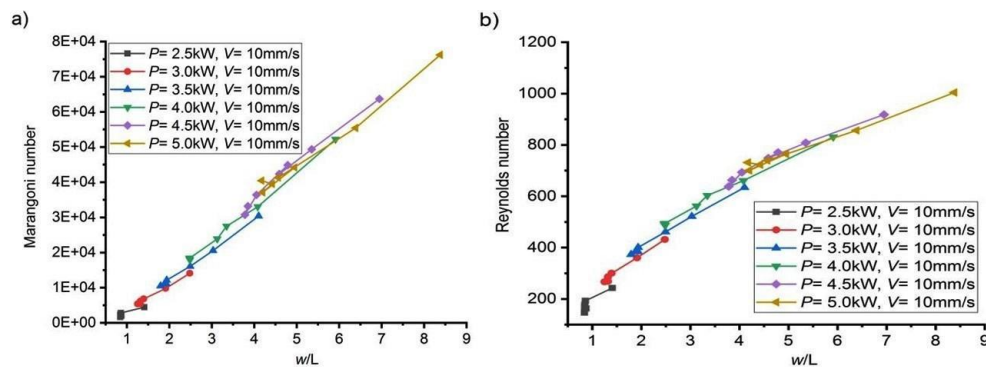


Figure 4.13 Scatter plots of (a) dimensionless width vs Marangoni number. (b). dimensionless width vs Reynold number for different levels of laser power.

It can be shown in **Figure 4.13 (a)** that increased laser power has resulted in a more significant Marangoni number at each given time step. When direct heat is applied, the molten pool volume increases, and the Marangoni number increases. In the molten pool, the velocities are more significant, and the Marangoni number varies in the order of 10^4 , which indicates that surface tension and Marangoni convection are the primary modes of convective transport in the melt pool. The same is true when dimensionless width is plotted versus Reynolds number, with a value of 1000 being recorded. The obtained Reynolds number shows that the flow in the melt pool is laminar. In **Figure 4.14 (a-b)**, a plot of dimensionless numbers vs dimensionless width of the melt pool at different scanning speeds is depicted, and a similar trend is found in both cases. The graph

constructed between the dimensionless width and the melt pool in **Figure 4.14** (a) shows that the Marangoni number is more significant at lower scanning speeds. As a result, at lower scanning speeds, the Marangoni convection dominates. Based on **Figure 4.14** (b), it can be noticed that the Reynolds number is more significant at slower scanning speeds. As a result, the melt pool is laminar at relatively lower scanning speeds.

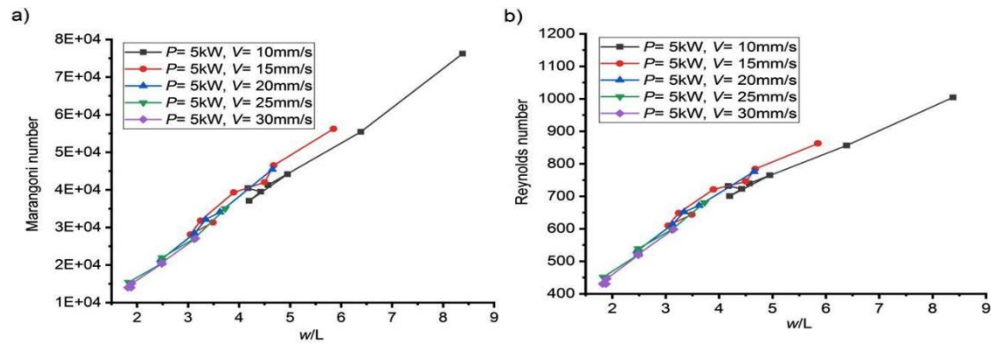


Figure 4.14 Scatter plots of (a) dimensionless width vs Marangoni number. (b) dimensionless width vs Reynold number for different levels of scanning speed.

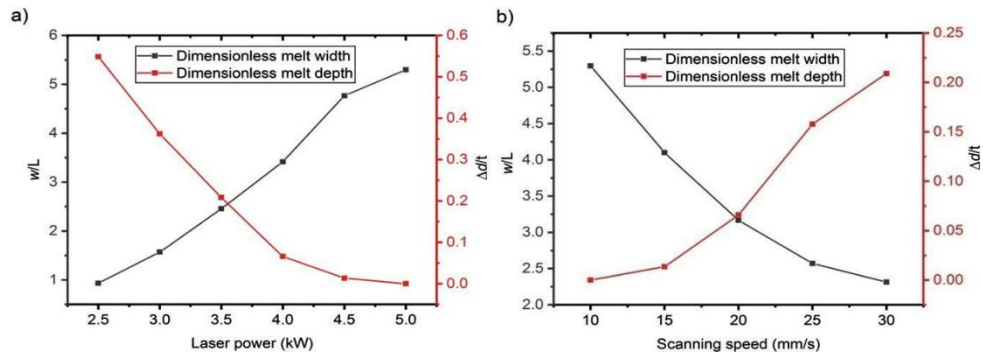


Figure 4.15 Variations of dimensionless melt pool dimensions with (a) Laser power, (b) Scanning speed.

Figure 4.15 depicts the relationship between laser power and scanning speed and the change in melt size in dimensionless melt width and depth. It is predicted that when the laser intensity is varied, the dimensionless melt breadth increases while the depth decreases, as seen in **Figure 4.15**. (a). The melt width has risen due to the heat accumulated by the workpiece during the melting process. **Figure 4.15** (b) shows that the dimensionless melt depth has dropped while the melt width has expanded due to the change in scanning speed.

4.8 Summary

1. The impact of Marangoni convection and buoyancy forces on laser welding on aluminium alloy is studied in this work. This computational model agrees well with published experimental results, with a maximum error of 5% in penetration depth and 3% in weld width. A solid-liquid model accurately depicts the molten pool's temperature distribution and fluid flow.
2. The system attained a temperature of 2075.3 K. Temperature profiles, and fluid flow is illustrated.
3. The molten pool resembled an hourglass. Raising the laser power has increased the average weld width and depth of melting. The change in scanning speed demonstrated a declining trend in weld width and depth.
4. Due to increased laser fluence, higher laser power raises melt pool volume. The maximum melt pool volume is 5 kW. At 2.5 kW, no substantial melt pool is noticed until the beam reaches the plate's end.
5. The surface tension on the weld pool causes a velocity pattern towards the keyhole edge. For the fastest scanning speed, the molten fluid velocity is 0.6446 m/s. At the slowest scanning speed, the fluid moves at 0.3522 m/s in the Y-Z plane and 0.4309 m/s in the plane perpendicular to it. While hot metal flowing towards the weld pool's edge produces broader welds, higher temperatures cause surface tension and a radially inward flow that produces deeper welds. A high melt flow produces a weld with a more significant aspect ratio.
6. Higher laser power has resulted in a higher Marangoni number. The molten pool has greater velocities and a Marangoni number of about 10^4 , suggesting that surface tension and Marangoni convection dominate. Similarly, plotting dimensionless width versus Reynolds number yields 1000. This plot suggests laminar flow in the melt pool due to the lower scanning speed. The dimensionless melt width grew with laser power while the depth dropped.

Chapter 5: Experimental investigation on laser welding of AA 2024

5.1 Introduction

This chapter discusses the experimental investigation conducted to understand the effect of process parameters on quality aspects of the weld and also gives a technological database of laser welding of aluminium alloy 2024. The structured experiments are performed using the Nd-YAG laser welding machine. This work studies the weld metrics, viz., weld width and depth of penetration and the defects that occurred during the welding, along with the metallurgical aspects. The design of experiments is used to obtain better weld quality out of the resources at hand. Empirical models are generated to determine the relationship between the process parameters and the weld quality. The optimal welding circumstances for the intended optimisation criteria are determined using the constructed empirical models when the quality parameters are at the desired values. Each parameter's impact on weld quality properties is determined, and the ideal welding circumstances are obtained.

5.2 Laser welding of the AA 2024

Laser welding of aluminium alloys is investigated in the present work. Rolled sheets of aluminium alloy 2024, cut into the required sizes, are used as the work materials. Structured experiments and further analysis are accomplished to develop empirical models and estimate the optimum parametric combination. Along with the parametric optimisation, the features observed during the experimental investigation are also explained. The significance of the input process parameters on the overall weld quality is analysed quantitatively using the analysis of variance (ANOVA) methodology.

5.2.1 Experimental details

Selection of range of parameters

Peak power, scanning speed, frequency and pulse width are the independently controlled process parameters for performing the experiments, while the shielding gas flow rate is kept constant at 3 bars. The air gap between the samples is kept as minimum as possible by mechanical filing and polishing the work samples. Bead-on plate experiments are conducted in the trail phase to find the best possible range on the excellent welding of the target material. The input parameters of the process and their ranges, along with units and limits, are mentioned in **Table 5.1**.

Table 5.1 Process control parameters and their limits

Parameters	Units	Notations	Limits				
			-2	-1	0	+1	+2
Peak Power	kW	<i>A</i>	4.00	4.25	4.50	4.75	5.00
Scanning Speed	mm/s	<i>B</i>	1.0	1.4	1.8	2.2	2.6
Frequency	Hz	<i>C</i>	6	7	8	9	10
Pulse Width	ms	<i>D</i>	5	6	7	8	9

5.3 Empirical modelling using RSM

Structured experiments and additional analysis are carried out to construct mathematical models for determining the relationship between process and weld quality characteristics. The adequacy of the developed model is tested using analysis of variance (ANOVA). Design-Expert software analyses the obtained responses and determination of the mathematical model with the best fit. The effect of each welding process parameter and the weld quality attributes are studied using the developed mathematical model.

5.3.1 Results of the experiment

Table 5.2 depicts the design matrix employed for the experimentation and their results as measured after the completion of the welding process.

Table 5.2 Design matrix and measured experimental results.

Sl. No	Peak Power (kW)	Scanning Speed (mm/s)	Frequency (Hz)	Pulse Width (ms)	Depth of penetration (mm)	Weld width (mm)
1	4.25	1.4	7	6	1.56	1.23
2	4.75	1.4	7	6	1.82	1.36
3	4.25	2.2	7	6	1.14	1.01
4	4.75	2.2	7	6	1.33	1.12
5	4.25	1.4	9	6	1.41	1.20
6	4.75	1.4	9	6	1.75	1.31
7	4.25	2.2	9	6	1.33	1.15
8	4.75	2.2	9	6	1.57	1.22
9	4.25	1.4	7	8	1.76	1.38
10	4.75	1.4	7	8	1.88	1.42
11	4.25	2.2	7	8	1.54	1.20
12	4.75	2.2	7	8	1.43	1.19
13	4.25	1.4	9	8	1.37	1.15
14	4.75	1.4	9	8	1.43	1.19
15	4.25	2.2	9	8	1.31	1.10
16	4.75	2.2	9	8	1.39	1.15
17	4.00	1.8	8	7	1.41	1.18
18	5.00	1.8	8	7	1.73	1.33
19	4.50	1.0	8	7	1.80	1.35
20	4.50	2.6	8	7	1.26	1.08
21	4.50	1.8	6	7	1.51	1.21
22	4.50	1.8	10	7	1.28	1.08
23	4.50	1.8	8	5	1.47	1.18
24	4.50	1.8	8	9	1.56	1.22
25	4.50	1.8	8	7	1.51	1.20
26	4.50	1.8	8	7	1.49	1.21
27	4.50	1.8	8	7	1.48	1.20
28	4.50	1.8	8	7	1.51	1.20
29	4.50	1.8	8	7	1.51	1.21
30	4.50	1.8	8	7	1.48	1.19

Analysis of weld width

The fit summary for the butt joint weld width suggests a quadratic connection with considerable additional factors, and the model is not aliased. The ANOVA table showing the adequacy indicators like R^2 , *adjusted R²* and *predicted R²* are

shown in **Table 5.3**. The corresponding p-value lower than 0.05 for the model (i.e., 95% confidence level) suggests that the model terms are statistically significant [151]. The *lack-of-fit* value of the model suggests non-significance, which is as expected.

The ANOVA results indicate that peak power (*A*), scanning speed (*B*), frequency (*C*), pulse width (*D*), the quadratic effect of the Peak power (A^2), frequency (C^2), the interaction effect of peak power and scanning speed (*AB*), peak power and pulse width (*AD*), scanning speed and frequency (*BC*), frequency and pulse width (*CD*) are significant factors related to the weld width in this case study. The other terms mentioned in the model are insignificant and hence, eliminated by the backward elimination process to enhance the model's accuracy. The ANOVA table related to the reduced quadratic model is given in **Table 5.4**. After elimination, the peak power (*A*), scanning speed (*B*), frequency (*C*), pulse width (*D*), the quadratic effect of the Peak power (A^2), frequency (C^2), and the interaction effect of peak power and pulse width (*AD*), scanning speed and frequency (*BC*), frequency and pulse width (*CD*) are significant factors. The terms in the model point out that the model is significant with a *p*-value lower than 0.05. The other indicators of adequacy, like R^2 , *adjusted R²* and *predicted R²* are in agreement and possess a value close to 1, depicting the adequacy of the model. These values guarantee that the higher-order model suitably fits the experimental data. An *adequate precision* ratio of 53.230 is obtained from the model, indicating the signal-to-noise ratio's adequacy. (Any value higher than four is considered good). The term *lack-of-fit* has a value of 3.44, which indicates that the significance of *lack-of-fit* is lesser than that of *pure error*. The following is the mathematical model for the weld strength, which gives prediction within the same design space:

Table 5.3 ANOVA for the weld width model (before elimination).

Source	Sum of Squares	df	Mean Square	F Value	p-value Prob > F	
Model	0.24595	14	0.01757	117.99	< 0.0001	Significant
A-Peak Power	0.02940	1	0.02940	197.46	< 0.0001	
B-Scanning Speed	0.11207	1	0.11207	752.69	< 0.0001	
C-Frequency	0.02042	1	0.02042	137.13	< 0.0001	
D-Pulse width	0.00282	1	0.00282	18.92	0.0006	

<i>AB</i>	0.00062	1	0.00062	4.20	0.0584	
<i>AC</i>	0.00000	1	0.00000	0.00	1.0000	
<i>AD</i>	0.00563	1	0.00563	37.78	< 0.0001	
<i>BC</i>	0.02560	1	0.02560	171.94	< 0.0001	
<i>BD</i>	0.00063	1	0.00063	4.20	0.0584	
<i>CD</i>	0.03610	1	0.03610	242.46	< 0.0001	
<i>A</i> ²	0.00583	1	0.00583	39.18	< 0.0001	
<i>B</i> ²	0.00058	1	0.00058	3.87	0.0679	
<i>C</i> ²	0.00458	1	0.00458	30.74	< 0.0001	
<i>D</i> ²	0.00002	1	0.00002	0.13	0.7256	
Residual	0.00223	15	0.00015			
<i>Lack-of-Fit</i>	0.00195	10	0.00020	3.44	0.0925	not significant
<i>Pure Error</i>	0.00028	5	0.00006			
Cor Total	0.24819	29				

<i>R-Squared</i>	0.9910
<i>Adj R-Squared</i>	0.9826
<i>Pred R-Squared</i>	0.9531
<i>Model Precision</i>	46.746

Table 5.4 ANOVA analysis for the weld width model (after elimination).

Source	Sum of Squares	d f	Mean Square	F Value	p-value Prob > F	
		1				
Model	0.24593	2	0.02049	154.68	< 0.0001	significant
<i>A</i> -Peak Power	0.02940	1	0.02940	221.90	< 0.0001	
<i>B</i> -Scanning Speed	0.11207	1	0.11207	845.83	< 0.0001	
<i>C</i> -Frequency	0.02042	1	0.02042	154.10	< 0.0001	
<i>D</i> -Pulse width	0.00282	1	0.00282	21.26	0.0002	
<i>AB</i>	0.00062	1	0.00062	4.72	0.0443	
<i>AD</i>	0.00563	1	0.00563	42.46	< 0.0001	
<i>BC</i>	0.02560	1	0.02560	193.22	< 0.0001	
<i>BD</i>	0.00063	1	0.00063	4.72	0.0443	
<i>CD</i>	0.03610	1	0.03610	272.47	< 0.0001	
<i>A</i> ²	0.00586	1	0.00586	44.21	< 0.0001	
<i>B</i> ²	0.00056	1	0.00056	4.21	0.0559	
<i>C</i> ²	0.00476	1	0.00476	35.91	< 0.0001	
Residual	0.00225	7	0.00013			
<i>Lack-of-Fit</i>	0.00197	2	0.00016	2.90	0.1244	not significant
<i>Pure Error</i>	0.00028	5	0.00006			
Cor Total	0.24819	9				

<i>R-Squared</i>	0.9909
<i>Adj R-Squared</i>	0.9845
<i>Pred R-Squared</i>	0.9632
<i>Model Precision</i>	53.230

The following are the final mathematical models for weld width that can be utilised for prediction within the same design space is given as :

a. In terms of coded factors

$$\text{Weld width} = 1.20 + 0.035 * A - 0.068 * B - 0.029 * C + 0.011 * D - 6.250 * E - 003 * A * B - 0.019 * A * D + 0.040 * B * C + 6.250 * E - 003 * B * D - 0.047 * C * D + 0.014 * A * A + 4.464 * E - 003 * B * B - 0.013 * C * C.$$

b. In terms of actual factors

$$\text{Weld width} = 1.08829 - 1.30536 * A - 0.89940 * B + 0.33190 * C + 0.70021 * D - 0.062500 * A * B - 0.075000 * A * D + 0.10000 * B * C + 0.015625 * B * D - 0.047500 * C * D + 0.23143 * A * A + 0.027902 * B * B - 0.013036 * C * C$$

Analysis of the depth of penetration

The fit analysis for penetration depth in the weld seam case indicates a quadratic connection in which the additional terms are relevant, and the model is not aliased. **Table 5.5** depicts the ANOVA table for the quadratic model with other adequacy parameters R^2 , *adjusted* R^2 , and *predicted* R^2 . The corresponding p -value is less than 0.05, indicating that the model terms are statistically significant. The *lack-of-fit* value for the model suggests non-significance as desired. The results of ANOVA suggest that the main effects of the input process parameters viz., peak power(A), scanning speed(B), Frequency (C) and pulse width (D), the quadratic effect of the peak power (A^2), frequency(C^2) combined with the interaction effect of the peak power and scanning speed (AB), peak power and frequency (AC), peak power and pulse width (AD), scanning speed and frequency (BC), scanning speed and pulse width (BD), frequency and pulse width (CD) are significant model terms related to the depth of penetration of the weld bead. The rest of the terms in the model are insignificant; hence, they are removed using the back elimination technique to enhance the model's adequacy. The analysis of the variance table for the reduced quadratic model is given in **Table 5.6**. The results of the model presented in **Table 5.6** suggest that the model is significant, with a p -value lower than 0.05. The other metrics of adequacy,

like R^2 , *adjusted R²* and *predicted R²* are in reasonable agreement by being close to 1, inferring the adequacy of the model. The value of the *adequate precision* ratio is 38.921, which means good model discrimination. The *lack-of-fit f*-value of 0.0536 denote that the *lack-of-fit* is insignificant compared to the *pure error*.

Table 5.5 ANOVA for the depth of penetration model (before elimination).

Source	Sum of Squares	df	Mean Square	F Value	p-value Prob > F	
		1				
Model	0.9089	4	0.0649	85.99	< 0.0001	Significant
<i>A-Peak Power</i>	0.1380	1	0.1380	182.80	< 0.0001	
<i>B-Scanning Speed</i>	0.3800	1	0.3800	503.33	< 0.0001	
<i>C-Frequency</i>	0.0771	1	0.0771	102.08	< 0.0001	
<i>D-Pulse width</i>	0.0060	1	0.0060	7.97	0.0129	
<i>AB</i>	0.0090	1	0.0090	11.95	0.0035	
<i>AC</i>	0.0042	1	0.0042	5.60	0.0319	
<i>AD</i>	0.0484	1	0.0484	64.11	< 0.0001	
<i>BC</i>	0.0930	1	0.0930	123.21	< 0.0001	
<i>BD</i>	0.0100	1	0.0100	13.25	0.0024	
<i>CD</i>	0.1089	1	0.1089	144.24	< 0.0001	
<i>A²</i>	0.0090	1	0.0090	11.93	0.0035	
<i>B²</i>	0.0018	1	0.0018	2.40	0.1423	
<i>C²</i>	0.0180	1	0.0180	23.86	0.0002	
<i>D²</i>	0.0005	1	0.0005	0.70	0.4174	
<i>Residual</i>	0.0113	5	0.0008			
		1				
<i>Lack of Fit</i>	0.0102	0	0.0010	4.50	0.0554	not significant
<i>Pure Error</i>	0.0011	5	0.0002			
		2				
Cor Total	0.9202	9				
<i>R-Squared</i>	0.9877					
<i>Adj R-Squared</i>	0.9762					
<i>Pred R-Squared</i>	0.9344					
<i>Model Precision</i>	37.057					

Table 5.6 ANOVA for the depth of penetration model (after elimination).

Source	Sum of Squares	df	Mean Square	F Value	p-value Prob > F	
Model	0.9068	12	0.0756	95.69	< 0.0001	significant
<i>A-Peak Power</i>	0.1380	1	0.1380	174.77	< 0.0001	
<i>B-Scanning Speed</i>	0.3800	1	0.3800	481.21	< 0.0001	
<i>C-Frequency</i>	0.0771	1	0.0771	97.59	< 0.0001	
<i>D-Pulse width</i>	0.0060	1	0.0060	7.62	0.0134	
<i>AB</i>	0.0090	1	0.0090	11.43	0.0036	
<i>AC</i>	0.0042	1	0.0042	5.35	0.0335	
<i>AD</i>	0.0484	1	0.0484	61.29	< 0.0001	
<i>BC</i>	0.0930	1	0.0930	117.80	< 0.0001	
<i>BD</i>	0.0100	1	0.0100	12.66	0.0024	
<i>CD</i>	0.1089	1	0.1089	137.90	< 0.0001	
<i>A²</i>	0.0078	1	0.0078	9.88	0.0059	
<i>C²</i>	0.0210	1	0.0210	26.62	< 0.0001	
<i>Residual</i>	0.0134	17	0.0008			
<i>Lack-of-fit</i>	0.0123	12	0.0010	4.52	0.0536	not significant
<i>Pure Error</i>	0.0011	5	0.0002			
Cor Total	0.9202	29				

R-Squared 0.9854
Adj R-Squared 0.9751
Pred R-Squared 0.9363
Model Precision 38.921

The final mathematical model for the depth of penetration for the weld bead, as given by the design expert software, is given as

a. In terms of coded factors

$$\text{Depth of penetration} = 1.51 + 0.076 * A - 0.13 * B - 0.057 * C + 0.016 * D - 0.024 * A * B + 0.016 * A * C - 0.055 * A * D + 0.076 * B * C + 0.025 * B * D - 0.082 * C * D + 0.017 * A * A - 0.027 * C * C$$

b. In terms of actual factors

$$\text{Depth of penetration} = -2.92208 - 0.63417 * A - 1.20833 * B + 0.32021 * C + 1.55333 * D - 0.23750 * A * B + 0.065000 * A * C - 0.22000 * A * D + 0.19063 * B * C + 0.062500 * B * D - 0.082500 * C * D + 0.26500 * A * A - 0.027188 * C * C.$$

5.4 Validation of the developed models

The produced response surface equations obtained from the multiple regression analysis are confirmed by executing three trials with the input parameters chosen randomly within the defined limits for which the equations are acquired. The exact findings are computed by taking the average of the three measured responses for each response. Table 5.7 shows the actual outcomes, expected results, and calculated % error of the validation experiments. The trials show that there is a minimal error % between the estimated and experimental values, indicating that the models stated are appropriate for use in real-time problems.

Table 5.7 Validation test results

S.No	P (kW)	V (mm /sec)	F (Hz)	pw (mS)	Actual values		Predicted values		Error (%)	
					WW (μm)	DP (μm)	WW (μm)	DP (μm)	WW	DP
1	4	1	6	5	1357.46	750	1255.89	763.7	8	1.79
2	4.25	2	7	8	1615.23	2000	1655.42	2038.1	1.7	1.8
3	4.5	1.5	6	7	1755.21	2000	1725.36	2057.8	2.5	2.8
4	4.75	2.5	9	8	1957.55	1890	1919.5	1816.30	1.8	3

Design-Expert® Software
Depth of penetration

Color points by value of
Depth of penetration:
1.88
1.14

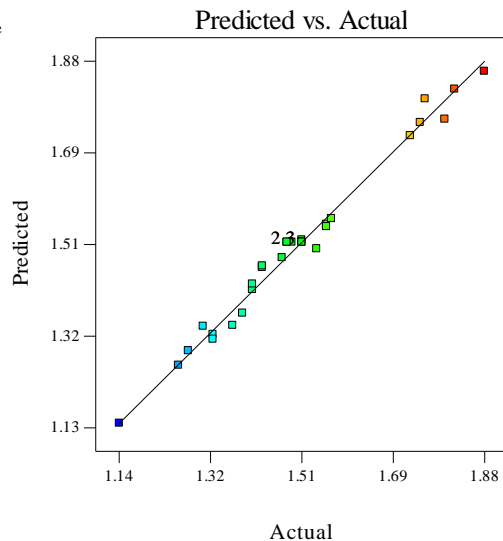


Figure 5.1 Plot of actual vs predicted response of depth of penetration results.

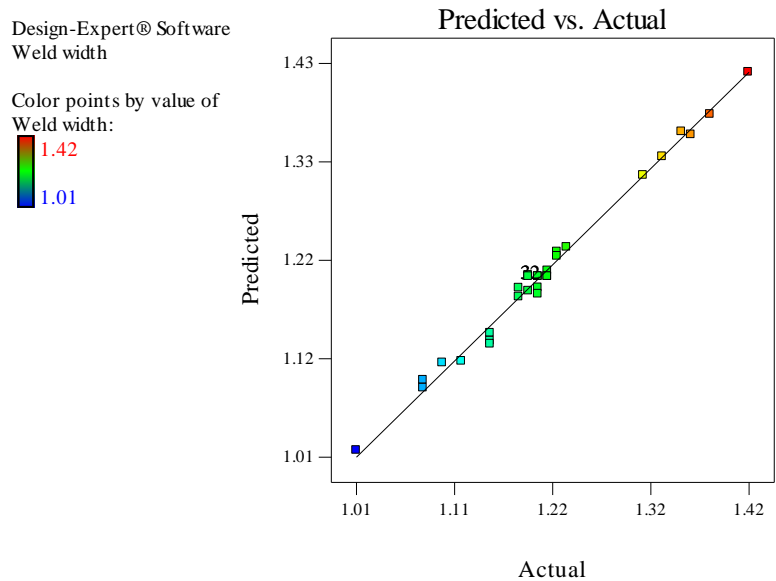


Figure 5.2 Plot of actual vs predicted response of weld width results.

Figures 5.1 and **5.2** show the graphs obtained between the predicted response against the depth of penetration and weld width. These figures show that the models are adequate, and the predicted results match the measured data with minimum deviation.

5.5 Effect of process parameters on the responses

The perturbations plot in **Figure 5.3** demonstrates the influence of all the factors at the centre point in the design space. It is clearly understood from the figure that scanning speed and frequency have a negative impact on the depth of penetration. A higher scanning speed moves the beam away from the irradiation site faster, reducing the available power. Frequency influences the energy accumulation by the number of pulses impinging on the joint. A higher number of pulses increases the available power. However, with a higher scanning speed, the distance between each pulse increases, reducing the irradiation time and area.

Consequently, the depth of penetration decreases. An increase in the peak power raises the available radiation, melting more material and penetrating deeper into the joint. The pulse width also increases the irradiation and the depth of penetration. **Figure 5.4** depicts the effect of input process parameters on the weld width. The parameters that influence the depth of penetration influence the

weld width also. The peak power and pulse width increase the weld width, while the scanning speed and frequency show a negative impact.

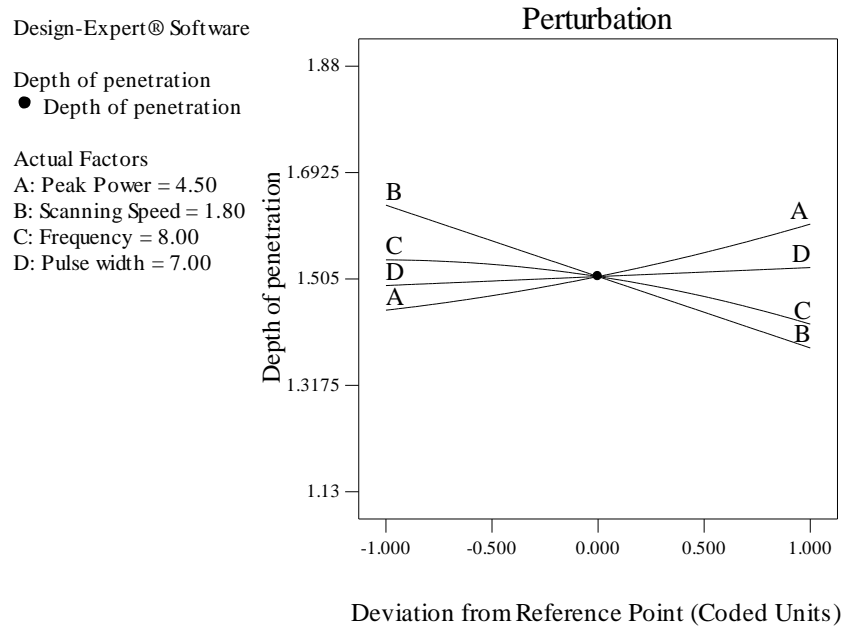


Figure 5.3 Perturbation plot shows all factors' effects on the penetration depth.

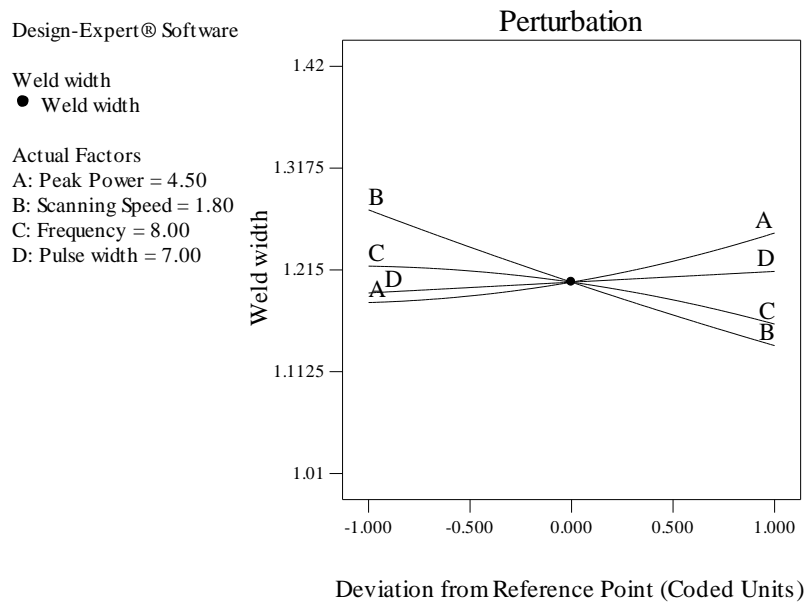


Figure 5.4 Perturbation plot shows all factors' effects on the weld width.

Regarding the interaction between the peak power and scanning speed, as shown in **Figures 5.5** and **5.6**, it is clear that the depth of penetration decreases when the scanning speed is increased. This trend is because of the rise in the available

power due to the slow movement of the beam. This rise in power helps in forming a good bond. The total depth of penetration which is desirable and leads to the formation of a keyhole is the consequence of the higher available peak power.

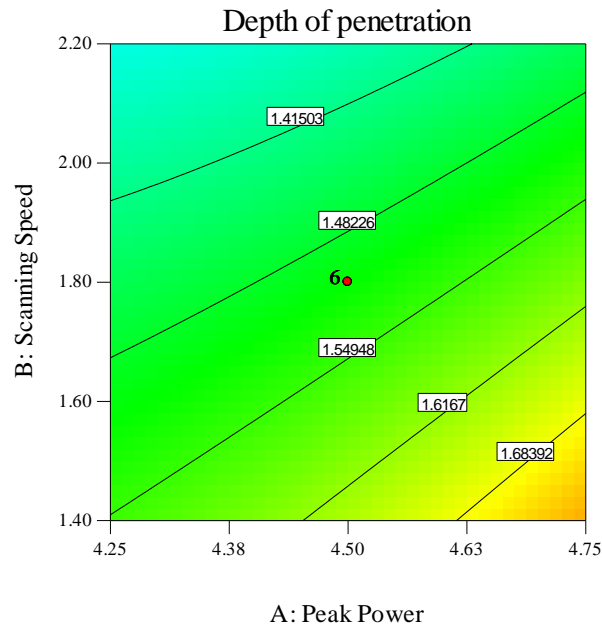


Figure 5.5 Contour plots indicating the effect of peak power and scanning speed at a frequency of 8Hz and pulse width of 7 ms.

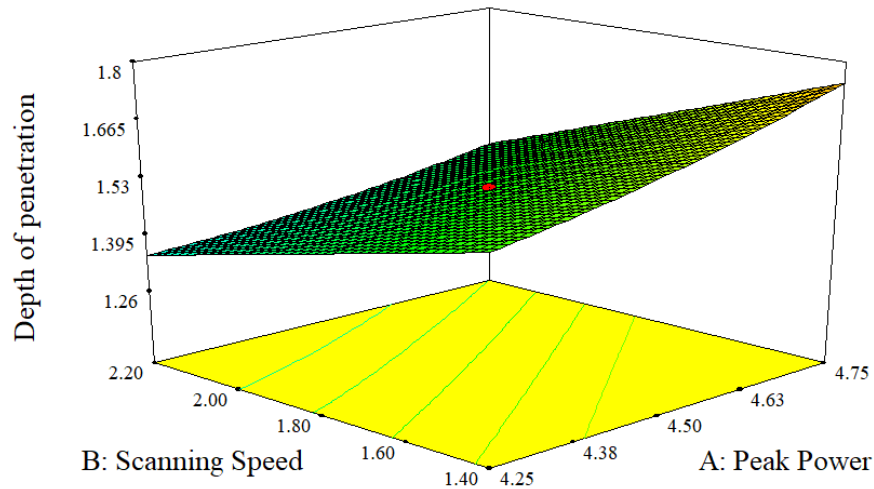


Figure 5.6 Response surface plot between peak power and scanning speed. Response surface plots indicate the effect of peak power and scanning speed at a frequency of 8Hz and pulse width of 7ms.

5.6 Results and discussion on welded specimens

The experiments are performed according to the guidelines mentioned in BS EN ISO 15614-11 and BS EN ISO 13919-2 for AA 2024 without filler wire. These standards guide the defects' levels while welding with a laser beam. The quality levels are termed moderate (D), intermediate (C), and stringent (B). These standards help the users to decide if the welded components are suitable for the designated application [151]. The quality level of moderate is considered for this study. **Table 5.8** lists the necessary tests to be conducted on welded joints in line with the guidance given in acceptance level D as mentioned in BS EN ISO 15614-11: 2002.

Table 5.8 Tests to be conducted on welded joints [151]

Sample	Type of test	Degree of the test
Butt joint weld	Visual inspection	100%
	Radiographic inspection	If needed
	Ultrasonic inspection	If needed
	Surface crack detection	If needed
	Metallographic measurement	At least one section

Table 5.8 shows the welded samples' visual inspection and the prepared welded specimens' metallographic measurements. The sample preparation for the metallographic study is mentioned in chapter 3. It was vital to examine the conformance of the weld joints since at least one piece had to be removed from the weld for metallographic analysis. A single weld cross-section could not guarantee the homogeneity of weld bead geometry across the whole weld joint for each welding parameter configuration. The conformance of weld bead geometry needs to be investigated to establish indicative trends in variations of the weld bead geometry for different welding conditions. The following techniques could be used to verify the consistency of weld seam geometry over the whole weld: obtaining segments parallel to the welding direction or generating lots of samples with identical specifications. However, given the

number of parameter modifications evaluated in this study, it was impractical to use these approaches because they require much time, effort, and material expenditures. Instead, the conformance of the weld seam geometry was determined by looking at the shape and quality of the top and bottom weld seam surfaces. Random weld joint evaluations revealed a favourable correlation between the consistency of the weld morphology and the quality of the top and bottom surfaces of the welds. A central cross-section, which is close to the weld start, and a cross-section close to the weld end were all extracted. Following the test procedures outlined in BS EN 1321 [133], transverse sections of metallographically welded specimens were subjected to macroscopic and microscopic inspection. In order to reveal the characteristics of welded joints, both a macroscopic inspection under low magnification and a microscopic examination under a magnification between 50 and 500 times were undertaken using etching. The chemical compositions of the specimens were determined using energy dispersive X-ray spectroscopy (EDX) in an environmental scanning electron microscope (SEM).

5.6.1 Welding Quality Acceptance Criteria

The quality of the weld joints obtained in this study was analysed depending on the guidelines laid down by the American welding society standards AWS D17.1:200, European standards BS EN ISO 13919-2:2001. This standard discusses the AA 2024 samples. Though American welding society guidelines are for fusion welding, they serve as an essential reckoning guide for the laser welded samples. European Standards BS EN 4678:2011 specifically deal with the laser beam welding of metal samples employed in an aircraft application. They are more stringent than other criteria [152]. **Table 5.9** discusses the guidelines prescribed by each of these standards.

Table 5.0.9 Different weld acceptance criteria

Imperfections	AWS D17.1:200			BS EN ISO 13919-2:2001			BS EN 4678:2011
	Class A	Class B	Class C	D	C	B	AI
Cracks	To be rejected	To be rejected	To be rejected	To be rejected	To be rejected	To be rejected	To be rejected
Incomplete fusion	To be rejected	To be rejected	To be rejected	$\leq 0.25 t$ Max. 1mm	To be rejected	To be rejected	To be rejected
Incomplete penetration	To be rejected	To be rejected	To be rejected	$\leq 0.25 t$ Max. 1mm	To be rejected	To be rejected	To be rejected
Face width	Not applicable	Not applicable	Not applicable	Not applicable	Not applicable	Not applicable	$\leq t + 1mm$
Root width	Not applicable	Not applicable	Not applicable	Not applicable	Not applicable	Not applicable	$\leq t + 0.5mm$
Porosity	$0.33 * t$ or 1.5mm, whichever is smaller	$0.5 * t$ or 2.3 mm, whichever is smaller	Not applicable	$0.5 * t$, max 6mm	$\leq 0.4 * t$, max 5mm	$\leq 0.3 * t$ Max 4mm	$> 0.2 mm$ $\leq 0.3 * t$
Undercut	0.05mm	$0.015 * t$ or 0.05 mm, whichever is smaller	$0.15 * t$, maximum 2mm	$\leq 0.15t$ maximum 2 mm	$\leq 0.1 * t$ maximum 1.5 mm	$\leq 0.05 * t$ maximum 1 mm	$0.1 * t$ or 0.5 mm, whichever is smaller

Table 5.9 indicates that the welds which possess cracks, incomplete fusion or penetration are rejected without any tolerance. Defects like porosity and undercut are the zones for stress concentration. Hence, a limitation is given to these defects. The high scanning speed employed in laser welding leads to defects like humping and undercutting, as there is lesser time for the molten metal to flow back and fill the gap. These defects are detrimental when the components are used in cyclic loading operations where they fail due to fatigue. The acceptance criteria for face and root width are mentioned in European standards for aircraft materials. The face width and root width are essential to

understand the processing stability in case of complete penetration. Chen et al. [153] conducted laser welding experiments on 3mm thick aluminium – lithium alloy 5090 and reported that the weld width ratio higher than 0.6 produced stable full penetration welds.

5.6.1.1 Effect of welding on the microstructure and defect formation of AA 2024.

The fit for the performance of the welded components depends on the weld bead geometry, melt pool attributes during the process, metallurgical transformations between the weld zone and heat-affected zone and the defects that occurred in the joint. These complex interactions yield consequent failure of the weld during its operation. Hence, it is necessary to apprehend all the consequences of the failure of the weld while designing it. According to the American Society of Mechanical Engineers, inadequate process conditions cause 45% failures in welded joints. [154]. Furthermore, because the study on the development of welding techniques has primarily been conducted to meet the industry's goals of demonstrating the great expertise of a process, many welding concepts have not been studied and hence are not comprehended [45]. This drawback implies that a significant amount of work is required to predict and optimise the laser welding process to produce constantly high-quality welds. Controlling the weld bead shape is critical for achieving an acceptable weld profile, and the weld bead attributes impact excellent mechanical qualities of the mechanical properties of welds. Welding settings and the associated quantity of heat input into the workpiece determine weld bead shape, which affects weld metal solidification behaviour [85]. As a result, the impact of welding input parameters [116, 157] on weld structure must be determined, and the origination of welding imperfections identified. The optimal combination of welding parameters that provide the desired weld quality and attributes while also minimising welding faults might then be identified [155,158].

AA 2024 components were welded under various welding conditions of peak power, scanning speed, frequency and pulse width. All the welds were autogenous, and argon was employed as the shielding gas. The quality criterion

discussed in **Table 5.6** was employed in the analysis of the micrographs. The main criterion assessed were weld width, penetration depth, undercut, humping and lack of penetration, along with cracks and pores. All the welds without penetration or cracks were rejected according to all the standards considered in this work. At low average power, the welds lacked penetration irrespective of the scanning speed. Also, there were porosity and cracks in the under-penetrated welds. Also, at low power, it was noticed that during the pulse-off time, the welding did not take place. This is due to the thermophysical properties of the material, which requires continuous high heat for its sufficient melting. However, by raising the laser power, a broader operating window was established [6], allowing a satisfactory weld quality to be produced by combining the laser power and welding speed suitably. As demonstrated in **Figure 5.7**, an input power of 2.5-4.5 kW and a low scanning speed of 1.0-2.0 m/min generated defect-free welds. However, the depth of penetration is significantly less. Raising the laser power over 4.5 kW at a specific welding speed resulted in widespread cracking in the weld due to strong keyhole effects, but reducing the laser power failed to adequately penetrate through the parent material.

Increasing welding speed with fixed laser power, in contrast, resulted in welding defects such as undercut and underfilled. The blue circle in Figure 5.8 indicates that a satisfactory weld quality can be attained with an optimised combination of laser power and welding speed. **Figure 5.9** shows the cracking started at the weld zone and extended through the depth. Welds similar to this have reduced strength and are not acceptable. Parameters such as focal position, weld pool shielding, and Acceptable filler metal choice have to be examined as well in order to avoid welding imperfections such as solidification cracking, grain boundary liquitation, and porosity, which were commonly encountered while welding crack-sensitive AA 2024-T. As a result, the effect of each parameter was explored and explained separately while the other parameters remained constant.

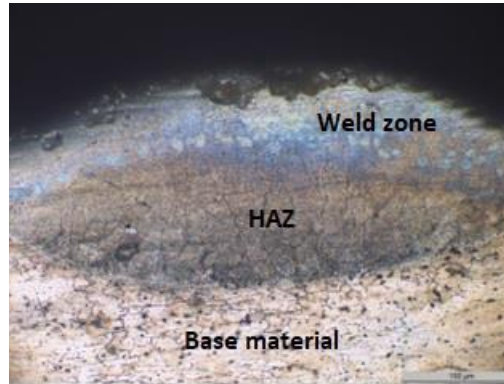


Figure 5.7 Image showing the weld zone along with heat affected zone and parent material at low power.

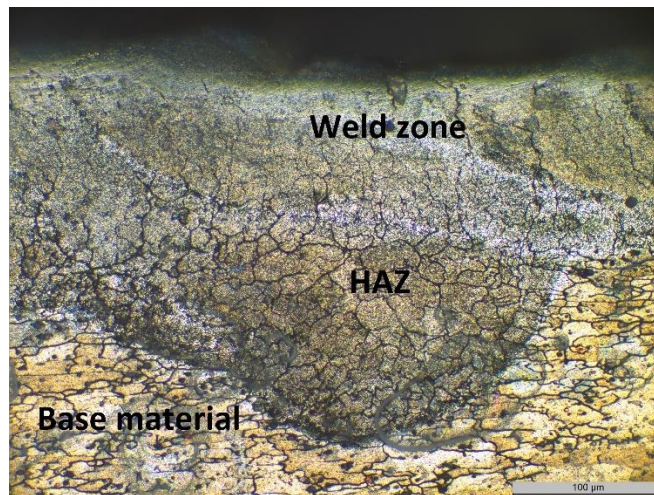


Figure 5.8 Image showing the weld zone along with heat affected zone and parent material at moderate power.



Figure 5.9 Image showing the weld zone along with heat affected zone and parent material at high power.

5.7 Prediction of weld metrics using the Gaussian process regression.

The composite model discussed in this article combines data from experiments, and FEA-based simulations, which are given as inputs to the ANN-based model. The experiments, finite element model, and ANN model all use identical inputs and outputs. This model assists in predicting the weld width and penetration depth, enabling the user to obtain the weld formation details.

5.7.1 Training process using Gaussian process regression

The neural network utilises an expensive class of supervised learning based on Gaussian processes. The advantages of this process are that it works even with a remarkably smaller number of parameters. It does not weigh the parameters leading to overfitting or generalisation; the training data determine the accuracy of the network's training. Even though laser welding is a complicated process, the effect of factors on output is visible, and the samples are distributed evenly. The training process employs the function '*C.predictFcn (T)*' to attain the fit data and respective curve. Here the data is supplied in a tabular column with the same predictor names as given in training data. The inputs are peak power, frequency, scanning speed and pulse width. The outputs are weld width and depth of penetration.

The architecture of the proposed gaussian process regression is given in **Figure 5.10**. The square boxes indicate the observed variables, whereas the circles are for the unknown variables. The horizontal line connecting all the circles represents the fully connected nodes. Here y_i is an observation independent of other nodes mentioned in the correlated latent variable f_i . Providing additional inputs x , latent variable f , and unobserved targets y does not change the distribution of other variables. This is due to the marginalisation property of GPR. The consistency is satisfied by the covariance function and its corresponding matrix.

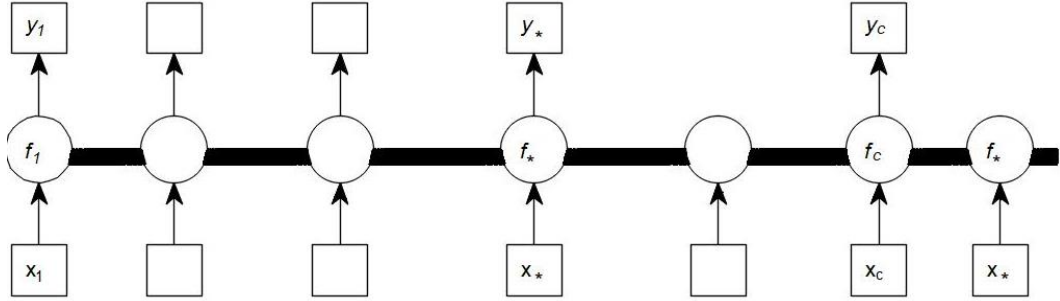


Figure 5.10 Architecture of the gaussian process regression model.

Gaussian process regression algorithm: The following is the sample algorithm for the process adopted in this work.

inputs

$:= x(\text{input}), (\text{target}), (\text{covariance function}), \delta_n^2(\text{noise level}), x_*(\text{test input})$

2: $L := \text{Cholesky}(k + \delta_n^2 I)$

3: $\alpha := L^T(L \setminus y)$

4: $\bar{f}_* := k_*^T \alpha$

5: $V := L \setminus k_*$

6: $\mathbb{V}_{f_*} := k(x_*, x_*) - V^T V$

7: *return* $:= \bar{f}_*(\text{mean}), \mathbb{V}[f_*](\text{variance})$

For multiple test cases, lines 4-6 are executed repeatedly.

5.7.2 Development of the GPR models

Various base kernel functions, called covariance functions, are employed in developing the GPR models. They are squared exponential (covSE), rational quadratic (covRQ) materniso 5/2 (CovMatern5), materniso 3/2 (covMatern3) and exponential covariance (covExp). While developing the model in GPR for predicting weld metrics in this work, all these covariance functions are assessed, and an optimum covariance function capable of predicting reliable weld width and depth of penetration is employed. A simple GPR constant mean function has yielded better results than zero and linear mean functions [155]. Hence this study employed a constant mean function to generate the model. The statistical parameters to evaluate the developed prediction model are the correlation

coefficient (R) and the root mean square error ($RMSE$). R examines the existence of a linear relationship between the predicted responses and the measured responses. $RMSE$ shows a difference between the predicted weld metrics and the measured responses. The mathematical equations for these two statistical parameters are given in equations 5.1 and 5.2. The entire model is coded in Matlab version R2020a

$$\text{Correlation coefficient } R = \frac{\sum_{i=1}^n (t_i - \bar{t}_i)(p_i - \bar{p}_i)}{\sqrt{\sum_{i=1}^n (t_i - \bar{t}_i)^2} * \sqrt{\sum_{i=1}^n (p_i - \bar{p}_i)^2}} \quad (5.1)$$

$$RMSE = \sqrt{\frac{1}{n} \sum_{i=1}^n (t_i - p_i)^2} \quad (5.2)$$

Here t denotes the measured value of the parameter, and p denotes the predicted value of the parameter, \bar{t} and \bar{p} represent the mean measured and predicted values, while n is the number of data sets [158]

5.8 Performance of the depth of penetration and weld width

The prediction results of the composite model developed by giving different covariance functions are given in **Table 5.10**. It is inferred from **Table 5.10** that the covExp performed the worst while CovMatern5 yielded good results. **Table 5.10** indicates the root mean square error and R squared values for different covariance functions applied to the present data.

Table 5.10 Different covariance and their performance in terms of error

Technique	CovSE	CovMatern5	CovExp	CovRQ
<i>RMSE</i>	11.52	10.779	11.825	10.882
<i>R-Squared</i>	0.89	0.98	0.89	0.90

The regression analysis between input data and predicted values for depth of penetration is depicted in **Figure 5.11**. Another set of welding parameters was

chosen randomly to assess the accuracy of network training. The input and output values were compared. R is the correlation coefficient between the target and predicted values, which is 0.99. The regression analysis findings reveal a strong correlation between the target and anticipated values. The data lying above the fit line are overfitting points, and those below the fit line are underfitting. The graph is to a depth of penetration of 2mm, which is the thickness of the material in experimental studies. Though a particular combination of input parameters gives a high average input power yielding a depth of penetration greater than 2mm, the study is limited to the experimental thickness.

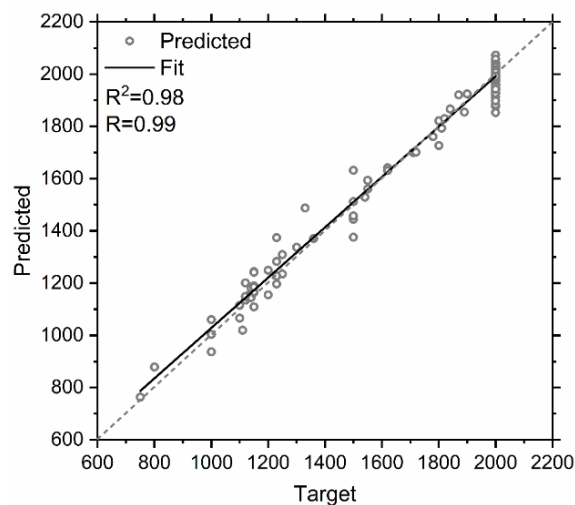


Figure 5.11 Analysis of regression between the target values and the predicted values for depth of penetration

Figure 5.12 shows the regression analysis between the empirical and predicted values for weld width. Here the correlation coefficient R is 0.9912, which indicates a strong correlation between the empirical and predicted values. Due to the spread of scattered points, the graph indicates that the proposed composite model is efficient at predicting the values at higher widths than at lower values.

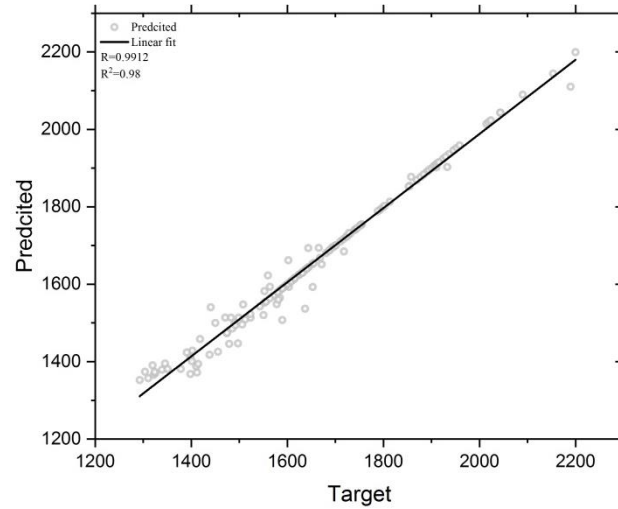


Figure 5.12 Analysis of regression between the target values and the predicted values for weld width.

This model has a mean absolute percentage error of 10^{-10} and a mean square error of 1.7, demonstrating the model's fidelity. This composite model can forecast weld depth of penetration for various combinations of input process parameters, allowing successful exploration of design space in less time while maintaining appropriate accuracy. The accuracy of this suggested model is determined by the data's dependability and the number of data sets utilised for training. The main issue in training the network arises from the accuracy of the acquired data and the number of data points. The higher the data sets, the more smoothed the training. Acquisition of the data sets is limited to the computational resources for simulating the proposed three-dimensional model and the cost involved in the experimentation. Also, the present model is designed to predict the parameters specific to the laser welding equipment employed in the experiment.

5.9 Implementation of the model

Table 5.11 indicates the error obtained from the proposed composite model compared to the simulation and experiment results.

Table 5.11 Error obtained from the proposed composite model.

S.No	P (kW)	V (mm/sec)	F (Hz)	PW (mS)	Input data		Composite model output		Error (%)	
					WW (μm)	DP (μm)	WW (μm)	DP (μm)	WW	DP
1	4	1	6	5	1357.46	750	1255.89	763.7	8	1.79
2	4.25	2	7	8	1615.23	2000	1655.42	2038.1	1.7	1.8
3	4.5	1.5	6	7	1755.21	2000	1725.36	2057.8	2.5	2.8
4	4.75	2.5	9	8	1957.55	1890	1919.5	1816.30	1.8	3

5.10 Summary

The design of experiments using response surface methodology gave 30 experiments. All the structured experiments are carried out on a 300W Nd: YAG laser welding machine.

The essential conclusions of the response surface methodology are

- The model proved adequate with acceptable values of the indicators like R^2 , *adjusted R^2* and *predicted R^2* .
- The p -values of weld width and depth of penetration are less than 0.05%, indicating that the model is statistically significant
- Scanning speed and frequency negatively impacted penetration depth, whereas higher peak power increased penetration depth.

The following are the salient conclusions from the predictive model:

- The average error between the outputs from experiments and CFD is around 4%. The data obtained from the experiments and simulation is worked using the Gaussian process, and the neural network is trained.
- The composite model evaluates the performance metrics, and the mean absolute percentage error is 10^{-7} . The mean square error from the proposed composite model is 1.7. The results indicate that the proposed model has the highest accuracy compared to the results from the simulation.
- The process is better suited for real-time quality decisions related to the depth of penetration and weld width, avoiding additional experimentation.

- Though the present work depicts the ability to create a composite model, it is limited in its applicability. The selected process parameters are related to the laser-pulsed welding machine. The input parameters range specific to the target material, aluminium alloy 2024.

Chapter 6: Formation of defects and simulation of humping during laser welding of Aluminium alloy 2024

6.1 Introduction

This chapter gives a thorough insight into the various defects that occur when AA2024 samples are welded using the laser beam. Various defects like cracks and pores, undercut, underfill, lack of penetration and humping occur during the welding of this alloy.

6.2 Defects on the welded samples

The butt-welded samples are examined under the metallurgical and scanning electron microscopes for the microstructure and defects. The following attributes are noticed during the investigation.

6.2.1 Hot cracking

Aluminium, in its pure form, is not sensitive to hot cracks. This is due to the unavailability of a lower melting point eutectic at the grain's boundary. But when added elements like Cu, Si and Mg make pure aluminium an alloy with the designation 2024, it is highly susceptible to cracking. These components render poor weldability due to the higher amount of solute, which renders a wider solidification temperature range and a higher inclination towards forming low melting point elements along the grain's boundary. These low melting point constituents occur due to the large coefficient of thermal expansion and a higher rate of solidification shrinkage. Hot cracking, also called solidification cracking, takes place predominantly alongside the welded grain's boundary at the time of solidification. The stresses along the boundary segregate the elements with lower melting point [58]. Generally, aluminium alloys are not susceptible to cold cracking [111]. Cao et al. [22] explained various theories, including the brittle temperature range theory and critical speed theory, to explain the cracking mechanism. Because of the existence of alloying elements, the 2024 alloy has a range of freezing temperatures, such that the solidification strains are proportional to the temperature interval over which solidification occurs. The

temperature range where the mushy zone occurs between the interlocking of dendrites and the solidus temperature; and mechanical properties of the alloy in the specified temperature limits help in the cracking of the weld zone. Rapid non-equilibrium solidification during welding lowers the effective solidus temperatures. At the time of solidification, the areas which have freezing zones, from the weld boundary to the weld centerline, solidify first. According to the theory of concentration of liquid film strain, the cracks form because the liquid films are unable to endure the thermal shrinkage that develops when the material solidifies. The supply of the residual eutectic liquid available to fill the crack is insufficient during shrinkage. The hot cracking phenomenon in AA 2024 is controlled by optimising the welding parameters and avoiding the crack-sensitive composition of the weld zone by using a filler rod [112]. Fine and equiaxed dendritic structures with sufficient liquid grains increase the resistance to solidification cracking. This increased resistance is due to the reduction in the mushy temperature range. Higher average available power reduces the strains caused due to the thermal history of the components and produces finer grain structure. This structure relieves local shrinkage stress [109, 159, 160]. **Figures 6.1** and **6.2** depict the crack that occurred along the fusion and heat-affected zones. It is noticed from **Figure 6.1** that the crack did not extend beyond HAZ, whereas it is spread throughout the depth of penetration in **Figure 6.2**.

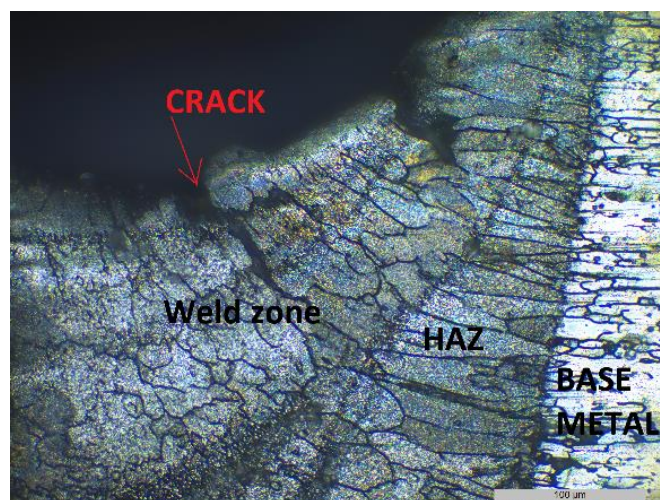


Figure 6.1 Crack present in the weld zone extending to the heat-affected zone.

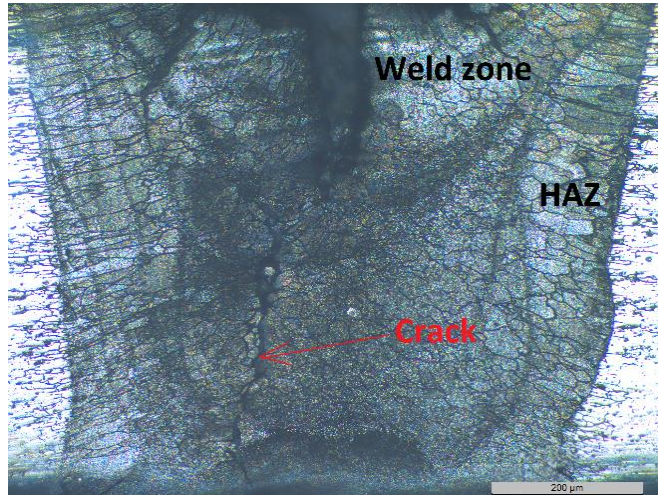


Figure 6.2 Solidification crack propagating in the heat-affected zone.

6.2.2 Porosity

Micro-pores are detrimental to the satisfactory working of the welded joints [45]. The traditional welding of AA2024 produces micro pores making the welded unsuitable for employing it in various applications. Hence, laser welding is chosen as an option. Though the impact of pores is lesser than that of cracking, the stringent aircraft norms reject the components during the quality check as they act as stress concentration zones. But in the selected window, pores were not noticed in the welded samples.

6.2.3 Softening of fusion zone

The dissolution of the precipitates results in the softening of the fusion zone. This effect is more dominant in the fusion zone than in the heat-affected zone due to the high dissolution of the strengthening phases at high temperatures [31, 128]. The fast-welding speed and high thermal gradients at the FZ boundary led to an elongated weld pool, promoting columnar dendritic structures in **Figure 6.3**. As can be seen from **Figure 6.4**, the FZ showed the formation of characteristic equiaxed dendrites and a typical honeycomb structure. The figure is captured at a magnification of 250x. Continuous epitaxial growth of columnar dendrites was observed in the direction of thermal gradients in the FZ, with the same crystallographic orientation as that at the FZ line. The dendrite cells' size

depended on the heat input, laser power and welding speed, which were responsible for the temperature gradient and solidification rate.

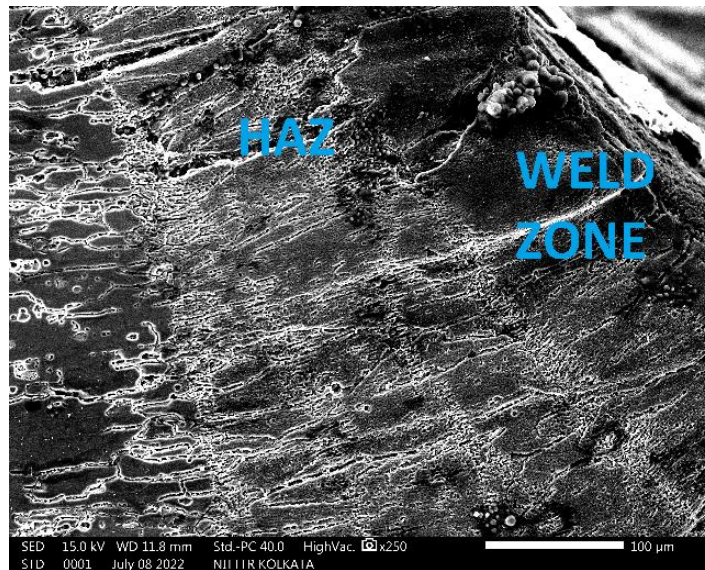


Figure 6.3 Columnar dendritic structure at high scanning speed.

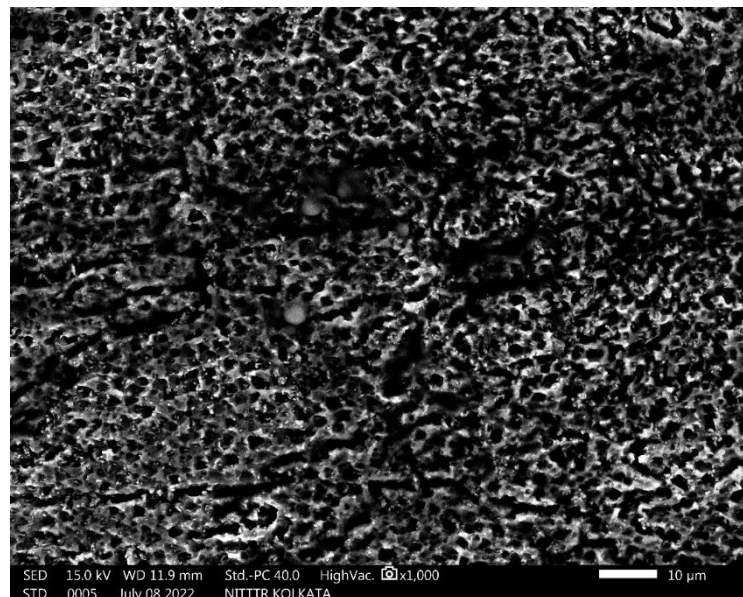


Figure 6.4 Honeycomb structure in the fusion zone.

6.2.4 Undercut

Figure 6.5 shows the undercut formed during welding at the highest power. The measured depth of the undercut is 0.6mm. It exceeded the maximum depth specified in AWS D17.1 of 0.05 mm and 0.15 mm in BS EN ISO 13919-2 and

BS EN 4678. As a result of the higher peak power, an undercut occurred, which failed the acceptance criterion of the weld. This undercut is due to a higher quantity of base material being melted and evaporated, leading to a spatter. Thus, the undercut was not backfilled properly during solidification.



Figure 6.5 Undercut seen on the welded sample at a peak power of 4.75kW.

6.2.5 Loss of alloying elements

The loss of alloying components such as magnesium, which has a low boiling point of 1091°C and a high equilibrium vapour pressure, was detected in the transverse cross-section of the weld using energy dispersive spectroscopy (EDX). These components are vaporised into the surrounding gas phases at the weld pool's surface [161].

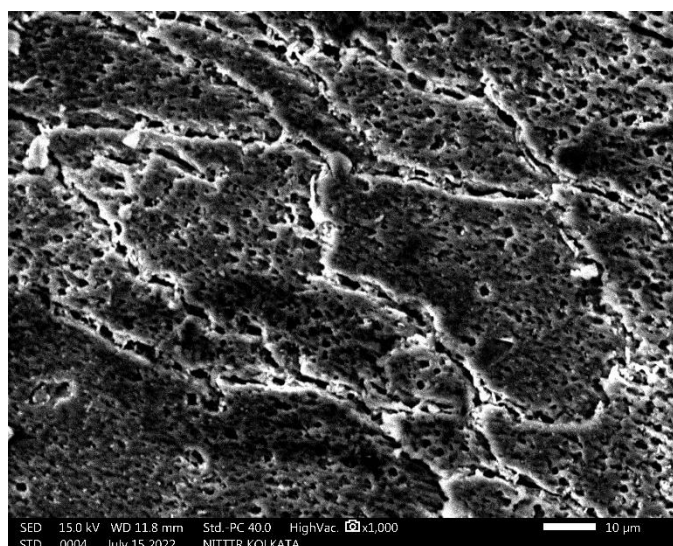


Figure 6.6 Scanning electron microscope image showing the composition.

Figure 6.6 depicts the EDX spectrum of the fusion zone as obtained by scanning electron microscopes (SEM), as well as the chemical composition of the parent material and welds generated at moderate power density. The shining boundary along the grains indicates magnesium content. Compared to the parent material

(PM), welds had an average loss in magnesium content of roughly 0.5%, ranging from 1.2 to 0.7%, but only a slight variation in power density was noted. The weld's low Mg content caused keyhole instability, which enhanced the danger of hot crack susceptibility [128, 161, 162, 163]. By adjusting the molten metal temperature in the weld pool, a change in power density was assumed to impact the magnitude of alloying element losses. However, the difference was relatively minor because the minimum heat inputs used in these specimens were similar. Nonetheless, welding parameters such as speed can be used to manage the vaporisation rate and the weld pool's volume.

6.2.6 Humping

Humping occurred at all powers ranging from the lowest peak power of 4kW to 4.75kW at a speed of 2.2 mm/s. **Figure 6.7** shows the hump formed at the average speed of 4.5kW. But below the scanning speed of 2.2mm/s, though humping was present, its dimension was not significant, as shown in **Figure 6.8**.

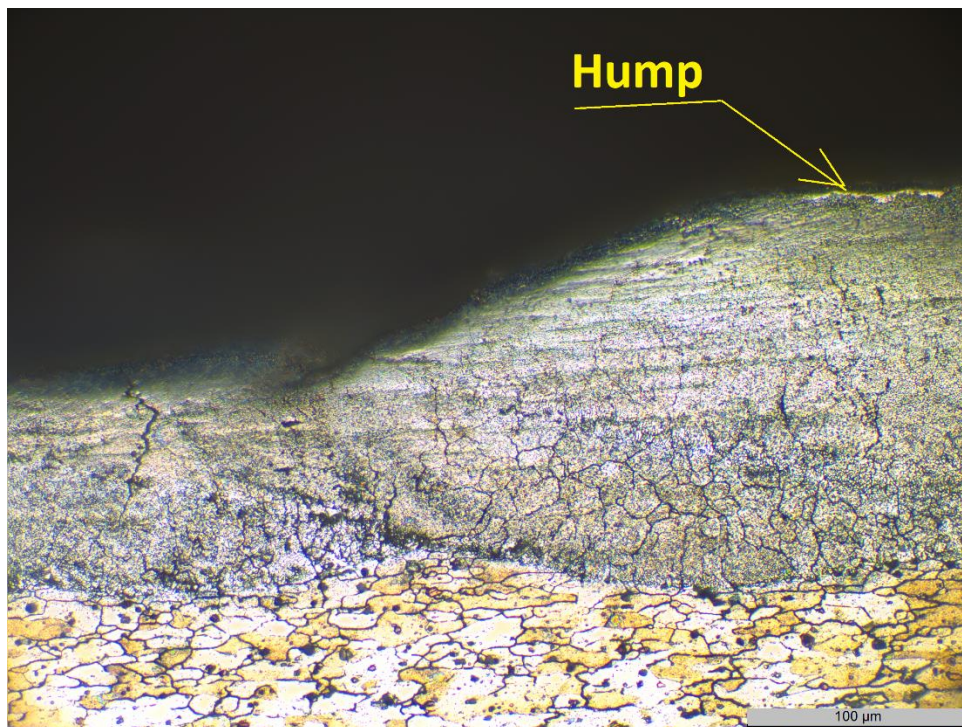


Figure 6.7 Hump formed at a peak power of 4.5kW.

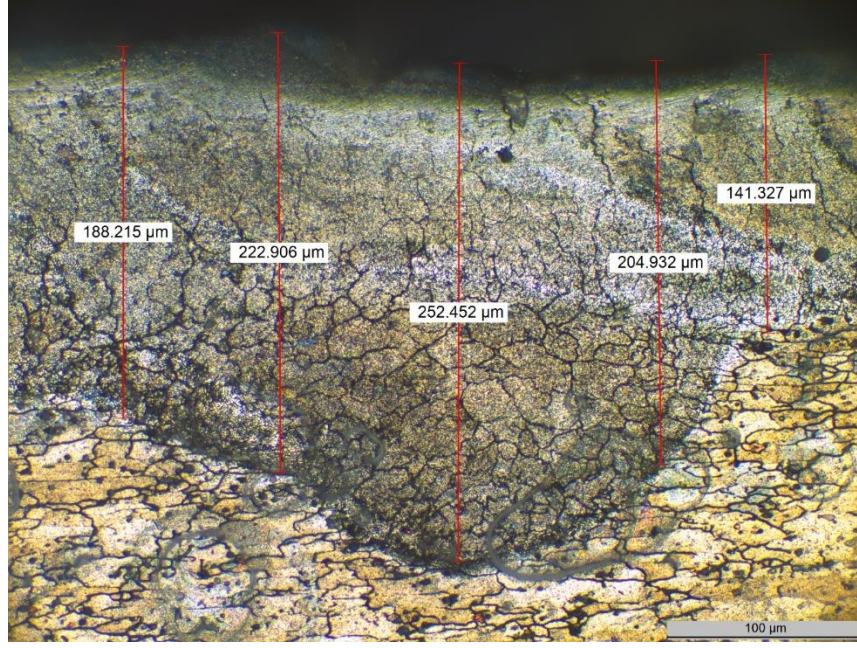


Figure 6.8 Hump formed at a peak power of 4kW and 1.4 mm/s

6.3 Numerical model of humping formation in laser welding of AA2024

6.3.1 Proposed Thermo-Fluid model

In the present section, a transient thermal and fluid 3D model is proposed to study the temperature history during the laser spot welding of AA2024. The laser beam impinges on the plate at a spot with small pulses till the heating time is complete. A frequency of 1Hz is considered in this work to study the thermal and fluid dynamics for one single pulse. This work aims to study the effect of one pulse on the formation of the hump.

6.3.2 Development of the model

The simulation is governed by the conservation of mass, momentum and energy equations (6.1), (6.2) and (6.3) to assess the time-temperature history and characteristics of the molten pool.

$$\nabla \cdot (\rho \mathbf{u}) = 0 \quad (6.1)$$

$$\rho \frac{\delta \mathbf{u}}{\delta t} + \rho (\mathbf{u} \cdot \nabla) \mathbf{u} = \nabla \cdot \left[-p \mathbf{I} + \mu (\nabla \mathbf{u} + (\nabla \mathbf{u})^T) - \frac{2}{3} \mathbf{u} (\nabla \cdot \mathbf{u}) \mathbf{I} \right] + K \mathbf{u} \quad (6.2)$$

$$\rho C_p^* u \cdot \nabla T = \nabla \cdot (\lambda \nabla T) \quad (6.3)$$

where ρ is the density of the molten material, u represents the velocity vector, μ is the fluid's viscosity, and p is the pressure of the liquid. K is the drag coefficient in the mushy zone given by equation (6.4),

$$K = \frac{C_1(1-f_l)^2}{f_l^2 + C_2} (u - u_{weld}) \quad (6.4)$$

C_1 is the constant operator to explain the conditions of the mushy region. f_l is the liquid fraction indicating frictional dissipation in the mushy zone, and C_2 is the positive number taken to avoid division by zero. The solidus-liquidus mushy zone is modelled based on the energy-temperature relationship [147] in equation (6.5). It is defined as:

$$f_l = \begin{cases} 0 & 0 < T < T_s \\ \frac{T-T_s}{T_s-T_l} & T_s \leq T \leq T_l \\ 1 & T \geq T_l \end{cases} \quad (6.5)$$

f_l is the liquid fraction for frictional dissipation in the mushy zone. It changes between 0 and 1 from solidus to liquidus temperatures. For the solid phase, $f_l = 0$, and when liquid is present, $f_l = 1$. For the target material, the solidus (T_s) and liquidus (T_l) temperatures are considered as 847 K and 933 K, respectively. The temperature in the fusion zone exceeds the material's melting point during the welding process. Hence, a phase change phenomenon by the enthalpy method defined in equation (6.6) is included in finite element simulation [147].

$$C_p^* = C_p + \frac{\exp\left(\frac{(T-T_{melt})^2}{\delta T}\right)}{\sqrt{\pi} \delta T} H_f \quad (6.6)$$

where, H_f = the latent heat of fusion and δT = the temperature range of the mushy zone. C_p = Specific heat capacity, C_p^* = apparent specific heat, which defines the melting phase.

Marangoni convection is applied at the top surface using equation (6.7). Here γ is the temperature-derived surface tension.

$$\gamma = \gamma_m + \left(\frac{\partial \delta}{\partial T} \right) (T - T_m) \quad (6.7)$$

6.3.3 Laser parameters

When laser light is incident on the surface, the energy-carrying photons transfer it to the colliding surfaces. This energy transfer depends on factors such as wavelength, reflectivity and absorptivity of the material and pulse width of the incident laser. The pulse width is the critical factor that defines the thermal energy transfer among these factors. In the present work, a millisecond pulsed laser is the heat source and follows a Gaussian distribution. A rectangular profile defines the constant rise and decay of the pulse. The beam diameter is 0.6mm, and the heat source is defined by the volumetric heat source given in equation (8)

$$Q_0 = \frac{3AP}{\pi r_b^2 h} \exp \frac{-3(x-x_c)^2}{r_b^2} \exp \frac{-3(y-y_c)^2}{r_b^2} \exp \frac{-3(z-z_c)^2}{h^2} \quad (6.8)$$

6.3.4 Numerical model

Three different phases of heat transfer take place during spot welding. Heat transfer in fluids and the fluid flow module are used to track the different phenomena occurring in the process. The molten metal is considered to be laminar. Before attaining the vapourisation point, surface tension, gravity and buoyancy forces acting on the molten metal. The surface tension is defined as a weak constraint on the top surface. This constraint depends on the tangential velocity of the molten metal. The vapourisation starts at a temperature of 2520K. Once vapourisation is attained, recoil pressure given in equation (9) comes into action at the liquid-vapour boundary.

$$R_p = 0.54 P_a \exp \left(\frac{L_v(T-T_v)}{RT T_v} \right) f_r \quad (6.9)$$

Here P_a is the atmospheric pressure (atm), L_v is the latent heat of vapourisation (J/Kg), T_v is the vapourisation temperature(K), R is the universal gas constant ($\text{kg}\cdot\text{m}^2\cdot\text{s}^{-2}\cdot\text{K}^{-1}\cdot\text{mol}^{-1}$), f_r is the spatial distribution that ensures that recoil pressure acts within the irradiated area. The recoil pressure gets activated only

in the regions where the temperature reaches vapourisation temperature. It is defined as an open boundary condition and exerts a download force perpendicular to the vapour-liquid interface. Matsunawa [70] termed a keyhole in terms of a balance of force between the surface tension of liquid encapsulating the vapour plume and recoil pressure. In the present work, the humping phenomenon is modelled using Arbitrary Lagrangian – Euler method. It is a feature for modelling moving boundaries in continuously deforming geometries. The entire domain experiences repetitive pulse heating at every time step.

6.3.5 Mesh

A triangular swept mesh with a total of 7660 elements is used to mesh the components, as shown in **Figure 6.9**. The beam irradiation site is meshed finely, and the rest of the component is meshed coarsely to ease the computation.

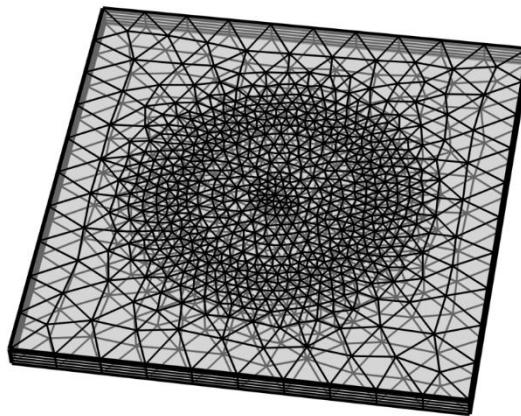


Figure 6.9 Meshed component

6.3.6. Results and discussions

To study the humping formation in ultra-thin sheets of aluminium alloy 2024, the process parameters employed for generating **Figure 6.9** and **Figure. 6.10** are peak power of 3kW, a pulse width of 5ms and a frequency of 1Hz.

Temperature distribution and evolution of the hump

The temperature distribution at various time steps during laser spot welding is shown in **Figure 6.10 (a-d)**. The temperature increased from 1969K at 0.8ms to 2064K at 1.4ms. It is observed from the above figure that the humping started at

around 0.8ms. It increased till the completion of the heating process, as shown in **Figure. 6.10 (c)**. Later the liquidus part solidifies, forming the hump. So, the temperature in **Figure. 6.10 (c)** is higher than in **Figure. 6.10(d)**, but the hump is larger than the previous time step. In subsequent time steps, the hump remained at the height as in **Figure.6.10 (d)**, which indicates the onset of solidification once the pulse turns off.

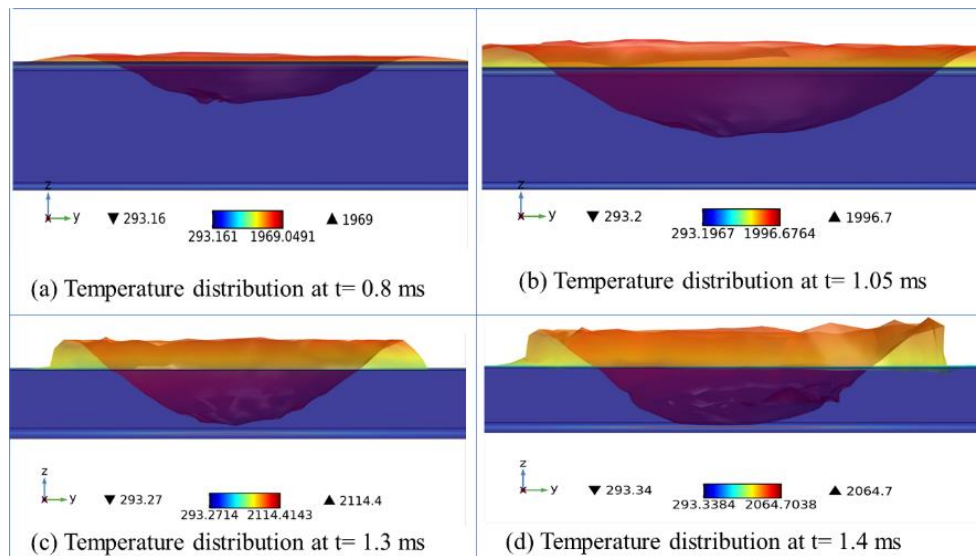


Figure 6.10 Temperature distribution in the components at different time steps.

Fluid flow and velocity of molten metal in hump formation

During the welding process, the molten metal in the front wall of the keyhole generally flows downward [15]. The greatest speed attained in this simulation is 1.0691 m/s. When this downward-flowing molten metal reaches the bottom of the keyhole, the metal's movement is stopped by the yet-to-melt solid beneath the bottom of the keyhole. Hence it moves to the rear part, and no hump is formed. This process is depicted in **Figure. 6.11 (a)**, where there is no hump.

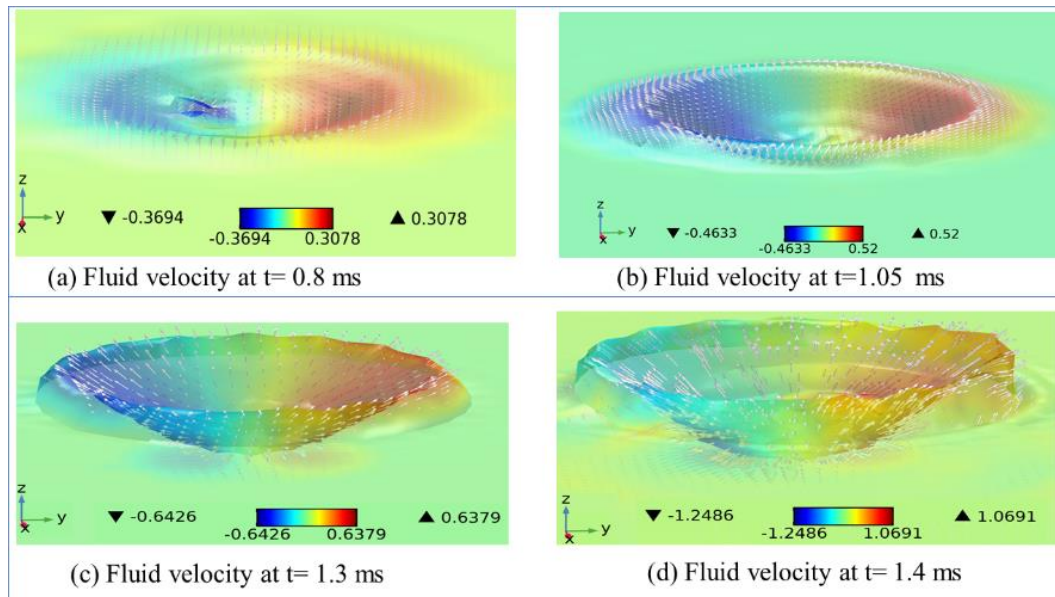


Figure 6.11 Fluid velocity in the components at different time steps

Subsequently, in **Figure 6.11 (b-d)**, as the melting continues, the molten fluid reaches the bottom part of the keyhole. Here, forces like surface tension and buoyancy come into play and slowly increase the penetration depth. There is an expansion of the molten metal in the opening of the keyhole. The metallic vapour rises upwards, and the back portion of the keyhole gets closed. This process initiates humping. The forces like recoil pressure and action of gravitation enhance the formation of humping. Surface tension and speed with which the molten metal solidifies are responsible for the size of the hump. The conditions influencing the humping formation on the surface and the root hump at the bottom are similar. With the rising peak power, the simulation shows the root hump and the hump on the surface.

The fluid velocity at different time steps is shown in **Figure 6.11**. According to **Figure 6.11**, the height of the hump is more at later time steps where the fluid velocity is also higher, as discussed in reference. At 0.8ms the fluid velocity is 0.3078 mm/s which increased to 1.0691m/s at 1.4 ms. High surface tension is obtained in places where the temperature is high. This higher surface tension is the reason for the inward flow of the material. It produces a

keyhole in the welds that pushes more material towards the surface resulting in larger humps. **Figure 6.12** shows the flow field and the distribution of fluid that results in the arrows and the flow direction.

Root humping: The principal driving forces that lead to the formation of root hump are recoil pressure draws the fluid down at high speed; surface tension pulling the molten metal back to the weld pool and acting opposite to the recoil pressure; gravitational force, which resists the action of surface tension on the molten metal and aids in the formation of root hump along with recoil pressure. **Figure. 6.13** shows the humping in the surface and the root hump that formed at high peak power of 4kW and 5ms.

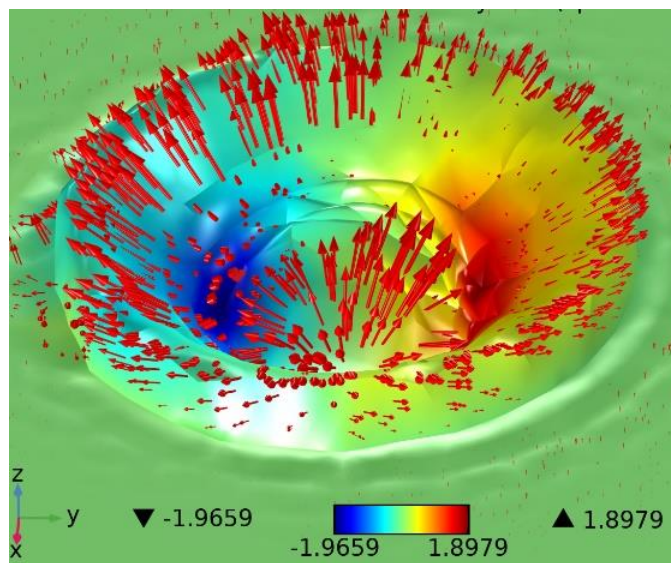


Figure 6.0.12 Flow field and fluid distribution.

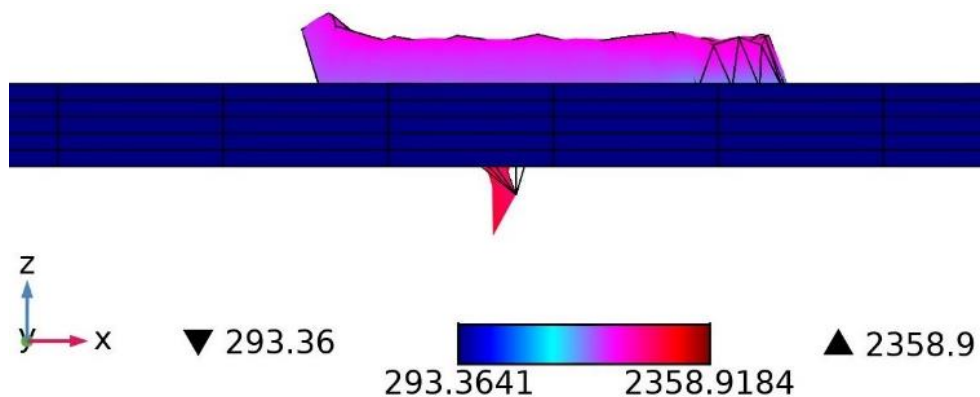


Figure 6.13 Hump and root drop

To assess the influence of peak power on the formation of humping

The peak power is increased in steps from 0.5 to 4 kW. At low powers, less than 1 kW, no humping is noticed, and it increases steeply after that, as shown in **Figure 6.14(a)**. The increase in peak power melts more metal which increases the Marangoni forces. Hence, the molten pool rises higher on the surface and solidifies, leading to humping. The peak power increases the velocity in the molten pool, which helps recirculate the fluid. This fluid gets solidified on the surface of the component, and it stays as a hump. **Figure 6.14 (b)** shows the velocity variation with peak power. The availability of higher radiation at high peak power values has given fluid a velocity as high as 134.12m/s at 4kW.

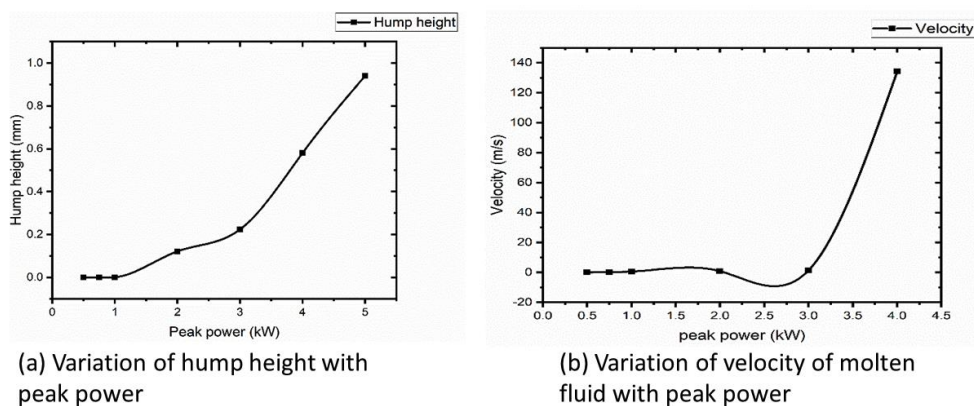
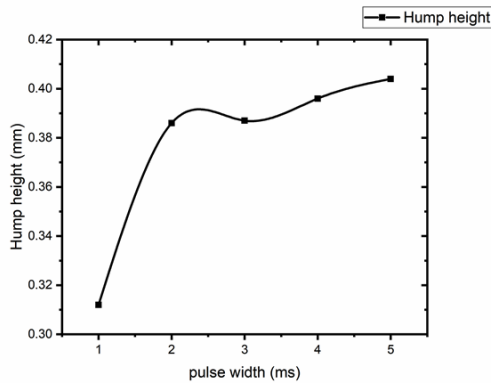


Figure 6.14 The hump height and molten pool velocity variation with peak power. (a) Variation of hump height with peak power. (b) Variation of velocity with peak power.

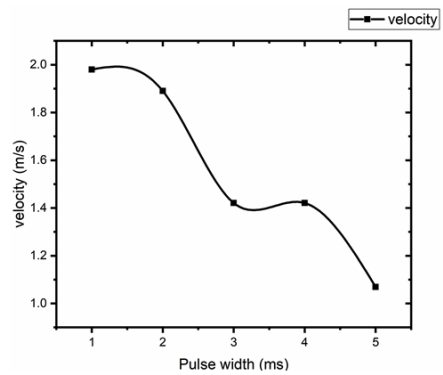
To assess the influence of pulse width on the formation of humping

The variation of hump height with pulse width is shown in **Figure. 6.15(a)**. It is inferred from the graph that the increase in pulse width raised the hump height. The peak power lowers and the pulse overlapping factor increases with a rise in pulse width. A nearly continuous weld seam ensues the subsequently overlapping pulses [3]. But this study is made for a frequency of 1Hz (i.e. for

one pulse of the laser). The velocity of the fluid decreased from 1.89 at 1ms to 1.06 at 5 ms. However, the velocity is reduced, and humping is formed due to the movement of the fluid. The values are drawn for a peak power of 3Kw. From **Figure 6.15(b)**, the velocity increases with the pulse width, but the rise is negligible.



(a) Variation of hump height with pulse width



(b) Variation of molten pool velocity with pulse width

Figure 6. 15 Variation in hump height and molten pool velocity with pulse width. (a) Variation of hump height with pulse width. (b) Variation of velocity with pulse width.

The evolution of the hump with pulse width is shown in **Figure 6.16**. It depicts the decreasing trend in the fluid velocity and the increasing hump height. Here the velocity as low as 0.845 at 1kW and 5ms also yielded a hump. Hence, though pulse width at a frequency of 1Hz is not an influencing factor, a rise in pulse width increases the humping formation.

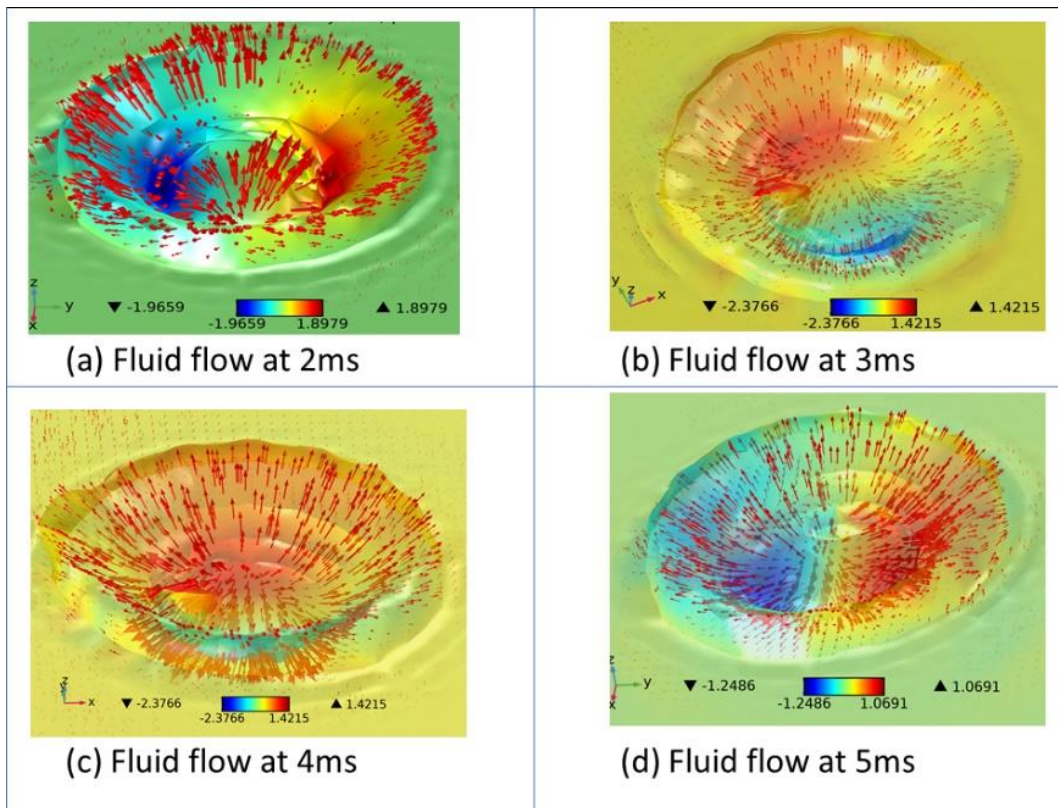


Figure 6.16 Evolution of humping with pulse width. (a) Fluid flow pattern at 2 ms. (b) Fluid flow pattern at 3 ms. (c) Fluid flow pattern at 4 ms. (d) Fluid flow pattern at 5 ms.

6.4. Summary

This chapter studies the welding defects that occurred during the laser welding of aluminium alloy 2024. The simulation is a microcosm of the hump formation in the welded joint, which studies the impact of a single pulse on the humping formation.

The simulation uses 0.5kW to 4kW peak power and 1-5ms pulse width. The molten pool dynamics are analysed by drawing the temperature distribution and fluid flow figures.

Based on the numerical simulation, the following conclusions can be summarised:

- The rise in peak power increases the hump height when the pulse width and frequency are maintained as constants

- The rise in pulse width has enhanced the humping formation at any constant peak power and frequency
- The velocity of the molten fluid is the influencing factor in the height of the hump, and pulse width has shown a negligible effect on the hump height at a frequency of 1Hz.

Chapter 7: Optimization of process parameters of laser welding of AA 2024

7.1 Problem Statement and Methodology

This chapter deals exclusively with the optimization of welded joints that were welded using laser beam welding. The quality of the welded joints is determined by the surface appearance, presence of defects and mechanical measurements. Of all the criteria, the first and basic one is surface appearance. The weld width is seen on the top surface, and the depth is at the bottom. The weld bead and the heat-affected zone are the major deciding factors on the top surface. The minimum weld width is more appealing and is always preferred. The depth of penetration should be maximum to have a sound joint. This chapter tries to optimize the input process parameters in the selected range with the objective of getting minimum weld width and a maximum depth of penetration. Particle swarm optimization is employed to optimise and attain desired results.

7.2 Process parameters and ranges

There are four parameters in this system. They are peak power scanning, speed frequency and pulse width. The units and ranges of the parameters are given in

Table 7.1

Table 7.1 Process parameters and ranges

Parameters	Units	Limits				
Peak Power	kW	4.00	4.25	4.50	4.75	5.00
Scanning Speed	mm/s	1.0	1.4	1.8	2.2	2.6
Frequency	Hz	6	7	8	9	10
Pulse Width	Ms	5	6	7	8	9

7.3 Objective functions

The objective of the work is to obtain a solution that gives a maximum depth of penetration and minimum weld width. The total depth of penetration occurs at high heat input to the joint. When combined with low scanning speed in a high-duty cycle in the case of pulsed mode laser welding, this heat input gives a

keyhole resulting in good bond strength. However, the high heat accumulated in the joint also gives a high weld width and a more comprehensive heat-affected zone. It is not desirable to have wider HAZ and weld width. They weaken the joint, and the appearance of the joint becomes poor. So, while getting full penetration, the objective is to obtain lesser weld width. The objectives are maximum depth of penetration and nominal or minimum weld width. Two objectives are conflicting, necessitating a compromise between their responses.

7.4 Results of the optimization

The optimizations were carried out exhaustively for an archive size of 700 and a maximum of 100 generations. The convergence was observed at the 345th run. Though the values of weld width and penetration depth change under the variables' range, their change appears to have a regular pattern. The optimization was also run for different archive sizes. However, beyond an archive size of 700, the optimization did not run, indicating that the archive size of 700 is the maximum size that can be used for this particular application. When the penetration depth was maximum, the weld width was minimal. However, a weld width of 1mm is the minimum possible value indicating that the objective value is at nominal the best. The Pareto front of the two objectives is obtained, as shown in **Figure 7.1**. The significance of this algorithm lies in the usage of the crowding distance parameter. The crowding distance is generally used in genetic algorithms. It is calculated by sorting the solutions in the increasing values of the objective functions. The value of the crowding distance of any solution is the average distance of the two solutions that are neighbours. In the present algorithm, the crowding distance and mutation operator are defined in PSO, along with the deletion of the external archive of the nondominated solutions. This process helps maintain the diversity of the nondominated solutions maintained in the external archive. The convergence is competitive, and the Pareto front gives a highly distributed set of nondominated solutions.

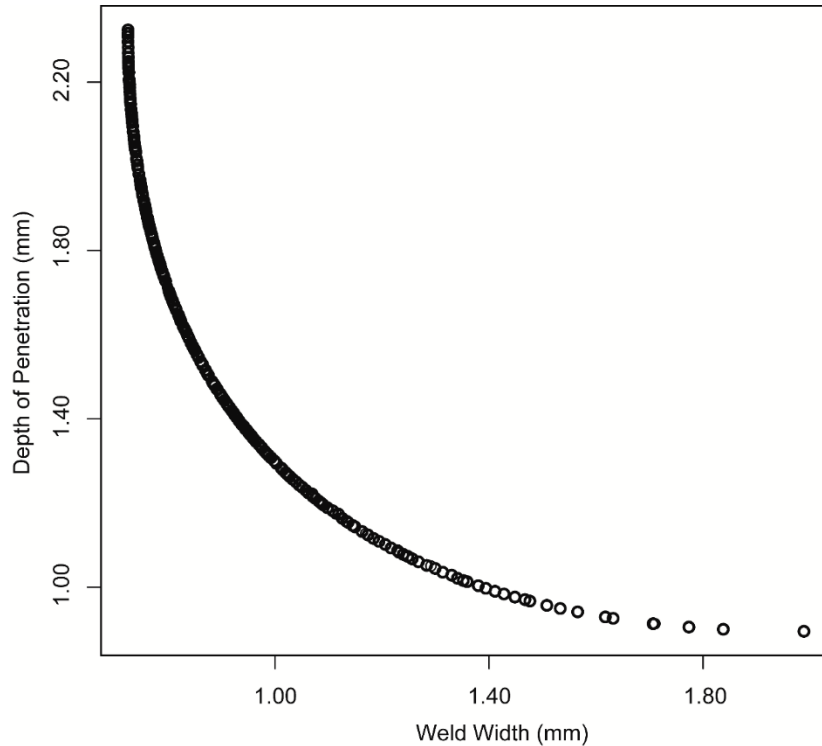


Figure 7.1 Pareto graph between weld width and depth of penetration

7.5 Time Complexity of the Algorithms

The current work takes into account two objectives and four constraints. Here, the crowding distance is calculated, and subsequently, the non-dominated solution is attained by comparing it with the archived solution. The complexity of the optimization algorithm is calculated by following the big ‘*O*’ notation. The computational time consumed by the present problem is 1.6293 seconds, wherein most of the time is spent sorting the archived solutions. Considering ‘*N*’ solutions in the archive for *F* objective functions with a swarm size ‘*S*’, the complexity is $O(F \times S \times \text{Log } N)$, as mentioned in [164].

7.6 Summary

A multi-objective optimisation corresponding to the welded joint is performed with PSO (crowding distance). This study has two objectives: minimisation of the weld width and maximisation of the depth of penetration of the weld. The two objectives are significant in deciding the surface attributes of the welded components. The higher the weld width, the more damaged the parent material,

and the strength decrease. Hence, a minimum weld width is desirable. The depth of penetration needs to be maximum to attain a good bonding between the two components. The crowding distance variant of the algorithm calculated the weld metrics in 1.6293 seconds. The mutation operator increased the exploring capacity of the swarm and protected it from premature convergence.

7.7 Parameter values to obtain the optimized value

Table 7.2 Values to obtain the optimized value

S.NO	Peak power	Scanning speed	Frequency	Pulse width
[1]	4.413705	1.000008	9.999999	8.999998
[2]	4.152337	1.00001	9.999997	8.999999
[3]	4.395897	1.000004	9.999999	8.999991
[4]	4.385788	1.000022	9.999995	8.999995
[5]	4.352215	1.000016	9.999995	8.999978
[6]	4.384208	1.000024	9.999998	8.999994
[7]	4.200544	1.000013	9.999998	8.999988
[8]	4.412284	1.000004	9.999997	8.999992
[9]	4.397172	1	9.999998	9
[10]	4.323441	1.000021	9.999997	8.999991
[11]	4.409886	1.000016	9.999997	8.999989
[12]	4.321321	1.000026	10	8.999998
[13]	4.411122	1.000006	10	8.999992
[14]	4.338843	1	9.999996	8.999992
[15]	4.340425	1.000012	9.999996	8.999998
[16]	4.207928	1	9.999996	9
[17]	4.345544	1.000015	9.999996	8.999997
[18]	4.291119	1.000018	9.999997	8.999991
[19]	4.360248	1.000004	9.999996	8.999984
[20]	4.327948	1.000016	9.999998	8.999993
[21]	4.37561	1.000022	9.999996	8.999985
[22]	4.266556	1.000012	9.999997	8.999993
[23]	4.408725	1	10	9
[24]	4.354896	1.000009	9.999998	9
[25]	4.39485	1.000017	9.999996	8.999979
[26]	4.400992	1.000005	9.999999	9
[27]	4.375024	1.000018	9.999996	8.999997
[28]	4.329236	1.000006	9.999996	8.999964
[29]	4.342478	1.000016	9.999997	8.999974
[30]	4.377856	1.00002	9.999997	8.999985
[31]	4.330146	1	9.999997	8.999959
[32]	4.398455	1.000027	9.999999	9

[33]	4.252426	1.000084	10	9
[34]	4.259817	1.000011	9.999996	8.999995
[35]	4.235354	1.000009	10	8.999982
[36]	4.22556	1	10	8.999991
[37]	4.399337	1.000011	9.999999	8.99999
[38]	4.337157	1.000026	9.999992	8.999982
[39]	4.192263	1.000006	9.999998	8.999999
[40]	4.392893	1.000019	9.999997	8.999987
[41]	4.256156	1	9.999998	9
[42]	4.366245	1.000009	9.999995	8.999986
[43]	4.204684	1.000004	9.999997	9
[44]	4.242333	1.000015	9.999998	8.999996
[45]	4.237608	1.000027	9.999994	8.999914
[46]	4.194049	1.000007	9.999998	8.999998
[47]	4.362783	1	9.999996	8.999964
[48]	4.41294	1.000033	9.999999	8.999997
[49]	4.299939	1.000004	9.999997	8.999992
[50]	4.250568	1.000007	9.999997	8.999991
[51]	4.371768	1.000006	9.999999	8.999998
[52]	4.383693	1.000019	9.999996	8.999989
[53]	4.376861	1.000002	9.999998	8.999992
[54]	4.369357	1.000025	9.999998	8.999993
[55]	4.343833	1.000005	9.999994	8.999993
[56]	4.270022	1	9.999998	8.999854
[57]	4.336082	1.000001	10	8.999964
[58]	4.314904	1.00001	9.999997	8.99999
[59]	4.331391	1.000025	9.999995	8.999986
[60]	4.289284	1	9.999995	8.999967
[61]	4.308828	1.000025	9.999996	8.999974
[62]	4.271696	1.000021	9.999997	8.99999
[63]	4.355823	1.000009	9.999999	8.999987
[64]	4.254398	1.000004	9.999995	8.999984
[65]	4.262202	1.000005	9.999997	8.999975
[66]	4.23293	1.000024	10	8.999876
[67]	4.298563	1.000017	9.999996	8.999965
[68]	4.292146	1	10	8.999897
[69]	4.347708	1	10	9
[70]	4.344295	1.000015	9.999994	8.99998
[71]	4.621216	1.000013	9.999996	8.999998
[72]	4.392043	1.000015	9.999998	8.999993
[73]	4.370836	1.000011	9.999998	8.999996
[74]	4.218746	1.000011	9.999997	8.999992
[75]	4.283398	1.000018	9.999997	8.999988
[76]	4.405811	1.000089	9.999997	9
[77]	4.397805	1	10	8.999994

[78]	4.361194	1.000017	9.999999	8.999992
[79]	4.311236	1.000011	9.999996	8.999977
[80]	4.215953	1.000017	9.999996	8.999992
[81]	4.401595	1.000018	9.999996	8.999988
[82]	4.381959	1.000002	9.999999	8.999993
[83]	4.279677	1.000007	9.999995	8.999997
[84]	4.532005	1.000013	9.999997	9
[85]	4.175637	1.00001	9.999997	8.999996
[86]	4.393601	1	10	8.999991
[87]	4.353413	1.000016	9.999998	8.999989
[88]	4.394131	1.000079	9.999998	9
[89]	4.380432	1.000007	9.999997	9
[90]	4.315883	1.000022	9.999997	8.999989
[91]	4.386404	1.000008	9.999997	8.999989
[92]	4.284693	1	10	8.999985
[93]	4.333864	1.000009	9.999995	8.999993
[94]	4.348418	1	9.999995	9
[95]	4.221091	1.000013	9.999999	9
[96]	4.729349	1.000004	10	8.999946
[97]	4.313738	1.000017	9.999994	8.999982
[98]	4.373881	1	9.999996	8.999986
[99]	4.281038	1.000042	9.999998	8.999977
[100]	4.223485	1	9.999998	8.999997
[101]	4.31713	1.000011	9.999994	8.99998
[102]	4.325197	1.00001	9.999997	8.999984
[103]	4.326769	1.000002	9.999999	8.999987
[104]	4.183312	1.000004	9.999997	8.999986
[105]	4.228574	1.000005	9.999996	8.999994
[106]	4.244214	1.000005	9.999998	8.999988
[107]	4.231191	1.000001	9.999998	8.999995
[108]	4.301066	1.00001	9.999996	9
[109]	4.838092	1.000015	9.999994	8.999995
[110]	4.36525	1.000017	9.999997	8.999994
[111]	4.307683	1.000005	9.999999	8.999998
[112]	4.35382	1.000019	9.999996	8.999999
[113]	4.782116	1.000025	10	8.999993
[114]	4.368584	1.000036	9.999997	8.999996
[115]	4.588015	1.000034	9.999998	9
[116]	4.31867	1.000016	9.999995	8.999988
[117]	4.358266	1.000026	9.999995	8.999997
[118]	4.349261	1.000013	9.999998	8.999997
[119]	4.378903	1.000022	9.999998	8.999993
[120]	4.276052	1.000011	9.999996	8.999992
[121]	4.940224	1	9.999991	8.999984
[122]	4.406804	1.000005	10	8.999996

[123]	4.407721	1.000008	9.999998	8.999988
[124]	4.368071	1.000007	9.999999	8.999995
[125]	4.312323	1.000022	9.999984	9
[126]	4.435061	1.000017	9.999996	8.999992
[127]	4.257972	1.000011	9.999997	8.999989
[128]	4.287416	1.000012	9.999998	8.999992
[129]	4.363853	1.000007	9.999998	8.999995
[130]	4.341783	1.000013	9.999996	8.999988
[131]	4.372692	1.000015	9.999996	8.999977
[132]	4.305574	1.000003	9.999997	8.999972
[133]	4.294472	1.000019	9.999997	8.999988
[134]	4.474781	1.000015	9.999998	8.999985
[135]	4.285838	1.000006	9.999996	8.999994
[136]	4.324078	1.000005	9.999998	8.999996
[137]	4.296192	1.000013	9.999997	8.999994
[138]	4.277037	1.000012	9.999996	8.999992
[139]	4.641076	1.000023	9.999994	9
[140]	4.262951	1.000007	9.999998	8.999985
[141]	4.288606	1.000017	9.999998	8.999984
[142]	4.405344	1.000003	10	8.999994
[143]	4.273233	1	10	8.999989
[144]	4.35649	1.000021	9.999997	8.999965
[145]	4.267906	1.0002	9.999999	9
[146]	4.359266	1.000005	9.999997	9
[147]	4.373655	1.000011	9.999999	8.999997
[148]	4.245602	1.000013	9.999997	8.99998
[149]	4.332035	1.000029	9.999994	8.999985
[150]	4.357659	1.000005	9.999998	8.999991
[151]	4.364836	1.00002	9.999997	8.999973
[152]	4.402734	1.000012	9.999999	9
[153]	4.303236	1.000016	9.999995	9
[154]	4.900046	1.000013	10	9
[155]	4.29545	1.000002	9.999997	8.999995
[156]	4.26457	1.000013	9.999999	8.999991
[157]	4.366987	1.000012	9.999999	8.999997
[158]	4.438273	1.000011	10	8.999999
[159]	4.624877	1	9.999999	8.999851
[160]	4.377228	1.000005	9.999999	8.999993
[161]	4.240002	1.000008	9.999996	8.999965
[162]	4.168429	1.000019	9.999997	8.999988
[163]	4.213403	1.000043	10	9
[164]	4.389664	1.000019	9.999997	9
[165]	4.301863	1.000014	9.999996	8.999975
[166]	4.346705	1.000002	9.999997	8.999991
[167]	4.36737	1.000016	9.999999	8.999997

[168]	4.309872	1.000005	9.999998	9
[169]	4.246929	1.000014	9.999997	8.999994
[170]	4.73907	1.000011	9.999998	8.999992
[171]	4.310303	1.000018	9.999995	8.999972
[172]	4.332838	1.000013	9.999997	8.999993
[173]	4.318882	1.000005	9.999997	8.999982
[174]	4.357069	1.000016	9.999999	8.999987
[175]	4.265098	1.00002	10	9
[176]	4.136409	1.000014	10	8.999995
[177]	4.34647	1.000012	9.999997	8.999996
[178]	4.387147	1.000013	9.999996	8.99999
[179]	4.306399	1.000009	9.999997	8.999995
[180]	4.313004	1	9.999999	8.999986
[181]	4.406664	1.000005	9.999998	8.999995
[182]	4.320858	1	10	9
[183]	4.286653	1.000008	9.999997	8.999991
[184]	4.388853	1.000032	9.999994	9
[185]	4.326921	1.000012	9.999997	8.999973
[186]	4.404344	1.00001	9.999998	8.999995
[187]	4.304181	1.000022	9.999993	8.999991
[188]	4.636208	1.000027	9.999996	8.999978
[189]	4.304649	1.000005	9.999997	8.999988
[190]	4.248091	1.000013	9.999996	8.999996
[191]	4.297495	1.000034	9.999995	8.999982
[192]	4.316872	1.000006	9.999998	8.999998
[193]	4.297272	1.000004	9.999997	8.999999
[194]	4.302656	1.000004	9.999998	9
[195]	4.325019	1.000004	9.999999	8.999992
[196]	4.277563	1.000052	9.999996	8.999801
[197]	4.273908	1.000004	9.999998	8.999987
[198]	4.278668	1.000004	9.999997	8.999988
[199]	4.361802	1.000012	9.999997	8.999989
[200]	4.929599	1.000003	9.999997	9
[201]	5.180005	1.000023	9.999996	8.999994
[202]	4.358973	1.000024	9.999997	8.999979
[203]	4.307022	1.000012	9.999997	8.999993
[204]	4.258666	1.000017	9.999998	9
[205]	4.268795	1.00001	9.999997	8.999996
[206]	4.379147	1.000006	10	8.999998
[207]	4.403233	1.000029	9.999999	9
[208]	4.413621	1.000034	10	9
[209]	4.349816	1.000017	9.999998	8.999988
[210]	4.333281	1.000025	9.999996	8.999972
[211]	4.388905	1.000036	9.999998	8.999996
[212]	4.335362	1.000012	9.999998	8.999994

[213]	4.238903	1.000065	9.999995	8.999857
[214]	4.35667	1	9.999998	8.999987
[215]	4.850633	1.000011	9.999997	8.999995
[216]	4.369198	1	9.999997	8.999993
[217]	4.337456	1.000008	9.999996	8.999992
[218]	4.437849	1.00002	9.999997	8.999985
[219]	4.349113	1.000005	9.999999	8.999995
[220]	4.150363	1.000006	9.999998	8.999997
[221]	4.327611	1	9.999997	8.999986
[222]	4.370172	1.000002	9.999997	8.999997
[223]	4.650198	1	9.999998	8.999992
[224]	4.372368	1.000003	9.999998	8.999988
[225]	4.350017	1.000006	9.999998	8.999992
[226]	4.339327	1	9.999999	8.999997
[227]	4.353988	1.000002	9.999998	8.999993
[228]	4.369078	1.000007	9.999997	8.999991
[229]	4.369964	1.000003	9.999998	8.99999
[230]	4.362159	1.000011	9.999997	8.999998
[231]	4.349219	1.000014	9.999996	8.999992
[232]	4.36302	1	9.999996	8.999994
[233]	4.453525	1.000005	10	9
[234]	4.364916	1.000009	9.999998	8.999995
[235]	4.41896	1.000005	9.999998	8.999995
[236]	4.348381	1.00001	9.999997	8.999998
[237]	4.353454	1.000004	9.999997	8.99999
[238]	4.349005	1.000006	9.999999	8.999991
[239]	4.590652	1.00001	9.999996	8.999994
[240]	4.372406	1	9.999998	8.999992
[241]	4.181291	1.000009	9.999997	8.999987
[242]	4.354295	1.000011	9.999999	8.999992
[243]	4.370947	1	9.999998	8.999989
[244]	4.342731	1	9.999999	8.999982

Chapter 8: Conclusions and future scope

Numerical simulation, optimization and thorough experimentation with the laser welding of the aluminium alloy 2024 were performed under certain constraints and limitations, like resource availability. The following conclusions are drawn from the current research investigations:

1. It is a well-known fact that it is challenging to obtain the numerical model of the process influenced by numerous factors. A three-dimensional transient thermos-fluid model is prepared to study the weld pool dynamics. It studies the impact of the Marangoni convection and buoyancy forces on laser welding. The fluid velocity and direction of the flow are identified, and the molten pool resembles an hourglass shape is concluded. The increase influences the depth of power penetration, and the change in scanning speed impacts it negatively. The hot metal flowing towards the weld pool's edge produces broader welds, higher temperatures cause surface tension and a radially inward flow that produces deeper welds
2. The selected material is weldable only at higher peak powers, and power as low as 2.5 kW did not weld the alloy. This problem in weldability is due to the thermos-physical properties of the material. The surface tension on the weld pool yielded a velocity of 0.6446 m/s and 0.4309 m/s at the higher and lower scanning speeds. A high melt flow gave welds with a higher aspect ratio.
3. Marangoni number was higher at higher power, has greater velocities and a Marangoni number of about 10^4 , suggesting that surface tension and Marangoni convection dominate.
4. The model is validated with the published data, and they agree well with a maximum error of 5% in penetration depth and 3% in weld width.
5. Successful utilization of the laser welding machine for joining two AA 2024 components with the objective of attaining good weld with maximum penetration depth and minimum weld width. The entire process depends on the proper choice of input parameters, peak power, scanning speed, frequency and pulse width.
6. The present research considers four control factors with three levels for butt joint welding mode. Peak power, scanning speed, pulse width and frequency

significantly impact the weld width and depth of penetration. There was only conduction mode welding when the power was lower, and the scanning speed was high. While the scanning speed is low and peak power is higher deep penetration occurred, but full penetration was not obtained in the selected window.

7. The second-order equations RSM developed can predict the responses' values with significant accuracy. The equations are checked for adequacy with a confidence interval of 95%. Graphical optimization results in overlay contours plots, which allow quick visual inspection of the area of possible response values in the factor space to choose the optimum welding parameter combination.

8. Using the same experimental data set, the process has been modelled using Gaussian process regression, which is a part of the deep learning technique. The radial bias kernel gave good values of the performance measure, R^2 . The post-training analysis proved the goodness of the proposed GPR model.

9. The material microstructure of the material, i.e. AA 2024, has been investigated using metallurgical and scanning electron microscopes. The columnar dendritic structure has been identified in the heat-affected zone. The honeycomb structure indicated the softening of the fusion zone.

10. Various defects are identified in the welding. Hot cracking is the most prominent, along with the undercut and humping.

11. A three-dimensional thermo-fluid model is developed to study the humping and the influence of various input parameters that impact humping. For the detailed study of the impact of the various parameters, the peak power and pulse width are considered while keeping the scanning speed and frequency as constants. The rise in pulse width has enhanced the humping formation at any constant peak power and frequency. The velocity of the molten fluid increased the hump height, and pulse width has shown a negligible rise in the hump height but is limited to only one pulse.

12. The process parameters that influenced the weld width and depth of penetration are further optimized using particle swarm optimization. The combination of parameters that result in a higher penetration depth and minimum weld width is given.

Hence, it is believed that the present set of research findings will not only open up new insights into the fundamental and applied research in the area of the laser welding of aluminium alloys but also be quite valuable for the manufacturing industry and tool rooms for making a quantum jump to the arena of the present day needs of the welding varieties of other light metal alloys in the changing scenario of the physical requirements of the parts or products.

8.2 Scope of future work

Laser welding of AA 2024 is emerging and is imperative to the industry. There is a vast scope for research in this area. Several recommendations for further research have arisen from this thesis

1. The present 3-D thermo-fluid model is validated by the weld dimensions, which validate the thermal physics of the model. That is adequate for reasonably predicting the transient temperature field and weld dimensions as a function of process parameters. However, a further experiment is required to validate the mechanical responses of the FE simulation (e.g., residual stress and distortion) to corroborate the proposed model and establish quantitative correlations between the FE simulation and experiments.
2. Thermal imaging can be used to measure the welded components' surface temperature distribution to compare the observed temperature to the predicted surface temperatures from the thermal model.
3. Gaps at mating joints pose a significant challenge for laser welding of aluminium alloys due to the formation of oxides. Shielding gas also can be varied, and its impact can be studied.
4. The numerical analysis could also be extended to other materials if the database of temperature-dependent thermo-physical and mechanical properties of other plastic materials is available. The impact strength and fatigue properties of the welded part can be studied.
5. Detailed analysis of the microstructure and its variation with the process parameters gives good scope for improving the weld quality.

Bibliography

- [1] Yung, C. S., Wu, B., Lei, S., Cheng, G. J. and Yao, Y. L. (2020), 'Overview of Laser Applications in Manufacturing and Materials Processing in Recent Years', *Journal of Manufacturing Science and Engineering* **142**(11), 110818.
- [2] 'Laser welding machines market' (2022), accessed March 23, 2022, <https://www.mordorintelligence.com/industry-reports/laser-welding-machines-market>.
- [3] Kannatey-Asibu, E. J. (2009), *Principles of laser materials processing*, John Wiley & Sons, New York.
- [4] Tarasov, L. (1986), *Laser physics and applications*, Mir Publishers, Moscow.
- [5] Majumdar, J. and Manna, I. J. D. Majumdar and I. Manna, ed., (2013), *Laser-Assisted Fabrication of Materials*, Springer, chapter Introduction to Laser Assisted Fabrication of Materials, pp. 1 - 67.
- [6] Ion, J. C. (2005), *Laser Processing of Engineering Materials Principles, Procedure and Industrial Application*, Elsevier.
- [7] Fabbro, R.S. Katayama, ed., (2013), *Handbook of Laser Welding Technologies*, Woodhead Publishing, chapter Developments in Nd: YAG laser welding, pp. 47 - 72.
- [8] Shcheglov, P. Y., Gumenyuk, A. V., Gornushkin, I. B., Rethmeier, M. and Petrovskiy, V. N. (2013), 'Vapor-plasma plume investigation during high-power fiber laser welding', *Laser Physics* **23**, 016001.
- [9] Semak, V. and Matsunawa, A. (1997), 'The role of recoil pressure in energy balance during laser materials processing.', *Journal of Physics D: Applied Physics* **30**, 2541- 552.
- [10] Coviello, D., D'Angola, A. and Sorgente, D. (2022), 'Numerical Study on the Influence of the Plasma Properties on the Keyhole Geometry in Laser Beam Welding', *Frontiers in Physics* **9**, 754672.

- [11] Hong, W., Shi, Y. and Gong, S. (2006), 'Numerical simulation of laser keyhole welding processes based on control volume methods', *Journal of Physics D: Applied Physics* **39**, 4722-4730.
- [12] Chen, Y., Lei, Z. K., Bai, R. X., Wei, Y. P. and Tao, W. (2017), Study on Elastoplastic Crack Propagation Behavior of Laser-welded 6061 Aluminum Alloy Using Digital Image Correlation Method, in 'IOP Conference Series', IOP Publishing Ltd, pp. 012040.
- [13] Xue, B., Chang, B. and Du, D. (2022), 'Monitoring of high- speed Laser welding process based on vapour plume.', *Optics and Laser Technology* **147**, 107649.
- [14] Lippold, J. C. (2015), *Welding Metallurgy and Weldability*, John Wiley & Sons: New Jersey.
- [15] Kou, S. (2003), *Welding Metallurgy*, John Wiley & Sons, New York.
- [16] Guitterez, L., Neye, G. and Zschech, E. (1996), 'Microstructure, hardness profile and tensile strength in welds of AA6013-T6 extrusions.', *Welding journal* **75**(4), 115S-121S.
- [17] Milewski, J., Lewis, G. K. and Wittig, J. E. (1999), 'Microstructural evaluation of low and high duty cycle Nd:YAG laser beam welds in 2024-T3 Aluminum', *Welding Journal* **72**(7), 341S-346S.
- [18] Cao, X., Wallac, W., Immarigeon, J. P. and Poon, C. (2007), 'Research and Progress in Laser Welding of Wrought Aluminum Alloys. II. Metallurgical Microstructures, Defects, and Mechanical Properties.', *Materials and Manufacturing Processes* **18**(1), 23-49.
- [19] Gaumann, M. and Kurz, W. (1998), Why Is It so Difficult to Produce an Equiaxed Microstructure During Welding?, in 'Numerical analysis of weldability', Institute of Materials, pp. 125-136.
- [20] Adisa, S. B., Loginova, I., Khalil, A. and Solonin, A. (2018), 'Effect of Laser Welding Process Parameters and Filler Metals on the Weldability and the Mechanical Properties of AA7020 Aluminium Alloy.', *Journal of Manufacturing and Materials Processing* **2**(2), 33.

- [21] Ayoolaa, W. A., Suder, W. J. and Williams, S. W. (2019), 'Effect of beam shape and spatial energy distribution on weld bead geometry in conduction welding', *Optics and Laser Technology* **117**, 280-287.
- [22] Courtois, M., Carin, M., Le Masson, P., Gaied, S. and & Balabane, M. (2013), 'A new approach to compute multi-reflections of laser beam in a keyhole for heat transfer and fluid flow modelling in laser welding.', *Journal of Physics D: Applied Physics* **14**, 505305.
- [23] Xu, J., Yi, L., Zhu, L., Han, J., Zhang, C. and Chen, D. (2019), 'Effect of shielding gas on the plasma plume in pulsed laser welding.', *Measurement* **134**, 25-32.
- [24] Kou, S. and Sun, D. (1985), 'Fluid flow and weld penetration in stationary arc welds', *Metallurgical Transactions: A* **16**, 203 - 213.
- [25] Ratchev, P., Verlinden, B., De Smet, P. and Van Houtte, P. (1998), 'Precipitation hardening of an Al- 4.2wt% Mg-0.6wt% Cu alloy.', *Acta Materialia*. **46**(10), 3523-3533.
- [26] Frewin, M. R. and & Scott, D. A. (1999), 'Finite element model of pulsed laser welding.', *Welding Journal: Welding Research Support* **78**, 15s - 22s.
- [27] Limmaneevichitr, C. and Kou, S. (2000), 'Visualization of Marangoni Convection in simulated weld pools.', *Welding Journal: Welding Research Support* **79**, 126s - 135s.
- [28] Miller, W. S., Zhuang, L., Bottema, J., Wittebrood, A. J., De Smet, P., Haszler, A. and Vieregge, A. (2000), 'Recent development in aluminium alloys for the automotive industry.', *Materials Science and Engineering: A* **280**, 37 - 49.
- [29] Matsunawa, A., Mizutani, M., Katayama, S. and Seto, N. (2003), 'Porosity formation mechanism and its prevention in laser lap welding for T-joints', *Welding International* **17**, 431 - 437.
- [30] Borrisutthekul, R., Miyashita, Y. and Mutoh, Y. (2005), 'Dissimilar material laser welding between magnesium alloy AZ31B and aluminum

alloy A5052-O', *Science and Technology of Advanced Materials* **6**(2), 199 - 204.

- [31] Zhou, J., Tsai, H. and Wang, P. (2005), Transport Phenomena and the Associated Humping Formation in Laser Welding, *in* , pp. 945-953.
- [32] Fabbro, R., Slimani, S., Doudet, I., Coste, F. and Briand, F. (2006), 'Experimental study of the dynamical coupling between the induced vapour plume and the melt pool for Nd-YAG CW laser welding.', *Journal of Physics D: Applied Physics* **39**, 394.
- [33] Kuo, T. Y. and Lin, Y. T. (2006), 'Effects of shielding gas flow rate and power waveform on Nd:YAG Laser welding of A5754-O Aluminium alloy', *Materials Transactions* **47**, 1365 - 1373.
- [34] Balasubramanian, K. R., Shanmugam, N. S., Buvanashakaran, G. and Sankaranarayanan, K. (2008), 'Numerical and experimental investigation of laser beam welding of AISI 304 stainless steel sheet', *Advances in Production Engineering & Management* **3**(2), 93-105.
- [35] Missori, S., Sili, A. and Ucciardello, N. (2008), 'Process Parameters Optimization of Laser Beam Welded Joints by Neural Network.', *Materials and Manufacturing Processes* **23**, 168-173.
- [36] Moraitis, G. A. and Labeas, G. N. (2008), 'Residual stress and distortion calculation of laser beam welding for aluminum lap joints.', *Journal of Materials Processing Technology* **198**(1 - 3), 260-269.
- [37] Akman, E. R. H. A. N., Demir, A., Canel, T. I. M. U. R. and Sinmazçelik, T. (2009), 'Laser welding of Ti6Al4V Titanium alloys', *Journal of Materials Processing Technology* **209**(8), 3705-3713.
- [38] Ghaini, F. M., Sheikhi, M., Torkamany, M. J. and Sabbaghzadeh, J. (2009), 'The relation between liquation and solidification cracks in pulsed laser welding of 2024 Aluminium alloy.', *Materials Science and Engineering: A* **519**, 167 - 171.
- [39] Amara, E. H. and Fabbro, R. (2010), 'Modeling of humps formation during deep-penetration laser welding.', *Applied Physics A* **101**, 111 -

- [40] Amara, E. H. (2010), Humping modelling in deep penetration laser welding, *in* S. Hinduja and Lin & Li, ed., 'Proceedings of the 36th International MATADOR Conference', Springer, London, pp. 271-274.
- [41] Bachmann, M., Avilov, V., Gumenyuk, A. and Rethmeier, M. (2011), 'Numerical simulation of full-penetration laser beam welding of thick aluminium plates with inductive support', *Journal of Physics D: Applied Physics* **45**(3), 035201.
- [42] Kaplan, A. F. H. and Powell, J. (2011), 'Spatter in laser welding', *Journal of Laser Applications* **23**, 032005.
- [43] Turňa, M., Taraba, B., Ambrož, P. and Sahul, M. (2011), 'Contribution to numerical simulation of Laser welding.', *Physics Procedia* **12**, 638 - 645.
- [44] Volpp, J. (2012), 'Investigation on the influence of different laser beam intensity distributions on keyhole geometry during laser welding', *Physics Procedia* **39**, 17 - 26.
- [45] Ilar, T., Eriksson, I., Powell, J. and Kaplan, A. (2012), 'Root humping in laser welding – an investigation based on high-speed imaging.', *Physics Procedia* **39**, 27 - 32.
- [46] Acherjee, B., Kuar, A. S., Mitra, S. and Misra, D. (2012), 'Effect of carbon black on temperature field and weld profile during laser transmission welding of polymers: A FEM study.' *Optics & Laser Technology* **44**(3), 514-521.
- [47] Acherjee, B., Kuar, A. S., Mitra, S. and Misra, D. (2012), 'Modeling of laser transmission contour welding process using FEA and DoE.' *Optics & Laser Technology* **44**(5), 1281-1289.
- [48] Enz, J., Riekehr, S., Ventzke, V. and Kashaev, N. (2012), 'Influence of the local chemical composition on the mechanical properties of laser beam welded Al-Li Alloys.' *Physics Procedia* **39**, 51 - 58.
- [49] Courtois, M., Carin, M., LeMasson, P., Gaied, S. and France, L. (2012),

'Keyhole formation during spot laser welding: Heat and fluid flow modeling in a 2D axisymmetric configuration.' 'Proceedings of the 2012 COMSOL Conference in Milan', COMSOL, 1-6.

- [50] Courtois, M., Carin, M., Le Masson, P., Gaied, S. and Balabane, M. (2013), 'Complete heat and fluid flow modeling of keyhole formation and collapse during spot laser welding.' 'International Congress on Applications of Lasers & Electro-Optics', The Laser Institute, Miami, United States, 77-84.
- [51] Brock, C., Tenner, F., Klampfl, F., Hohenstein, R. and Schmidt, M. (2013), 'Detection of weld defects by high-speed imaging of the vapor plume.', *Physics Procedia* **41**, 539 - 543.
- [52] Gao, X. L., Zhang, L. J., Liu, J. and Zhang, J. X. (2013), 'A comparative study of pulsed Nd: YAG laser welding and TIG welding of thin Ti6Al4V Titanium alloy plate', *Materials Science and Engineering: A* **559**, 14 - 21.
- [53] Akbari, M., Saedodin, S., Toghraie, D., Shoja-Razavi, R. and Kowsari, F. (2014), 'Experimental and numerical investigation of temperature distribution and melt pool geometry during pulsed laser welding of Ti6Al4V alloy.', *Optics & Laser Technology* **59**, 52-59.
- [54] Bachmann, M., Avilov, V., Gumenyuk, A. and Rethmeier, M. (2014), 'Experimental and numerical investigation of an electromagnetic weld pool control for laser beam welding.', *Physics Procedia* **56**, 515-524.
- [55] Bachmann, M., Avilov, V., Gumenyuk, A. and Rethmeier, M. (2014), 'Experimental and numerical investigation of an electromagnetic weld pool support system for high power laser beam welding of austenitic stainless steel.', *Journal of Materials Processing Technology* **214**(3), 578-591.
- [56] Lecoanet, A., Ivey, D. G. and Henein, H. (2014), Simulation of the temperature profile during welding with COMSOL multiphysics® software using Rosenthal's approach., in 'Proceedings of the 2014 COMSOL Conference'.

- [57] Narasimhachary, D., Bathe, R. N., Padmanabham, G. and Basu, A. (2014), 'Influence of temperature profile during laser welding of aluminium alloy 6061 T6 on microstructure and mechanical properties.', *Materials and Manufacturing Processes* **29**, 948 - 953.
- [58] Xiao, R. and Zhang, X. (2014), 'Problems and issues in laser beam welding of Aluminum–Lithium alloys', *Journal of Manufacturing Processes* **16**, 166 - 175.
- [59] Zhang, L. J., Zhang, J. X., Gumenyuk, A., Rethmeier, M. and Na, S. J. (2014), 'Numerical simulation of full penetration laser welding of thick steel plate with high power high brightness laser.', *Journal of materials processing technology* **214**(8), 1710 - 1720.
- [60] Alfieria, V., Caiazzo, F. and Sergi, V. (2015), 'Autogenous laser welding of AA 2024 aluminium alloy: Process issues and bead features.', *Procedia CIRP* **33**, 406 - 411.
- [61] Bachmann, M., Avilov, V., Gumenyuk, A. and Rethmeier, M. (2015), Experimental and numerical investigation of an electromagnetic weld pool support system for high power laser beam welding of austenitic stainless steel., in 'International congress on applications of laser and electro optics'.
- [62] Chukkan, J. R., Vasudevan, M., Muthukumaran, S., Kumar, R. R. and Chandrasekhar, N. (2015), 'Simulation of laser butt welding of AISI 316L stainless steel sheet using various heat sources and experimental validation', *Journal of Materials Processing Technology* **219**, 48 - 59.
- [63] Pang, S., Chen, X., Zhou, J., Shao, X. and Wang, C. (2015), '3D transient multiphase model for keyhole, vapor plume, and weld pool dynamics in laser welding including the ambient pressure effect.', *Optics and Lasers in Engineering* **74**, 47 - 58.
- [64] Sheikhi, M., Ghaini, F. M. and Assadi, H. (2015), 'Prediction of solidification cracking in pulsed laser welding of 2024 aluminium alloy.', *Acta Materialia* **82**, 491 - 502.

- [65] Zhang, X., Yang, W. and Xiao, R. (2015), 'Microstructure and mechanical properties of laser beam welded Al–Li alloy 2060 with Al–Mg filler wire.', *Materials and Design* **88**, 446 - 450.
- [66] Zhang, X., Huang, T., Yang, W., Xiao, R., Liu, Z. and Lica, L. (2016), 'Microstructure and mechanical properties of laser beam-welded AA2060 Al-Li alloy', *Journal of Materials Processing Technology* **237**, 301 - 308.
- [67] Atabaki, M. M., Yazdian, N. and Kovacevic, R. (2016), 'Partial penetration laser-based welding of aluminium alloy (AA 5083 – H32)', *Optik* **127**, 6782 - 6804.
- [68] Bakir, N., Gumenyuk, A. and Rethmeier, M. (2016), 'Numerical simulation of solidification crack formation during laser beam welding of austenitic stainless steels under external load', *Welding in the World* **60**(5), 1001 - 1008.
- [69] Courtois, M., Carin, M., Le Masson, P., Gaied, S. and Balabane, M. (2016), 'Guidelines in the experimental validation of a 3D heat and fluid flow model of keyhole laser welding', *Journal of Physics D: Applied Physics* **49**(15), 155503.
- [70] Otto, A., Patschger, A. and Seiler, M. (2016), 'Numerical and experimental investigations of humping phenomena in Laser micro welding.', *Physics Procedia* **83**, 1415 - 1423.
- [71] Ahn, J., He, E., Chen, L., Dear, J. and Davies, C. (2017), 'The effect of Ar and He shielding gas on fibre laser weld shape and microstructure in AA 2024 – T3', *Journal of Manufacturing Processes* **29**, 62 - 73.
- [72] Ai, Y., Jiang, P., Shao, X., Li, P. and Wang, C. (2017), 'A three-dimensional numerical simulation model for weld characteristics analysis in fiber laser keyhole welding.', *International Journal of Heat and Mass Transfer* **108**, 614 - 626.
- [73] D'Ostuni, S., Leo, P. and Casalino, G. (2017), 'FEM Simulation of Dissimilar Aluminum Titanium Fiber Laser Welding Using 2D and 3D

Gaussian Heat Sources', *Metals* **7**, 307.

- [74] Hong, K. – M. and Shin, Y. C. (2017), 'Prospects of laser welding technology in the automotive industry: A review.', *Journal of Materials Processing Technology* **254**, 46 - 69.
- [75] Liebl, S., Stadter, C., Ganser, A. and Zaeh, M. F. (2017), 'Numerical simulation of laser beam welding using an adapted intensity distribution.', *Journal of Laser Applications* **29**, 022405.
- [76] Meco, S., Cozzolino, L., Ganguly, S., Williams, S. and McPherson, N. (2017), 'Laser welding of steel to aluminium: Thermal modelling and joint strength analysis.', *Journal of Materials Processing Technology* **247**, 121 - 133.
- [77] Loginova, I., Khalil, A., Pozdniakov, A., Solonin, A. and Zolotorevskiy, V. (2017), 'Effect of pulse laser welding parameters and filler metal on microstructure and mechanical properties of Al-4.7Mg-0.32Mn-0.21Sc-0.1Zr Alloy', *Metals* **7**, 564.
- [78] Ng, C. H., Yahaya, S. N. M. and Majid, A. A. A. (2017), 'Reviews on aluminium alloy series and its applications.', *Academia Journal of Scientific Research* **5**, 708 - 716.
- [79] Sanchez-Amaya, J. M., Pasang, T., Amaya-Vazquez, M. R., Lopez-Castro, J. D., Churiaque, C., Tao, Y. and Pedemonte, F. J. B. (2017), 'Microstructure and Mechanical Properties of Ti5553 Butt Welds Performed by LBW under Conduction Regime.', *Metals* **7**, 269.
- [80] Shen, F., Zhao, B., Li, L., Kai Chua, C. and Zhou, K. (2017), 'Fatigue damage evolution and lifetime prediction of welded joints with the consideration of residual stresses and porosity.', *International Journal of Fatigue*. **103**, 272 - 279.
- [81] Svenungsson, J., Choquet, I. and Kaplan, A. (2017), 'Marangoni force and numerical instability when modelling keyhole laser welding.' 'Proceedings of LIM'.
- [82] Xue, X., Pereira, A. B., Amorim, J. and Liao, J. (2017), 'Effects of Pulsed

Nd:YAG Laser Welding Parameters on Penetration and Microstructure Characterization of a DP1000 Steel Butt Joint.', *Metals* **7**, 292.

- [83] Ahn, J., Chen, L., He, E., Dear, J. P. and Davies, C. M. (2018), 'Effect of filler metal feed rate and composition on microstructure and mechanical properties of fibre laser welded 2024-T3 aluminium alloy.', *Journal of Manufacturing Process* **34**, 70 - 85.
- [84] Artinov, A., Bachmann, M. and Rethmeier, M. (2018), 'Equivalent heat source approach in a 3D transient heat transfer simulation of full-penetration high power laser beam welding of thick metal plates.', *International Journal of Heat and Mass Transfer* **122**, 1003 - 1013.
- [85] Fetzer, F., Berger, P., Hu, H., Weber, R. and Graf, T. (2018), Pores in laser beam welding: generation mechanism and impact on the melt flow., in 'SPIE Proceedings, 10525: High-Power laser materials processing: Applications, Diagnostics and Systems VII', SPIE, San Francisco, United States, pp. 105250D.
- [86] Fotovvati, B., Wayne, S. F., Lewis, G. and Asadi, E. (2018), 'A review on melt-pool characteristics in laser welding of metals.', *Advances in Materials Science and Engineering* **2018**, 4920718.
- [87] Maina, M., Okamoto, Y., Okada, A., Narhi, M., Kangastupa, J. and Vihinen, J. (2018), 'High surface quality of aluminium using adjustable ring-mode fiber laser.', *Journal of material processing technology* **258**, 180 - 188.
- [88] Panwisawas, C., Sovani, Y., Turner, R. P., Brooks, J. W., Basoalto, H. C. and Choquet, I. (2018), 'Modelling of thermal fluid dynamics for fusion welding.', *Journal of Materials Processing Technology*. **252**, 176 - 182.
- [89] Patschger, A., Seiler, M. and Bliedtner, J. (2018), 'Influencing factors on humping effect in laser welding with small aspect ratios.', *Journal of Laser Applications* **30**, 032409.
- [90] Artinov, A., Karkhin, V., Khomich, P., Bachmann, M. and Rethmeier,

- M. (2019), 'Assessment of thermal cycles by combining thermo-fluid dynamics and heat conduction in keyhole mode welding processes.', *International Journal of Thermal Sciences* **145**, 105981.
- [91] Mehrapouya, M., Gisario, A., Huang, H., Rahimzadeh, A. and Elahinia, M. (2019), 'Numerical study for prediction of optimum operational parameters in laser welding of NiTi alloy.', *Optics and Laser Technology* **118**, 159 - 169.
- [92] Ghosh, A., Misra, D. and Acharyya, S. (2019), 'Numerical Simulation of the Laser Welding of 2205 Duplex Stainless Steel.', *International Journal of Laser Science*. **1**, 293 - 313.
- [93] Cao, L., Zhang, L. and Wu, Y. (2020), 'A data-driven model for weld bead monitoring during the laser welding assisted by magnetic field.', *The International Journal of Advanced Manufacturing Technology* **107**, 475 - 487.
- [94] Feng, Y., Gao, X., Zhang, X., Peng, C., Gui, X., Sun, Y. and Xiao, X. (2021), 'Simulation and experiment for dynamics of laser welding keyhole and molten pool at different penetration status.', *The International Journal of Advanced Manufacturing Technology*. **112**, 2301 - 2312.
- [95] Moges, T., Yang, Z., Jones, K., Feng, S., Witherell, P. and Lu, Y. (2021), 'Hybrid modeling approach for melt-pool prediction in Laser powder bed fusion additive manufacturing.', *Journal of Computing and Information Science in Engineering* **21**, 050902-1.
- [96] Luo, H., Zeng, H., Hu, L., Hu, X. and Zhou, Z. (2005), 'Application of artificial neural network in laser welding defect diagnostics.', *Journal of Materials Processing Technology* **170**, 403 - 411.
- [97] Shanmugam, N. S., Buvanashakaran, G., Sankaranarayananasamy, K. and Kumar, S. R. (2010), 'A transient finite element simulation of the temperature and bead profiles of T-joint laser welds.', *Materials & Design* **31**(9), 4528 - 4542.

- [98] Jiang, P., Wang, C., Zhou, Q., Shao, X., Shu, L. and Li, X. (2016), 'Optimization of laser welding process parameters of stainless steel 316L using FEM, Kriging and NSGA-II.', *Advances in Engineering Software* **99**, 147 - 160.
- [99] Bagchi A., S. S. K. G. S. M. G. R. K. (2017), 'Numerical simulation and optimization in pulsed Nd: YAG laser welding of Hastelloy C-276 through Taguchi method and artificial neural network.', *Optik* **146**, 80 - 89.
- [100] Zhao, D., Zhao, K., Ren, D. and Guo, X. (2017), 'Ultrasonic Welding of Magnesium–Titanium Dissimilar Metals: A Study on Influences of Welding Parameters on Mechanical Property by Experimentation and Artificial Neural Network.', *Journal of Manufacturing Science and Engineering* **139**, 031019.
- [101] Wang, Q., Liu, X., Yan, Z., Dong, Z. and Yan, D. (2017), 'On the mechanism of residual stresses relaxation in welded joints under cyclic loading.', *International Journal of Fatigue*. **105**, 43 - 59.
- [102] Lei, Z., Shen, J., Wang, Q. and Chen, Y. (2019), 'Real-time weld geometry prediction based on multi-information using neural network optimized by PCA and GA during thin-plate laser welding.', *Journal of Manufacturing Processes*. **43**, 207 - 217.
- [103] Zhang, M., Liu, T., Hu, R., Mu, Z., Chen, S. and Chen, G. (2020), 'Understanding root humping in high-power laser welding of stainless steels: a combination approach.', *The International Journal of Advanced Manufacturing Technology* **106**, 5353 - 5364.
- [104] Yusof, M., Ishak, M. and Ghazali, M. F. (2021), 'Weld depth estimation during pulse mode laser welding process by the analysis of the acquired sound using feature extraction analysis and artificial neural network.', *Journal of Manufacturing Processes*. **63**, 163 - 178.
- [105] Oh, S., Kim, H., Nam, K. and Ki, H. (2021), 'Deep-learning approach for predicting laser-beam absorptance in full-penetration laser keyhole welding', *Optics express* **29**, 20010 - 20021.

- [106] Li, R., Dong, M. and Gao, H. (2021), 'Prediction of Bead Geometry with Changing Welding Speed Using Artificial Neural Network.', *Materials* **14**, 1494.
- [107] Marimuthu, S., Eghio, R. M., Pinkerton, A. J. and Li, L. (2013), 'Coupled computational fluid dynamic and Finite element multiphase modeling of laser weld bead formation and joint strength.', *Journal of Manufacturing Science and Engineering* **135**, 011004-1.
- [108] Okon, P, Dearden, G, Watkins, K, Sharp, M and French, P (2002), 'Laser welding of aluminium alloy 5083', *International Congress on Applications of Lasers & Electro-Optics* **2002**(1), 158364.
- [109] Parsopoulos, K. E. and Vrahatis., M. N. (2010), *Particle swarm optimization and intelligence; advances and applications.*, Book News, Inc.
- [110] Pastor, M, Zhao, H, Martukanitz, RP and Debroy, T (1999), 'Porosity, Underfill and Magnesium loss during continuous wave Nd: YAG laser welding of thin plates of Aluminum alloys 5182 and 5754.', *Welding Journal* **78**(6), 207s - 216s.
- [111] Robati A., B. G. A. P. H. F. M. J. and Anaraki, J. (2012), 'Balanced fuzzy particle swarm optimization.', *Applied Mathematical Modelling* **36**, 2169 - 2177.
- [112] Sakamoto H., S. K. and Dausinger, F. (2003), 'Effect of alloying elements on weld properties in CO2 laser welding of Aluminium alloys', *Welding International* **17**(7), 509 - 513.
- [113] Sánchez-Amaya J.M., B. Z. A.-V. M. and Botana, F. (2012), 'Laser weldability of aluminium alloys with high power diode laser', *Welding Journal* **91**(5), 155 - 161.
- [114] Shakeri, H. R., Buste, A., Worswick, M. J., Clarke, J. A., Feng, F., Jain, M. and Finn, M. (2002), 'Study of damage initiation and fracture in aluminum tailor welded blanks made via different welding techniques', *Journal of Light Metals* **2**(2), 95 - 110.

- [115] Huntington, C. A. and Eagar, T. W. (1983), 'Laser Welding of Aluminum and Aluminum Alloys', *Welding Journal* **62**(4), 105 - 107.
- [116] Leong, K. H., Sabo, K. R., Altshuller, B., Wilkinson, T. L. and Albright, C. E. (1999), 'Laser beam welding of 5182 Aluminum alloy sheet', *Journal of Laser Applications* **11**(3), 109 - 118.
- [117] Zhao, H., White, D. R. and Debroy, T. (1999), 'Current issues and problems in laser welding of automotive Aluminium alloys.', *International Materials Reviews* **44**(6), 238 - 266.
- [118] El-Batahgy, A. M. and Kutsuna, M. (2009), 'Laser Beam Welding of AA5052, AA5083, and AA6061 Aluminum Alloys', *Advances in Materials Science and Engineering* **2009**, 974182.
- [119] Squillace, A. and Prisco, U. (2009), 'Influence of filler material on micro- and macro-mechanical behaviour of laser-beam-welded T-joint for aerospace applications.', *Proceedings of the Institution of Mechanical Engineers, Part L: Journal of Materials: Design and Applications*. **223**(3), 103 - 115.
- [120] Choi, K. D., Ahn, Y. N. and Kim, C. (2010), 'Weld strength improvement for Al alloy by using laser weaving method', *Journal of Laser Applications* **22**(3), 116.
- [121] Fabrègue, D. and Deschamps, A. (2002), 'Microstructural Study of Laser Welds Al6056-AS12 in Relation with Hot Tearing.', *Materials Science Forum* **396 - 402**, 1562 - 1572.
- [122] Yang, Z. B., Tao, W., Li, L. Q., Chen, Y. B., Li, F. Z. and Zhang, Y. L. (2012), 'Double-sided laser beam welded T-joints for aluminum aircraft fuselage panels: Process, microstructure, and mechanical properties.', *Materials & Design* **33**, 652 - 658.
- [123] Li, M., Li, Z., Zhao, Y., Li, H., Wang, Y. and Huang, J. (2011), 'Influence of Welding Parameters on Weld Formation and Microstructure of Dual-Laser Beams Welded T-Joint of Aluminum Alloy.', *Advances in Materials Science and Engineering* **2011**, 767260.

- [124] Liu, C., Northwood, D. and Bhole, S. (2004), 'Tensile fracture behavior in CO₂ laser beam welds of 7075-T6 Aluminum alloy.', *Materials & Design* **25**(7), 573 - 577.
- [125] Cui, L., Li, X., He, D., Chen, L. and Gong, S. (2012), 'Effect of Nd:YAG laser welding on microstructure and hardness of an Al–Li based alloy', *Materials Characterization* **71**, 95 - 102.
- [126] Bardin F., M. R. M. A. M. S. W. S. J. J. D. C. (2004), 'Real-time temperature measurement for process monitoring of laser conduction welding', *Journal of Laser Applications* **ICALEO 2004**, 1309.
- [127] Hu, B. and Richardson, I. M. (2005), 'Autogenous laser keyhole welding of Aluminum alloy 2024.', *Journal of Laser Applications* **17**, 70.
- [128] Alfieri, V., Cardaropoli, F., Caiazzo, F. and Sergi, V. (2011), 'Porosity evolution in aluminum alloy 2024 bop and butt defocused welding by Yb-YAG disk laser.', *Engineering Review*. **31**(2), 125 - 132.
- [129] Caiazzo, F., Alfieri, V., Cardaropoli, F. and Sergi, V. (2013), 'Butt autogenous laser welding of AA 2024 aluminium alloy thin sheets with a Yb:YAG disk laser.', *International Journal of Advanced Manufacturing Technology*. **67**, 2157 - 2169.
- [130] Kuo, T. and Lin, Y. T. (2006), 'Effects of Shielding Gas Flow Rate and Power Waveform on Nd:YAG Laser Welding of A5754-O Aluminum Alloy', *Materials Transactions* **47**(5), 1365 - 1373.
- [131] Howard K., L. S. and Zhou, Y. (2006), 'Welding aluminum sheet using a highpower diode laser', *Welding Journal* **85**(5), 101 - 110.
- [132] ASTM 'E3 Methods for Preparation of Metallographic Specimens', ASTM International.
- [133] Cao, X., Jahazi, M., Immarigeon, J. P. and Wallace, W. (2006), 'A review of laser welding techniques for magnesium alloys.', *Journal of Materials Processing Technology* **171**(2), 188 - 204.
- [134] AWS C7.2 'Recommended Practices for Laser Beam Welding, Cutting and Drilling.'

- [135] TR17671-6:2005. (2005), 'Welding - Recommendations for welding of metallic materials - Part 6: Laser beam welding.', ISO.
- [136] EN 1011-6:2005. (2005), 'Welding. Recommendations for welding of metallic materials. Laser beam welding.', BS.
- [137] EN 1321:1997. (1997), 'Destructive test on welds in metallic materials. Macroscopic and microscopic examination of welds.', BS.
- [138] Cleric, M. (2006), *Particle Swarm Optimization*, Wiley-ISTE.
- [139] Coello, C. A. C. (2000), Handling preferences in evolutionary multiobjective optimization: a survey, *in* 'Proceedings of the 2000 Congress on Evolutionary Computation. CEC00 (Cat. No.00TH8512)', pp. 30 - 37.
- [140] Sierra, M. and Coello, C. (2006), 'Multi-Objective Particle Swarm Optimizers: A Survey of the State-of-the-Art.', *International Journal of Computational Intelligence Research*. **2**(3), 287 - 308.
- [141] Nayak, S. K., Padhy, S. K. and Panigrahi, S. P. (2012), 'A novel algorithm for dynamic task scheduling', *Future Generation Computer Systems* **28**(5), 709 - 717.
- [142] Yu. Y. Z Ren, X.-y. S. D. F. J. S. J. (2012), 'Application of Improved PSO Algorithm in Hydraulic Pressing System Identification.', *Journal of Iron and Steel Research* **19**(9), 29 - 35.
- [143] He, X., Fuerschbach, P. W. and Debroy, T. (2003), 'Heat transfer and fluid flow during laser spot welding of 304 stainless steel.', *Journal of Physics D: Applied Physics* **36**, 1388 - 1398.
- [144] Gao, Z., Jiang, P., Mi, G., Cao, L. and Liu, W. (2018), 'Investigation on the weld bead profile transformation with the keyhole and molten pool dynamic behaviour simulation in high power laser welding.', *International journal of Heat and Mass Transfer* **116**, 1304 - 1313.
- [145] Liu, T., Mu, Z., Hu, R. and Pang, S. (2019), 'Sinusoidal oscillating laser welding of 7075 Aluminium alloy: Hydrodynamics, porosity formation and optimization.', *International Journal of Heat and Mass Transfer* **140**, 346 - 358.

- [146] Koo, B. S., Thasanaraphan, P. and Nied, H. F. (2019), 'Numerical simulation of the formation of hourglass welds during laser welding', *Journal of Material Processing Technology*. **263**, 175 - 186.
- [147] Zhang, R., Tnag, X., Xu, L., Lu, F. and Cui, H. (2020), 'Study of molten pool dynamics and porosity formation mechanism in full penetration fiber laser welding of Al-alloy.', *International Journal of Heat and Mass Transfer* **148**, 119089.
- [148] Li, Z., You, G., He, X., Li, S., Tian, C. and Dong, B. (2020), 'Analysis of surface tension driven flow and solidification behaviour in laser linear welding of stainless steel.', *Optics and Laser Technology* **123**, 105914.
- [149] Ai, Y., Zheng, K., Shin, Y. C. and Wu, B. (2018), 'Analysis of weld geometry and liquid flow in laser transmission welding between polyethylene (PET) and Ti6Al4V based on numerical simulation.', *Optics and Laser Technology*. **103**, 99 - 108.
- [150] Cho, W., Na, S. J., Thomy, C. and Vollertsen, F. (2011), 'Numerical simulation of molten pool dynamics in high power disk laser welding.', *Journal of Materials Processing Technology* **212**, 262 - 275.
- [151] Acherjee, B., Misra, D., Bose, D. and Venkadeshwaran, K. (2009), 'Prediction of weld strength and seam width for laser transmission welding of thermoplastic using response surface methodology.', *Optics & Laser Technology* **41**(8), 956 - 967.
- [152] 'ISO 15614-11:2002 (2002) Specification and qualification of welding procedures for metallic materials — Welding procedure test — Part 11 Electron and laser beam welding.', BS.
- [153] Hilton, P., Blackburn, J. and Chong, P. (2007), 'Welding of Ti-6Al-4V with fibre delivered laser beams.', *Journal of Laser Applications* **ICALEO 2007**, 1607.
- [154] Chen, L., Shuili, G. and Yang, J. (2012), Study on Full Penetration Stability of Light Alloys Sheet Laser Welding., in S. Hinduja and L. Li, ed., 'Proceedings of the 37th International MATADOR Conference', pp. 315 - 318.

- [155] Clifford, M. (2001), *ASME engineer's data book.*, ASME Press, Fairfield.
- [156] El-Batahgy, A.-M. (1997), 'Effect of laser welding parameters on fusion zone shape and solidification structure of austenitic stainless steels.', *Materials Letters* **32**(2 - 3), 155 - 163.
- [157] Chen. L. Hu, L. G. S. (2006), 'A study on the porosity of CO2 laser welding of titanium alloy.', *China Welding.* **15**(1), 1 - 5.
- [158] Aye, S. and Heyns, P. (2017), 'An integrated Gaussian process regression for prediction of remaining useful life of slow speed bearings based on acoustic emission.', *Mechanical Systems and Signal Processing* **84, Part A**, 485 - 498.
- [159] Brantson, E., Ju, B., Ziggah, Y., Akwensi, P., Sun, Y., Wu, D. and Addo, B. (2019), 'Forecasting of Horizontal Gas Well Production Decline in Unconventional Reservoirs using Productivity, Soft Computing and Swarm Intelligence Models', *Natural Resources Research* **28**, 717 - 756.
- [160] Yamaoka, H. (2001), 'Microstructural control of laser-welded Aluminium alloys.', *Welding International* **15**(11), 845 - 850.
- [161] Kanazawa, H. (1998), 'Welding performance of high power YAG lasers with Aluminium alloys.', *Welding International.* **12**(5), 341 - 346.
- [162] Zhao, H. and Debroy, T. (2001), 'Weld Metal Composition Change during Conduction Mode Laser Welding of Aluminum Alloy 5182.', *Metallurgical and Materials Transactions B* **32**(1), 163-172.
- [163] Pastor, M., Zhao, H., Martukanitz, R. P. and Debroy, T. (1999), 'Porosity, Underfill and Magnesium loss during continuous wave Nd: YAG laser welding of thin plates of aluminum alloys 5182 and 5754.', *Welding Journal.* **78**(6), 207s - 216s.
- [164] Leung M. F., N. S. C. C. C. C. and Lui, A. (2014), 'A new strategy for finding good local guides in MOPSO.' 'IEEE Congress on Evolutionary Computation (CEC)', IEEE, IEEE, Beijing, China, 1990 - 1997.



*Laser Welding of Aluminium Alloy 2024:
Experimental Investigation, Numerical
Simulation and Optimization*

A SUDHA KIRAN DUGGIRALA

D 7/10/22/19

Filters & Settings

FILTERS

- Exclude Quotes
- Exclude Bibliography

Exclude sources that are less than:

- words
- %
- Don't exclude by size

Exclude matches that are less than:

- 14 words
- Don't exclude

Exclude Sections:

- Abstract
- Methods and Materials

Includes variations: Method, Method, Materials, Materials and Methods

Smt
18/10/22

Acherjee
18/10/22

DR. BAPPA ACHERJEE
ASSISTANT PROFESSOR
DEPARTMENT OF PRODUCTION & INDUSTRIAL ENGINEERING
BIRLA INSTITUTE OF TECHNOLOGY
MESRA, RANCHI - 835215, INDIA

17 Oct 2022 10:02PM 4754 words • 132 matches • 55 sources FAQ

iThenticate Laser Welding of Aluminium Alloy 2024: Experimental Investigation, Numerical Simulation and Optimization Quotes Excluded 6% Bibliography Excluded 336.4%

Laser Welding of Aluminium Alloy 2024: Experimental Investigation, Numerical Simulation and Optimization

A SUDHA KIRAN DUGGIRALA

D. 7/ISLM/22/19

Match Overview

1	Internet 250 words created on 16-Aug-2022 maifitace.com	<1%
2	Internet 244 words created on 16-Dec-2021 opu4.kobv.de	<1%
3	Crossref 234 words Bappa Acherjee, Dipan Mitra, Dipankar Saha, K. Venkatesh shekhar. "Prediction of weld strength and seam width to ..."	<1%
4	Internet 202 words created on 24-Mar-2021 epdf.pub	<1%
5	Internet 136 words created on 25-Mar-2022 cook.info	<1%
6	Internet 116 words created on 11-Apr-2020 www.mppi.com	<1%
7	Internet 111 words created on 24-Dec-2019 dipca.ib.cranfield.ac.uk	<1%
8	Internet 100 words created on 14-Mar-2022 www.pduniv.edu.in	<1%
9	Internet 94 words created on 14-Sep-2022 www.researchgate.net	<1%
10	Crossref 91 words "Advances in Manufacturing Engineering" Springer Science and Business Media LLC, 2023	<1%
11	Internet 88 words created on 30-Sep-2022 link.springer.com	<1%
12	ProQuest 81 words Bappa Acherjee, Leonardo. "Application of Game Modeling to profit learning practice", Proquest, 2011/03	<1%

PAGE 1 OF 108

Smt.
18/10/22

AB Duggirala
18/10/22

DR. BAPPA ACHERJEE
ASSISTANT PROFESSOR
DEPARTMENT OF PRODUCTION & INDUSTRIAL ENGINEERING
BIRLA INSTITUTE OF TECHNOLOGY
MESRA, RANCHI - 835215, INDIA